

---


Electronic Theses and Dissertations, 2020-

---

2021

## Atomically Thin Platinum-based Dichalcogenide Materials for Multifunctional Photo-sensitive Applications

Mashiyat Sumaiya Shawkat  
University of Central Florida

 Part of the [Electrical and Computer Engineering Commons](#)  
Find similar works at: <https://stars.library.ucf.edu/etd2020>  
University of Central Florida Libraries <http://library.ucf.edu>

This Doctoral Dissertation (Open Access) is brought to you for free and open access by STARS. It has been accepted for inclusion in Electronic Theses and Dissertations, 2020- by an authorized administrator of STARS. For more information, please contact [STARS@ucf.edu](mailto:STARS@ucf.edu).

---

### STARS Citation

Shawkat, Mashiyat Sumaiya, "Atomically Thin Platinum-based Dichalcogenide Materials for Multifunctional Photo-sensitive Applications" (2021). *Electronic Theses and Dissertations, 2020-*. 1345.  
<https://stars.library.ucf.edu/etd2020/1345>

ATOMICALLY THIN PLATINUM-BASED DICHALCOGENIDE MATERIALS FOR  
MULTIFUNCTIONAL PHOTO-SENSITIVE APPLICATIONS

by

MASHIYAT SUMAIYA SHAWKAT  
B.S. BRAC University, 2014

A dissertation submitted in partial fulfilment of the requirements  
for the degree of Doctor of Philosophy  
in the Department of Electrical and Computer Engineering  
in the College of Engineering and Computer Science  
at the University of Central Florida  
Orlando, Florida

Fall Term  
2021

Major Professor: Yeonwoong Jung

© 2021 Mashiyat Sumaiya Shawkat

## ABSTRACT

Two-dimensional (2D) transition metal dichalcogenides (TMDs) are a distinct class of atomically thin materials assembled by weak van der Waals bonding. They exhibit 2D layer number-dependent bandgap tunability promising exciting applications in electronics and optoelectronics. Among them, there is a surge of interest in Platinum-based dichalcogenides (e.g., PtSe<sub>2</sub> and PtTe<sub>2</sub>). 2D PtSe<sub>2</sub> has a theoretically predicted carrier mobility of  $>1000 \text{ cm}^2/(\text{Vs})$ , at room temperature, which is higher than that of most 2D TMDs. Additionally, 2D PtSe<sub>2</sub> exhibits a semiconducting to metallic transition with an increasing number of layers. 2D PtTe<sub>2</sub> is highly metallic in its few-layer form and exhibits electrical conductivity of  $> 10^6 \text{ S/m}$  – superior to most of the previously reported 2D TMDs. These properties project the promise of Platinum-based dichalcogenides for photosensitive applications. This intrinsic superiority of Platinum-based dichalcogenides is improved further when they are merged with conventional three-dimensional (3D) semiconductors such as silicon (Si). We applied a novel chemical vapor deposition (CVD) technique to synthesize large-area 2D PtSe<sub>2</sub> and 2D PtTe<sub>2</sub> directly on various substrates with controlled 2D layer orientation and electronic property. With direct CVD synthesis of metallic 2D PtSe<sub>2</sub> and PtTe<sub>2</sub> on silicon (Si) wafer, we created 2D PtSe<sub>2</sub>/Si and 2D PtTe<sub>2</sub>/Si Schottky junction devices. We investigated their photovoltaic performance as well as viability as photodetectors in visible to mid-infrared (MIR) regimes. The PtTe<sub>2</sub>/Si photodetectors exhibit fast photoresponse time ( $\sim 1 \mu\text{s}$ ) and high photodetectivity ( $>10^{13}$  Jones) in visible light and display photocurrent up to  $7 \mu\text{m}$  wavelength regime. Finally, we extended the application of Platinum-based dichalcogenides into flexible optoelectronics by directly synthesizing Platinum-based dichalcogenides on thin Si wafer or polyimide substrates, owing to their low synthesis temperature. These studies are a part of a new paradigm shift of using Pt-based TMDs with unique optical, electrical, and mechanical properties in unique photosensitive devices.

This dissertation is dedicated to my parents, my husband, my sister, and my grandparents

## ACKNOWLEDGMENTS

This dissertation is a result of the continuous support of several key individuals in my life.

I would like to express my gratitude to my professor, Dr. Yeonwoong Jung, for his constant mentorship throughout my program. Dr. Jung displayed confidence in my scientific abilities to pursue my research interests in his lab. He provided regular feedback and guidance, which helped me sharpen my technical and communication skills required to be a capable researcher in my field.

I thank Dr. Tania Roy, Dr. Kalpathy Sundaram, Dr. Jiann-Shiun Yuan, and Dr. Lei Zhai for serving on my committee and giving me important pieces of advice throughout my Ph.D. journey despite their busy schedules.

I am immensely thankful to my husband, Tanvir, for his unwavering support and encouragement. He has been my ultimate source of strength and positivity that powered me throughout this journey. I am incredibly grateful to you, my love.

I am indebted to my parents for the love and support they provided me. They have always been a source of inspiration and unconditional love for me. I am grateful for all the sacrifices they made for me. I am also thankful to my younger sister for being a ball of joy in my life. I am grateful to have grandparents who always showered me with love and encouragement, and I know they would be incredibly proud today if they were still alive. I am also very grateful to my friends for being there with me through the good times and the bad.

I am thankful for my past and present lab partners – Dr. Mengjing Wang, Dr. Tae-Jun Ko, Dr. Sang Sub Han, Dr. Emmanuel Okogbue, Dr. Ashraful Islam, Dr. Nitin Choudhary, Dr. Jung Han Kim, Dr. Changhyeon Yoo, Markoni, Dwight, Dr. Sohrab, Dr. Hao Li, Luis, and Sushant for all the insightful discussions and engaging ideas that lead to many successful collaborations. I

express sincere gratitude to our collaborators, Dr. Tania Roy, Dr. Hee-Suk Chung, Dr. Dong-Kyun Ko, Dr. Debashis Chanda, Dr. YounJoon Jung, Dr. Gwan-Hyoung Lee, Dr. J Andreas Larsson, and Dr. Shahid Sattar, for their support on multiple projects with various material and device characterizations.

## TABLE OF CONTENTS

LIST OF FIGURES . . . . .	viii
CHAPTER 1: INTRODUCTION . . . . .	1
2D Materials . . . . .	1
Graphene . . . . .	1
Transition Metal Dichalcogenides (TMDs) . . . . .	2
Refractory Metal-Based Dichalcogenides . . . . .	3
Platinum (Pt)-Based Dichalcogenides . . . . .	4
Motivation . . . . .	6
Why Pt-Based Dichalcogenides for Photosensitive Applications? . . . . .	6
Issues and Challenges . . . . .	7
Objectives . . . . .	9
Dissertation Overview . . . . .	9
CHAPTER 2: LARGE-AREA DIRECT SYNTHESIS OF PLATINUM-BASED DICHALCO- GENIDES . . . . .	12
Introduction . . . . .	12

Experimental Method . . . . .	13
Thickness Dependent 2D Layer Orientation Transition . . . . .	14
Thickness Dependent Electrical Transport . . . . .	17
 CHAPTER 3: CONSTRUCTION OF 2D/3D SCHOTTKY JUNCTIONS . . . . .	 22
Introduction . . . . .	22
Process of Fabrication of 2D/3D Schottky Junctions . . . . .	23
Direct Synthesis of PtSe <sub>2</sub> on Silicon Substrate . . . . .	24
Structural and Chemical Characterization . . . . .	24
Direct Synthesis of PtTe <sub>2</sub> on Silicon Substrate . . . . .	27
Structural and Chemical Characterization . . . . .	27
Conclusion . . . . .	29
 CHAPTER 4: SEMICONDUCTING-TO-METALLIC CONVERSION IN WAFER-SCALE 2D PTSE <sub>2</sub> LAYERS BY PLASMA-DRIVEN CHALCOGEN DEFECT ENGI- NEERING . . . . .	   30
Introduction . . . . .	30
Results and Discussion . . . . .	32
Process of Plasma Treatment . . . . .	32

Structural and Chemical Characterization of As-Grown 2D PtSe <sub>2</sub> . . . . .	33
Electrical Characterization After Plasma Treatment . . . . .	35
Temperature-Variant Electrical Characterization After Plasma Treatment . . . . .	38
Chemical and Structural Characterization Before and After Plasma Treatment . . .	40
Conclusion . . . . .	44
CHAPTER 5: 2D PTSE <sub>2</sub> /3D SILICON SCHOTTKY JUNCTION FOR SOLAR CELL AP- PLICATION . . . . .	45
Introduction . . . . .	45
Results and Discussion . . . . .	46
Temperature-Variant Electrical Characterization . . . . .	46
Photovoltaic Characterization . . . . .	49
Opto-Mechanical Properties . . . . .	51
Conclusion . . . . .	52
CHAPTER 6: 2D PTTE <sub>2</sub> /3D SILICON SCHOTTKY JUNCTION FOR VISIBLE LIGHT PHOTODETECTION . . . . .	54
Introduction . . . . .	54
Results and Discussion . . . . .	55

Photovoltaic Performance . . . . .	55
Photodetection Performance . . . . .	57
Characterization of Photoresponse Speed . . . . .	59
Band Diagram . . . . .	61
Super-Hydrophobicity Driven Photovoltaic Improvement . . . . .	62
Conclusion . . . . .	65
CHAPTER 7: 2D PTTE <sub>2</sub> /3D SILICON SCHOTTKY JUNCTION FOR NEAR-TO-MID INFRARED PHOTODETECTION . . . . .	66
Introduction . . . . .	66
Results and Discussion . . . . .	68
Near Infrared Photodetection Performance . . . . .	68
Mid Infrared Photodetection Performance . . . . .	71
Fourier Transform IR (FTIR) . . . . .	73
Opto-Mechanical Characterization . . . . .	75
Conclusion . . . . .	77
CHAPTER 8: WATER-ASSISTED TRANSFER AND VAN DER WAALS ASSEMBLY OF NEAR-ATOM THICKNESS HETERO-MEMBRANES . . . . .	78

Introduction . . . . .	78
Results and Discussion . . . . .	80
Water-Assisted Transfer and Van Der Waals Assembly Method . . . . .	80
Mechanism for Water-Assisted Method . . . . .	80
PtTe <sub>2</sub> /PtS Hetero-Membranes for Near Infrared Photodetection . . . . .	84
Opto-Mechanical Performance . . . . .	86
Conclusion . . . . .	88
CHAPTER 9: SUMMARY AND FUTURE PERSPECTIVES . . . . .	90
Summary . . . . .	90
Future Perspectives . . . . .	91
APPENDIX : COPYRIGHT PERMISSIONS . . . . .	93
LIST OF REFERENCES . . . . .	107

## LIST OF FIGURES

Figure 1.1: Periodic table highlights transition metals and chalcogen elements that form transition metal dichalcogenides (TMDs) in a layered crystalline structure. Partial highlights for Co, Rh, Ir and Ni signifies that not all their dichalcogenides form layered structures. Adapted with permission from reference. [1] . . . . .	2
Figure 1.2: Band structure transition of MoS <sub>2</sub> from bulk to monolayer. Bandstructure of (a) bulk MoS <sub>2</sub> , (b) 4-layer MoS <sub>2</sub> , (c) 2-layer MoS <sub>2</sub> , and (d) monolayer MoS <sub>2</sub> . Bulk MoS <sub>2</sub> exhibits an indirect bandgap. With thickness reduction, the bandgap increases and transits to a direct bandgap in monolayer MoS <sub>2</sub> . Adapted with permission from reference. [2] . . . . .	4
Figure 1.3: (a) Atomic structure of PtSe <sub>2</sub> and (b) its three-dimensional (3D) side views. Adopted with permission from reference.[3] . . . . .	6
Figure 1.4: Room temperature mobility of typical 2D materials, noble metal-based dichalcogenides, BP, and refractory metal-based dichalcogenides. Adapted with permission from reference.[4] . . . . .	7
Figure 2.1: (a) Schematic illustration of quartz tube CVD furnace used for thermally assisted conversion of transition metal into transition metal dichalcogenide. (b) Image of a large-area PtTe <sub>2</sub> synthesized on SiO <sub>2</sub> /Si substrate. Adapted with permission from reference.[5] . . . . .	14

Figure 2.2: (a) Schematics for growth characteristics of 2D PtTe<sub>2</sub> layers obtained by tel-  
lurizing (a) scattered Pt nanoclusters, (b) dense Pt nanoclusters, and (c) con-  
tinuous Pt films. (d-f) HAADF-STEM images of (d) holey layers with the  
pores indicated by the red arrow, (e) continuous layers, and (f) continuous  
layers with pronounced imaging contrast. (g-i): High-resolution HAADF-  
STEM images of (g) (110) lattice fringes in crystalline grains with a grain  
boundary, (h) (110) lattice fringes from crystalline 2D basal planes of three  
distinct orientations, and (i) (001) lattice fringes denoting 2D layer vertical  
orientation. (j-l): Cross-sectional STEM images of (j) edge-terminated hori-  
zontally aligned 2D layers, (k) reorientation of 2D layers along with the top  
and bottom insets corresponding to the blue and red boxed regions, and (l)  
vertically aligned 2D layers along with the inset corresponding to the green  
boxed region. The scale bars of the insets are 1 nm. Adapted with permission  
from Reference [5] . . . . . 15

Figure 2.3: Electrical characterizations of vertically aligned 2D PtSe<sub>2</sub> layers. (a) Schematic  
of a back-gated FET device based on vertically aligned 2D PtSe<sub>2</sub> layers.  
(b, c) Characterization of a horizontally-aligned 2D PtSe<sub>2</sub> layers-based FET  
demonstrating (b)  $I_{ds}$ - $V_{ds}$  and (c)  $I_{ds}$ - $V_g$  transfer characteristics. (d, e) Char-  
acterization of a vertically-aligned 2D PtSe<sub>2</sub> layers-based FET demonstrating  
(d)  $I_{ds}$ - $V_{ds}$  and (e)  $I_{ds}$ - $V_g$  transfer characteristics. Adapted with permission  
from Reference [6] . . . . . 18

Figure 2.4: Electrical characterizations of vertically aligned 2D PtTe<sub>2</sub> layers. (a) Thickness of 2D PtTe<sub>2</sub> layers as a function of Pt thickness. (b, c) Back-gate FET measurements of 2D PtTe<sub>2</sub> layers obtained from  $\sim 0.5$  nm Pt thickness, showing (b)  $I_{ds}-V_{ds}$  and (c)  $I_{ds}-V_g$  transfer characteristics. (d) I–V curves of 2D PtTe<sub>2</sub> prepared from various Pt thicknesses. (e) Conductance as a function of Pt thickness. (f) Conductivity as a function of Pt thickness showing a presence of its thickness-dependent maximum point. The junction of the blue and red shading represents a transition of horizontal-to-vertical layer orientation. (g) Schematics of electron transports in horizontally vs. vertically aligned 2D PtTe<sub>2</sub> layers. Adapted with permission from [5] . . . . . 19

Figure 3.1: Fabrication of 2D TMD/Si Schottky devices. (a) Illustration of step-by-step procedures to fabricate a 2D PtSe<sub>2</sub>/Si or 2D PtTe<sub>2</sub>/Si Schottky device (b) Schematic diagram describing thermally assisted conversion assisted method used to synthesize 2D PtSe<sub>2</sub> or or 2D PtTe<sub>2</sub>. (c) Schematic (left) and digital camera image (right) of the final device (c) Representative image of a completed 2D PtSe<sub>2</sub>/Si Schottky device. Adapted with permission from Reference [7], [5] . . . . . 23

Figure 3.2: Structural and chemical characterizations of vertically aligned 2D PtSe<sub>2</sub> layers. (a–e) Structural and chemical characterizations: (a, b) TEM characterization of vertically aligned 2D PtSe<sub>2</sub> layers in (a) low-magnification and (b) high-magnification views. (c) Raman spectroscopy characterization. (d) Cross-sectional STEM image of vertically aligned 2D PtSe<sub>2</sub> layers. (e) STEM-EDS elemental mapping images corresponding to (d). Adapted with permission from Reference [6]. . . . . 25

Figure 3.3: Material characterization of 2D PtTe<sub>2</sub> synthesized on Silicon. (a) Raman spectroscopy characterization of few-layered 2D PtTe<sub>2</sub>, comparing the theoretically calculated spectrum (black solid line) with the experimentally determined one (blue dotted line). (b) XPS spectra of Pt 4f (left) and Te 3d (right) core levels obtained from 2D PtTe<sub>2</sub> layers grown on a Si wafer. (c) Plane-view STEM image of 2D PtTe<sub>2</sub> layers and the corresponding SAED pattern in the inset. (d) Plane-view HR-STEM image revealing two neighboring stitching grains, separated by the grain boundary (purple dotted curve). (e) Cross-sectional HR-STEM image of 2D PtTe<sub>2</sub> multilayers. (f) Cross-sectional STEM–EDS elemental mapping images corresponding to (e). Adapted with permission from Reference [7], [8]. . . . . 27

Figure 4.1: Schematic illustration for the preparation of Ar-plasma-treated and -untreated areas within identical 2D PtSe<sub>2</sub> layers. Adapted with permission from reference [9]. . . . . 33

Figure 4.2: Structural and chemical characterization of as-grown 2D PtSe<sub>2</sub> layers. (a) Image of large-area 2D PtSe<sub>2</sub> layers grown on a SiO<sub>2</sub>/Si substrate. (b) Raman spectroscopy profile from the corresponding sample. (c) Low-magnification plane-view TEM image. (d) Corresponding HR-STEM image revealing Moiré fringe patterns (blue box) and their corresponding atomic structure simulation (right). The inset shows the FFT image corresponding to the blue box, depicting a misalignment angle of 13°. (e) Cross-sectional HR-TEM image (left) revealing horizontally aligned 2D PtSe<sub>2</sub> multilayers and their corresponding atomic structure model (right). (f) STEM-EDS elemental mapping images corresponding to (e), confirming the homogeneous spatial distribution of Pt and Se. Adapted with permission from reference [9] . . . . . 34

Figure 4.3: Electrical and Raman characterization of 2D PtSe<sub>2</sub> layers in their pristine and Ar-plasma-treated states. (a) Schematic of a 2D PtSe<sub>2</sub> layer-based FET device with Au electrodes in a back-gate configuration. (b) Optical microscopy image of a representative FET device. (c) Optical microscopy image unveiling color contrast between plasma-treated and -untreated regions within identical 2D PtSe<sub>2</sub> layers. (d)  $I_{ds}-V_{ds}$  FET transfer plots from pristine 2D PtSe<sub>2</sub> layers, confirming p-type semiconducting characteristics. The inset shows the corresponding  $I_{ds}-V_g$  transfer characteristics. (e)  $I_{ds}-V_{ds}$  FET transfer plots from plasma-irradiated 2D PtSe<sub>2</sub> layers, confirming metallic characteristics with almost zero-gate modulation. The inset shows the corresponding  $I_{ds}-V_g$  transfer characteristics. (f)  $I_{ds}-V_{ds}$  characteristics from another FET device with thicker 2D PtSe<sub>2</sub> layers systematically irradiated with Ar-plasma for varying durations. The drain voltage was set at 1 V. (g) Raman spectroscopy profiles obtained from the sample corresponding to (f) with varying plasma irradiation times. Adapted with permission from reference [9] . . . . 36

Figure 4.4: Temperature-variant FET transport characteristics of 2D PtSe<sub>2</sub> layers in pristine vs Ar-plasma-irradiated states. Pristine 2D PtSe<sub>2</sub> layers revealing (a)  $V_g$ -dependent  $I_{ds}$ - $V_{ds}$  transfer curves at 300 K and (b)  $I_{ds}$ - $V_{ds}$  characteristics under  $V_g = 0$  V obtained at 300 and 412 K. Ar-treated 2D PtSe<sub>2</sub> layers revealing (c)  $V_g$ -dependent  $I_{ds}$ - $V_{ds}$  transfer curves at 300 K and (d)  $I_{ds}$ - $V_{ds}$  characteristics under  $V_g = 0$  V obtained at 300 and 412 K. (e) Comparison of the current ratio with respect to 300 K as a function of temperature for the corresponding pristine and Ar-treated samples. (f) Comparison of activation energies for thermally driven transports of charge carriers in pristine vs Ar-plasma-treated 2D PtSe<sub>2</sub> layers. Adapted with permission from reference [9]. . . . . 38

Figure 4.5: Structural and chemical characterization of 2D PtSe<sub>2</sub> layers before/after the Ar-plasma treatment. XPS spectra of (a) Pt 4f and (b) Se 3d core levels obtained from 2D PtSe<sub>2</sub> layers in pristine vs Ar-plasma-treated states. Low-magnification TEM images (left) and corresponding SAED patterns (right) from 2D PtSe<sub>2</sub> layers in (c) untreated and (d) treated states. (e) EDS spectra obtained from 2D PtSe<sub>2</sub> layers in Ar-plasma-treated and -untreated states. (f) HR-STEM image of Ar-plasma-irradiated 2D PtSe<sub>2</sub> layers. Zoom-in images corresponding to the (g) red and (h) blue boxes in (f). (i) Cross-sectional HRTEM image of Ar-plasma-irradiated 2D PtSe<sub>2</sub> layers. (j) EDS elemental map images visualizing a localized distribution of Pt and deficiency of Se. Adapted with permission from reference [9]. . . . . 42

Figure 5.1: Characterization of Schottky junction characteristics in 2D PtSe<sub>2</sub>/Si devices.

(a) I–V characteristics of a 2D PtSe<sub>2</sub>/Si Schottky junction device. The inset presents the corresponding semilog plot. (b) I–V characteristics from only-2D PtSe<sub>2</sub> layers and only-Si wafers without 2D PtSe<sub>2</sub>/Si junctions obtained with Au contacts. (c) I–V characteristics with varying temperature in a range of 320–380 K. (d) Semilog plots corresponding to (c). (e) Temperature-dependent Schottky barrier height and ideality factor. Adapted with permission from reference [6]. . . . . 46

Figure 5.2: Photovoltaic characteristics of 2D PtSe<sub>2</sub>/Si devices. (a, b) J–V characteristics of a 2D PtSe<sub>2</sub>/Si Schottky junction device in dark (red) and under illumination (blue) in (a) linear and (b) semilog scales. (c) Representative band diagram of a 2D PtSe<sub>2</sub>/Si Schottky junction under zero bias. (d) Photo image of a flexible 2D PtSe<sub>2</sub>/Si Schottky junction device. (e) I–V characteristics of the device in (d) in dark (red) and under illumination (blue). The inset presents the corresponding characteristics on a semilog scale. Adapted with permission from reference [6]. . . . . 49

Figure 5.3: Flexible photovoltaic 2D PtSe<sub>2</sub>/Si devices. (a–c) Photovoltaic responses before/after repeated bending at a bending radius of R1 = 9.43 mm. (a) Corresponding image. (b) Photovoltaic characteristics before bending. (c) Photovoltaic characteristics after 100 times bending at R1. (d–f) Photovoltaic responses before/after repeated bending at a bending radius of R2 = 5.95 mm. (d) Corresponding image. (e) Photovoltaic characteristics before bending. (f) Photovoltaic characteristics after 100 times bending at R2. (g) J<sub>sc</sub> with varying bending cycles. (h) V<sub>oc</sub> with varying bending cycles. Adapted with permission from reference [6]. . . . . 52

Figure 6.1: (a-b) Photovoltaics of PtTe <sub>2</sub> /p-Si devices prepared with Pt of 4.5 nm thickness; (a) J–V characteristics in the dark (red) and under illumination (blue), and (b) the corresponding presentation in the semi-log scale. Adapted with permission from Reference [7]. . . . .	56
Figure 6.2: (a) I–V characteristics of a 2D PtTe <sub>2</sub> /3D Si device in the semi-log scale measured under 625 nm illumination of varying intensities. (b, c) Photo-responsiveness measured at zero external bias; (b) Temporal response of a device under 625 nm illumination of varying intensities. (c) Light intensity-dependent specific detectivity (red) and responsivity (blue) of the same device in (d). Adapted with permission from Reference [7]. . . . .	57
Figure 6.3: Schematic illustration of the experimental setup for recording the temporal photo-responsiveness of PtTe <sub>2</sub> /p-Si devices under periodically pulsed 625 nm illumination. (b–d) Temporal photo-responsiveness of a device measured at varying illumination frequencies of (b) 10 Hz, (c) 30 kHz, and (d) 300 kHz. (e) Relative balance, $(I_{max} - I_{min})/I_{max}$ , of the same device as a function of illumination modulation frequency revealing a 3-dB cutoff frequency of >300 kHz. (f) Magnified view of photo-switching characteristics obtained at 150 kHz clarifying rise ( $\tau_r$ ) and fall ( $\tau_f$ ) times. Adapted with permission from Reference [7]. . . . .	59

Figure 6.4: (a) PAEP diagram of few layered 2D  $\text{PtTe}_2$  and its calculated work function, (4.56 eV, green line) with the vacuum level at 0 eV. (b) Determination of the work function of p-Si (4.95 eV, orange line) and band offsets by superimposing the PAEP of bulk Si on that of the slab and calibrating the vacuum level to 0 eV. (c) Energy band diagrams for 2D  $\text{PtTe}_2$  and p-Si that form a p-type Schottky contact upon interfacing. (d) Band bending diagram revealing the presence of  $\text{PtTe}_2$ /p-Si Schottky barrier whose height is determined to be 0.67 eV (violet line). Adapted with permission from Reference [7]. . . . . 61

Figure 6.5: (a) Image of water droplets integrated on a  $\text{PtTe}_2$  /p-Si device. (b) I–V characteristics of the  $\text{PtTe}_2$  /p-Si device in the dark (blue), under illumination (red), and after integrating the water droplet shown in the inset (black). (c) I–V characteristics in the semi-log scale corresponding to (b). (d) Change of photovoltaic parameters induced by the water droplet integration in (b) and (c). (e) Integration of water droplets on the  $\text{PtTe}_2$  /p-Si device slanted at  $\sim 45^\circ$  under continuous illumination from a 625 nm LED source at an intensity of 29.8 mW/cm<sup>2</sup>. (f) Temporal current obtained from the device in (e) with a periodic integration of water droplets at an interval of  $\sim 1.6$  s. (g) Enlarged view of the blue dotted region in (f) highlighting the current change by the droplet integration and rolling-off due to gravity. (h) Schematic illustration of the increased concentration of photo-generated carriers by the light concentration effect. Adapted with permission from Reference [7]. . . . . 63

Figure 7.1: (a) Plot of optical transmittance (red) vs electrical conductivity (blue) for 2D PtTe<sub>2</sub> layers prepared with varying Pt thickness values. (b) I–V curve in dark and its corresponding semilog plot (inset) denoting an ideality factor of  $\sim 1.08$ . (c) Temporal photo-response of the same device in (b) under 1.5  $\mu\text{m}$  illumination. (d) Illumination wavelength-dependent responsivity. Adapted with permission from reference [7]. . . . . 69

Figure 7.2: (a) Plot of MIR photocurrent measured using 900 °C-calibrated blackbody radiation filtered with Ge as an illumination source. (b) Spectral irradiance of the blackbody obtained from a band-pass filter in a center wavelength range of 2–7  $\mu\text{m}$ , estimated using the Planck radiation formula. The inset displays the calculated optical power obtained by integrating the area under the respective blue curves at each wavelength. (c) Photocurrents measured with illumination of varying wavelengths. (d) Illumination wavelength-dependent specific detectivity. All measurements were conducted at room temperature 300 K using a constant bias of - 0.6 V. Adapted with permission from reference [7]. . . . . 73

Figure 7.3: (a) FTIR absorbance spectra of a bare Si wafer (red) and 2D PtTe<sub>2</sub> layers integrated on a glass (blue). (b) FTIR absorbance spectrum of a 2D PtTe<sub>2</sub>/Si device and the corresponding characteristics up to 14  $\mu\text{m}$  in wavelength (inset). (c) Schematic illustration of a stand-alone 2D PtTe<sub>2</sub> layer-based device. (d) Temporal photo-response of devices with and without the 2D PtTe<sub>2</sub>/Si junction. The device with the junction was characterized with an illumination frequency of 1000 Hz (blue arrow). Adapted with permission from reference [7]. . . . . 74

Figure 7.4: (a) Images of a thin Si wafer under bending (top) and a 2D PtTe<sub>2</sub>/Si flexible photodetector (bottom). The inset shows the top view of the device prior to its attachment to the supporting substrate. (b) Intensity-dependent temporal photo-response obtained from the flexible 2D PtTe<sub>2</sub>/Si device at an illumination wavelength of 0.94  $\mu$ m. (c) Plot of photocurrent vs illumination intensity. (d) Plot of photocurrent vs bending cycles for a flexible device subjected to a reduction of lateral length by 20%. (e) Plot of responsivity vs bending cycles. (f) Plot of intensity-dependent temporal photo-response obtained after a completion of 1000 bending cycles. Adapted with permission from reference [7]. . . . . 76

Figure 8.1: a) Schematic illustration describing water-assisted, polymer-free green integration of CVD-grown nano-membranes on arbitrary substrates. Adapted with permission from reference [10]. . . . . 81

Figure 8.2: Mechanism of water-assisted transfer. Schematic illustration of the water-assisted integration of 2D PtTe<sub>2</sub> layers and 3D PtS membranes on arbitrary substrates. (a) Time-lapsed images displaying the water-assisted delamination of 3D PtS membranes. The red dotted circle denotes the delaminated membrane floating on the water surface. (b) Water droplet images and WCA measurements of a similar sample at its pristine (left) and aged (right) state. (c) Plot of time-dependent WCA values. (d) Comparison of the delamination efficacy for the samples with two distinct water wettability. (e) Representative image of 2D MoS<sub>2</sub> on an assortment of unconventional substrates, e.g. wood and paper. (f) Demonstration of the vdW assembly of multiple layers of 2D MoS<sub>2</sub> onto a PET substrate. L0, L1, L2 represent first, second and third time integration of MoS<sub>2</sub> layers. Integration of 2D WSe<sub>2</sub> layers (g) and 2D PtSe<sub>2</sub> layers (h) onto PET substrates. Adapted with permission from reference [10, 11]. . . . . 82

Figure 8.3: a) Schematic illustration of combining the patterned growth of 2D PtTe<sub>2</sub> layers with the water-assisted integration of 3D PtS membranes on arbitrary substrates. (b) Camera image of a PtTe<sub>2</sub>/PtS hetero-material integrated on a PI substrate. The scale bar is 1 cm. (c) Graph of intensity-dependent temporal photo-responsiveness obtained from the sample in (b) at 625 nm wavelength at a bias of 1 V. (d–f) Graphs representing intensity-dependent temporal photo-responsiveness obtained at 940 nm wavelength from various hetero-junctions; (d) PtTe<sub>2</sub>-PtS-PtTe<sub>2</sub>, (e) Au-PtS-Au, (f) PtTe<sub>2</sub>-PtS, respectively. The scale bars in the inset images are 0.5 cm. (g) Plot of responsivity versus intensity obtained from a PtTe<sub>2</sub>/PtS/PtTe<sub>2</sub> sample. Adapted with permission from reference [11]. . . . . 84

Figure 8.4: (a) Camera images of a  $\text{PtTe}_2/\text{PtS}/\text{PtTe}_2$  sample undergoing a string of bending degrees with varying bending radius ( $R_a$ ). (b–d) Graphs of intensity-dependent current versus time obtained from the sample in (a) at various bending radii; (b) 11.8, (c) 9.9, and (d) 8.9 mm at a bias of 1 V. (e) Plot of photocurrent versus radius of bending, with varying illumination intensity obtained at 625 nm wavelength, at a bias of 1 V. Adapted with permission from reference [11]. . . . . 87

Figure 8.5: (a) Plots of intensity-dependent temporal photo-responsiveness under various bending radii at 940 nm illumination. (b) Plots of intensity-dependent temporal photo-responsiveness obtained from an identical sample subjected to reversible bending/unbending for 10, 100, and 400 cycles. (c) Comparison of maximum photocurrent versus intensity for three different bending cycles. Adapted with permission from reference [11]. . . . . 88

# CHAPTER 1: INTRODUCTION

## 2D Materials

Since the isolation of graphene, a monolayer of graphite, in 2004[4], two-dimensional (2D) materials have received a surge of interest. They exhibit unique material properties due to their exceptionally small thickness, and van der Waals (vdW) assembled 2D layers. These unique properties propelled the search for 2D materials with electronic properties ranging from insulating to semi-conducting and metallic,[12, 13] e.g., hexagonal boron nitride (h-BN), black phosphorus (BP), and transitional metal dichalcogenides (TMDs).

### *Graphene*

Graphene is a 2D sheet having  $sp^2$ -hybridized carbon. It has carbon atoms arranged in a honeycomb structure. This honeycomb structure is present in all the essential allotropes of carbon. Stacking 2D layers form three-dimensional (3D) graphite, whereas rolling a layer forms 1D nanotubes. Graphene presents superior thermal and electrical performance.

Additionally, it has high transparency and can sustain a large degree of mechanical strain, making it highly promising for high-performance flexible applications.[14, 15] Graphene has a zero bandgap, and due to this, it suffers from high dark current and low current on/off ratio. Therefore, additional functionalization is required, which makes graphene challenging to be utilized in practical electronic applications. Hence, interest shifted towards other materials which have non-zero bandgaps, such as TMDs and BP.

### Transition Metal Dichalcogenides (TMDs)

Among the large group of 2D materials, 2D TMDs received significant attention due to their non-zero bandgap and therefore allowing high current on/off ratio, suitable for electronics. Weak dielectric screening and strong dimensional confinement lead to significantly strong Coulomb interaction and allow unusual excitonic effects that enable strong light-matter interactions and ultrafast optoelectronic response.[16] Quantum confinement effect leads to bandgap tunability with a dimensional reduction in 2D TMDs. TMDs also provide a degree of freedom to engineer their electronic band structure by compositional tuning, defect engineering, etc.[17] These properties make 2D TMDs an exciting material system for optoelectronics.[18, 19] They are a group of compounds in the form of  $MX_2$ , (M: transition metals, X: chalcogens) assembled by weak van der Waals (vdW) bonding. There exists an extensive library of 2D TMDs, as shown in Figure 1.1.

H	MX <sub>2</sub> M = Transition metal X = Chalcogen																He
Li	Be											B	C	N	O	F	Ne
Na	Mg	3	4	5	6	7	8	9	10	11	12	Al	Si	P	S	Cl	Ar
K	Ca	Sc	Ti	V	Cr	Mn	Fe	Co	Ni	Cu	Zn	Ga	Ge	As	Se	Br	Kr
Rb	Sr	Y	Zr	Nb	Mo	Tc	Ru	Rh	Pd	Ag	Cd	In	Sn	Sb	Te	I	Xe
Cs	Ba	La - Lu	Hf	Ta	W	Re	Os	Ir	Pt	Au	Hg	Tl	Pb	Bi	Po	At	Rn
Fr	Ra	Ac - Lr	Rf	Db	Sg	Bh	Hs	Mt	Ds	Rg	Cn	Uut	Fl	Uup	Lv	Uus	Uuo

Figure 1.1: Periodic table highlights transition metals and chalcogen elements that form transition metal dichalcogenides (TMDs) in a layered crystalline structure. Partial highlights for Co, Rh, Ir and Ni signifies that not all their dichalcogenides form layered structures. Adapted with permission from reference. [1]

Owing to the lack of dangling bonds on the surface of 2D TMDs, hetero-materials can be stacked on top of each other, forming atomically thin junctions such as p-n junctions.[20] Besides 2D

materials, they can also be integrated with 3D materials such as silicon to extend their functionality.[6, 7] Additionally, they present extraordinary mechanical flexibility compared to traditional thin-film inorganic semiconductors rendering vast opportunities towards devising futuristic devices of unconventional forms.[12,21]

### *Refractory Metal-Based Dichalcogenides*

Among the group of TMDs, refractory metal-based dichalcogenides ( $\text{MoS}_2$ ,  $\text{WS}_2$ ,  $\text{MoSe}_2$ , and  $\text{WSe}_2$ ) are the most commonly studied.[1, 16, 22–26] They present a diverse set of material and structural properties that make them suitable for photovoltaics, thermoelectrics, electrochemically-driven energy conversion/storage devices (e.g., batteries), displays, sensors, and actuators.[16,27] Some inherent limitations with their material properties and preparation methods hinder their widespread utilization for practical technologies. For instance, their carrier mobilities are inferior to those of traditional semiconductors (e.g., silicon or III-V compounds)[24, 28, 29], which further degrade when they are synthetically grown via scalable routes such as thermally assisted conversion (TAC)-based growth in a chemical vapor deposition (CVD) tube furnace.[30,31] Also, the synthesis temperatures are quite high ( $\sim 700\text{--}1000\text{ }^\circ\text{C}$ ) using TAC method in a CVD furnace. Generally, refractory metal-based dichalcogenides exhibit photo-sensitivity from visible to near-infrared regime owing to their large bandgap ( $\sim 1.1 - 2\text{ eV}$ ).

Additionally, they have an indirect to direct bandgap transition from multilayers to monolayer. Figure 1.2 shows the band structure of  $\text{MoS}_2$  in four different thicknesses. The excitonic transition remains unchanged even as the bandgap increases with reducing thickness. The indirect transition changes to a direct transition in monolayer  $\text{MoS}_2$ . [2, 27] Due to the larger bandgap, it has a high current on/off ratio but is limited in long-wavelength photodetection. Therefore interest shifted towards materials with non-zero but comparatively smaller bandgap such as BP and noble metal-

based dichalcogenides.

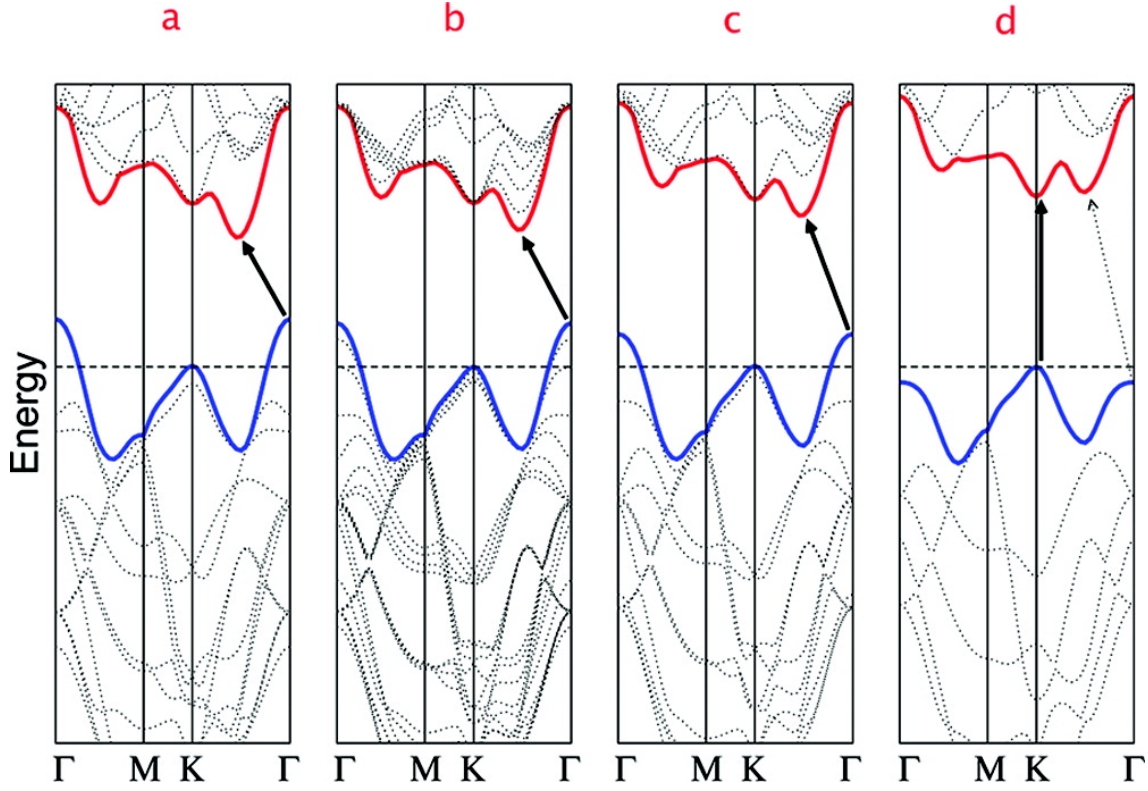


Figure 1.2: Band structure transition of MoS<sub>2</sub> from bulk to monolayer. Bandstructure of (a) bulk MoS<sub>2</sub>, (b) 4-layer MoS<sub>2</sub>, (c) 2-layer MoS<sub>2</sub>, and (d) monolayer MoS<sub>2</sub>. Bulk MoS<sub>2</sub> exhibits an indirect bandgap. With thickness reduction, the bandgap increases and transits to a direct bandgap in monolayer MoS<sub>2</sub>. Adapted with permission from reference. [2]

### *Platinum (Pt)-Based Dichalcogenides*

BP is a layered 2D material that has tunable direct bandgap between 0.3 to 2 eV and high carrier mobility over 1000 cm<sup>2</sup>/Vs.[4, 32] Owing to smaller bandgap, BP presents longer cutoff wavelength of photodetection compared to refractory metal-based dichalcogenides. Unfortunately, BP is prone to rapid air oxidation and its associated property degradation,[33,34] making it unsuitable for many practical applications. Recently, a new type of 2D TMDs based on noble metals such as

platinum (Pt) have been discovered, which include PtSe<sub>2</sub>, PtS<sub>2</sub> and PtTe<sub>2</sub>. [35–37]

Platinum diselenide (PtSe<sub>2</sub>) crystal has a 1T-type hexagonal crystal structure and 1T-PtSe<sub>2</sub> possesses a space group of p-3m1 as shown in Figure 1.3 a,b. Each layer consists of three layers of atoms stacked in the order of Se-Pt-Se. The layers are then held together by weak van der Waals forces. Platinum ditelluride (PtTe<sub>2</sub>) also presents a similar crystal structure. [5] It was reported that PtSe<sub>2</sub> presents a phase transition from 1T to 1H polymorph governed by diffusion of Se vacancies by annealing at 400 °C. It was observed that pentacene (C<sub>22</sub>H<sub>14</sub>) was selectively adsorbed in the 1H regions. Moreover, this transformation is reversible; the 1H phase can return to the pure 1T phase by absorbing Se atoms at  $\approx 270$  °C. [38]

Furthermore, PtSe<sub>2</sub> exhibits semiconducting to metallic transition or indirect to direct bandgap transition by applying external stimuli such as strain. For example, it was demonstrated that monolayer PtSe<sub>2</sub> transforms from an indirect bandgap semiconductor to a direct bandgap semiconductor upon applying a uniaxial compressive strain of  $\epsilon_y = 8\%$ . Additionally, a reversible semiconducting to metallic transition for bilayer PtSe<sub>2</sub> was observed under critical vertical strain ( $0.4 < \epsilon \leq 0.45$ ,  $1.2 \text{ GPa} < P \leq 3.6 \text{ GPa}$ ), which stemmed from the p-orbital coupling of the inner Se atoms. [39]

Pt-based dichalcogenides are d-electron-rich and have layer-dependent electrical properties, superior catalytic activity, and environmental stability. Through controlling the thickness of PtSe<sub>2</sub>, it has been observed that the edge site density for electrocatalytic activity can be effectively designed by tuning the number of layers. Interestingly, edge density could be tuned to be as high as 81%, and the maximum cathodic current density of up to  $227 \text{ mA cm}^{-2}$  was reached. [40] 2D PtSe<sub>2</sub> is gaining increasing attention due to distinguishable property advantages over refractory metal-based 2D TMDs. PtSe<sub>2</sub> has a theoretically predicted carrier mobility at room temperature of  $>1000 \text{ cm}^2/\text{Vs}$ , [41,42] making it promising for several applications such as field-effect transistors. On the other hand, 2D PtTe<sub>2</sub> exhibits extremely high electrical conductivity.

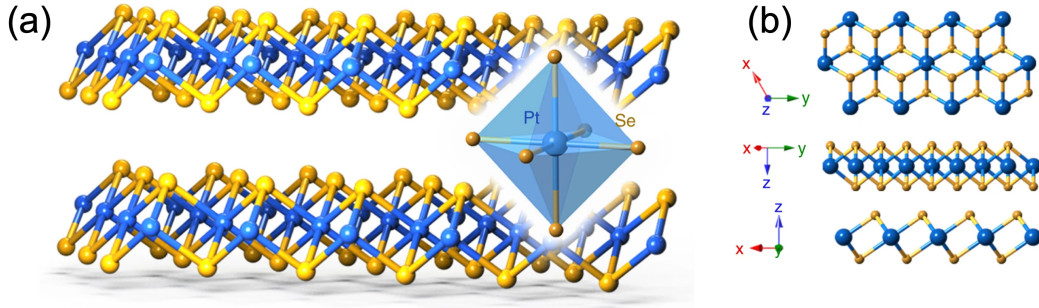


Figure 1.3: (a) Atomic structure of PtSe<sub>2</sub> and (b) its three-dimensional (3D) side views. Adopted with permission from reference.[3]

## Motivation

### *Why Pt-Based Dichalcogenides for Photosensitive Applications?*

PtSe<sub>2</sub> has a theoretically predicted mobility higher than  $>1000 \text{ cm}^2/\text{Vs}$ . [42] Figure 1.4 summarizes the room temperature carrier mobilities obtained from noble metal-based dichalcogenides, BP, and refractory metal-based dichalcogenides. [4] It can be observed that very high mobility of  $\approx 210 \text{ cm}^2/\text{Vs}$  was achieved with PtSe<sub>2</sub>, which greatly exceeds that of MoS<sub>2</sub> and is almost as high as BP. Unlike BP, 2D PtSe<sub>2</sub> is highly stable in ambient conditions. [41, 43] More interestingly, its carrier transport characteristics transition from metallic to semiconducting with a dimensional reduction from bulk to monolayer. [44] PtTe<sub>2</sub> presents extremely high electrical conductivity ( $> 10^6 \text{ S/m}$ ), superior to most of the previously reported 2D TMDs layers, both in  $\mu\text{m}$  scale synthesis methods and wafer-scale synthesis routes. [5, 45–47] Therefore, 2D PtTe<sub>2</sub> or 2D PtSe<sub>2</sub> can be good contenders for photosensitive applications where they also have to perform as top electrodes, such as in vertical architectures. [48] Given that PtSe<sub>2</sub> has a tunable bandgap from 1.3 eV to 0 eV and PtTe<sub>2</sub> has a tunable bandgap of 0.4 eV to 0 eV, they cover a wide range of the electromagnetic spectrum from

UV to mid-infrared regime ( $2\ \mu\text{m} - 8\ \mu\text{m}$ ) and even beyond.[49,50] Given that  $\text{PtSe}_2$  and  $\text{PtTe}_2$  are highly metallic, and their synthesis temperatures can be lower than refractory metal-based dichalcogenides, they can be directly synthesized on a silicon wafer to form heterojunctions and self-driven devices.[49] Given that 2D  $\text{PtSe}_2$  and 2D  $\text{PtTe}_2$  are highly electrically conductive, they can provide fast photoresponse even beyond what conventional TMDs can offer. It is also worth noting that for practical application, environmental stability is a critical factor.  $\text{PtSe}_2$  and  $\text{PtTe}_2$  exhibit ultra-high environmental stability showing promise in practical device applications.[51]

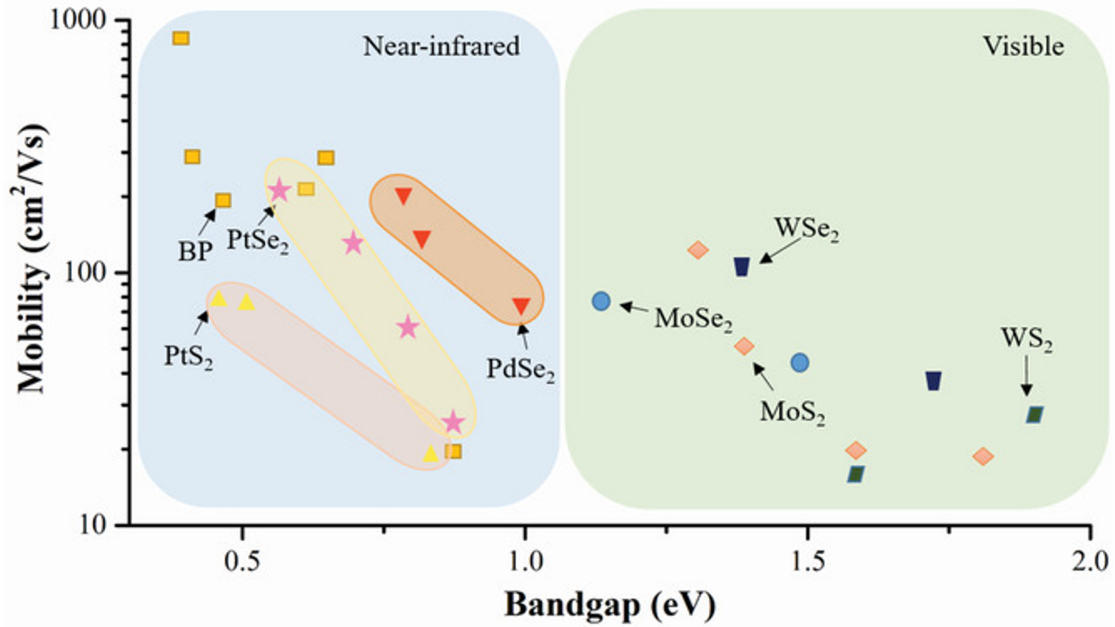


Figure 1.4: Room temperature mobility of typical 2D materials, noble metal-based dichalcogenides, BP, and refractory metal-based dichalcogenides. Adapted with permission from reference.[4]

### *Issues and Challenges*

Despite having significant potential, several challenges exist in realizing commercial electronics based on these Pt-based dichalcogenides. Scalable and controllable chemical synthesis of Pt-based

dichalcogenides with controlled layer orientation and electrical properties has not been established so far. A methodical study of their structure-property-thickness relationship is lacking, obstructing the full utilization of the fascinating properties presented by Pt-based dichalcogenides. Current methods for synthesizing Pt-based dichalcogenides include (1) chemical vapor transport growth of bulk crystals at high temperatures through self-reflux followed by mechanical exfoliation,[52] (2) co-evaporation of pre-cursor powders at a temperature range of  $\sim 800$ - $1100$  °C, [45, 46] and (3) eutectic liquid synthesis at  $\sim 700$  °C.[53] A significant drawback common in these approaches is that they result in 2D layers of limited size (i.e., typically  $\sim 5$ - $20$   $\mu\text{m}$ ) and non-uniform spatial distribution and surface coverage. Moreover, the adopted synthesis temperature is high and comparable to conventional 2D TMDs (e.g., 2D  $\text{MoS}_2$ ) despite the much lower melting temperature of Pt over refractory metals (e.g., Mo).[54]

Furthermore, 2D TMDs present some opportunities un-attainable with conventional materials. Previous studies reported that engineering their electronic band structures is possible by altering the concentration of chalcogen vacancies.[54, 55] This can result in unique electronic property after alteration. Attaining this controllably can make many futuristic applications possible, such as deterministic post-development tuning of electronic band structures in controlled regions to produce atomically thin electronic circuitry with the same 2D material system.

2D TMDs provide high in-plane mechanical strain ( $> 5$  times) compared to conventional inorganic thin films. To truly realize flexible, stretchable, and wearable devices, it is crucial to integrate these materials onto unconventional substrates with unusual form factors, e.g., bendable, stretchable, twistable, unconventional 3D shapes. The synthesis temperatures are often quite high  $\sim 800$  °C, synthesizing these materials directly on low-melting temperature substrates is challenging. Therefore, reliable transfer methods are required from growth substrate. Generally, transfer of 2D TMDs require a polymer protective layer, which needs to be rinsed off, leading to mechanical failure in the 2D layers. Additionally, toxic chemicals are also used to etch away underlying  $\text{SiO}_2$ . All these

processes lead to chemical change within the 2D layers. Given that 2D TMDs are held together by weak van der Waals forces, they can also be stacked on top of each other to attain attractive band offsets.

This thesis aims to make advancements in handling these issues and advance the commercialization of large-area high-quality Pt-based dichalcogenides.

### *Objectives*

The objectives of this thesis are as follows:

1. To develop scalable techniques to synthesize high-quality, large-area (i.e.,  $> \text{cm}^2$ ) Pt-based dichalcogenides on  $\text{SiO}_2/\text{Si}$  wafer and Si wafer.
2. To develop large-area 2D/3D Schottky junctions by direct synthesis of Pt-based dichalcogenides using thermally assisted conversion in CVD.
3. To develop scalable and green technique to transfer nano-membranes of 2D TMDs and non-layered covalently-bonded 3D material onto arbitrary substrates.
4. To realize large-area, high-performance photosensitive devices based on directly synthesized 2D/3D Schottky junctions and van der Waals assembly technique.

### *Dissertation Overview*

Chapter two starts with the methods and techniques used to obtain large-area high-quality Pt-based dichalcogenides with defined structural and electrical properties controlled by Pt-seed layer thickness.

Having developed these growth techniques on various substrates, chapter three presents the development of 2D/3D Schottky junction devices based on Pt-based dichalcogenides using direct synthesis method.

Chapter four presents the post-growth tuning of Pt-based dichalcogenides based on plasma-driven chalcogen defect engineering. We present semiconducting to metallic transition in 2D PtSe<sub>2</sub> and provide theoretical background behind it.

In chapter five, we present the application of the 2D PtSe<sub>2</sub>/3D Si Schottky junction diode for solar cell application. We present flexible solar cells developed by directly synthesizing 2D PtSe<sub>2</sub> on silicon wafer. We explored the temperature-variant electrical property of these Schottky junctions and photovoltaic performance in rigid and flexible conditions.

In chapter six, we present the application of the 2D PtTe<sub>2</sub>/3D Si Schottky junction diode for solar cell application. We unveiled improved performance upon replacing PtSe<sub>2</sub> with PtTe<sub>2</sub>. Furthermore, we explored the performance of these Schottky diode junctions as visible-light photodetectors and unveiled critical parameters such as specific detectivity, responsivity and response speed. We also present unique water-droplet enhanced light-focusing to achieve improved photovoltaic performance owing to large hydrophobicity presented by 2D PtTe<sub>2</sub>.

In chapter seven, we explored the application of 2D PtTe<sub>2</sub>/3D Si Schottky junction device for near-infrared to mid-infrared photodetection. We present several electrical and optical characterization to probe into the performance of these devices.

Chapter eight presents the development of water-assisted delamination method of nano-membranes of 2D TMDs and covalently bonded non-layered material. We prepared hetero-materials of 2D PtTe<sub>2</sub> and 3D PtS and unveiled their performance in near-infrared photodetection.

Chapter nine concludes the dissertation and the future directions that need to be explored to realize

Pt-based dichalcogenides for photo-sensitive applications fully.

## **CHAPTER 2: LARGE-AREA DIRECT SYNTHESIS OF PLATINUM-BASED DICHALCOGENIDES**

The contents of this chapter have been published in:

M.Wang, T.-J. Ko, M. S. Shawkat, S. S. Han, E. Okogbue, H.-S. Chung, T.-S. Bae, S. Sattar, J. Gil, C. Noh, K. H. Oh, Y. Jung, J.A. Larsson, and Y. Jung, “Wafer-scale Growth of 2D PtTe<sub>2</sub> with Layer Orientation Tunable High Electrical Conductivity and Superior Hydrophobicity,” ACS Applied Materials Interfaces, vol. 12, no. 9, pp. 10839-10851, 2020.

M. S. Shawkat, H.-S. Chung, D. Dev, S. Das, T. Roy, and Y. Jung, “Two-Dimensional/Three-Dimensional Schottky Junction Photovoltaic Devices Realized by the Direct CVD Growth of vdW 2D PtSe<sub>2</sub> Layers on Silicon,” ACS Applied Materials Interfaces, vol. 11, no. 30, pp. 27251-27258, 2019.

### **Introduction**

Previous works on TMDs based on noble metals resulted in small-sized 2D TMDs (i.e., typically  $\sim 5\text{-}20\ \mu\text{m}$ ) and involved temperatures (700-1000 °C).[45, 46, 52, 53] Additionally, these methods result in spatially non-uniform layer thickness and non-uniform surface coverage. To ensure the batch fabrication of identical devices with reliable and repeatable performance, uniform thickness control and surface coverage is crucial. Therefore these growth methods severely impede the commercialization of these noble metal-based 2D TMDs. Additionally, the synthesis temperatures are quite high, almost on par with those of Mo- or W-based 2D TMDs (e.g., 2D MoS<sub>2</sub>) even though the melting temperature of Pt is much lower than that of refractory metals (e.g., Mo). Therefore, these materials fail to meet the back-end-of-line Complementary metal–oxide–semiconductor (CMOS)

processing temperature budget. In order to realize large-area noble metal-based 2D TMDs layers, we adopted thermally assisted conversion (TAC)-based synthesis method in a chemical vapor deposition (CVD) tube furnace at a temperature of  $\sim 400$  °C.[5–7] A previous study by Han et al. revealed thickness-controlled 2D PtSe<sub>2</sub> layers with uniform coverage on SiO<sub>2</sub>/Si wafer. Using this method, they achieved high-quality thickness-controlled 2D PtSe<sub>2</sub> of uniform coverage on SiO<sub>2</sub>/Si wafer.[44] Han et al. observed that the 2D PtSe<sub>2</sub> layers align themselves horizontally in smaller thicknesses of 2D PtSe<sub>2</sub> whereas, in higher thickness, 2D PtSe<sub>2</sub> layers align themselves vertically.

Additionally, through electrical characterization, it was unveiled that 2D PtSe<sub>2</sub> has a transition in electrical transport property where it becomes more metallic from semiconducting as the thickness of the Pt precursor layer is increased.[44] 2D PtTe<sub>2</sub> is another Pt-based 2D dichalcogenide emerging material and has received much attention.[56–58] An exceptionally high electrical conductivity of  $\sim 10^6$ – $10^7$  S/m was observed in chemically synthesized PtTe<sub>2</sub> crystals. The 2D PtTe<sub>2</sub> layers synthesized by these methods resulted in small sizes of  $\sim 5$ – $20$   $\mu$ m.

This chapter reports large-area and low-temperature synthesis of 2D PtSe<sub>2</sub> and PtTe<sub>2</sub> of controlled thickness and layer orientation using TAC-based synthesis method in a CVD tube furnace. Additionally, desired electrical transport property can be obtained by controlling the Pt precursor thickness. This method can be generalized to synthesize 2D PtSe<sub>2</sub> and 2D PtTe<sub>2</sub> on Si, SiO<sub>2</sub>/Si and polyimide substrate.

## Experimental Method

Figure 2.1 presents the schematic representation of the experimental setup for synthesizing Pt-based 2D TMD. A platinum seed layer of required thickness was deposited onto the desired substrate by electron beam evaporation at an evaporation rate of  $\sim 0.05$ – $0.15$  Å/s. The substrates were

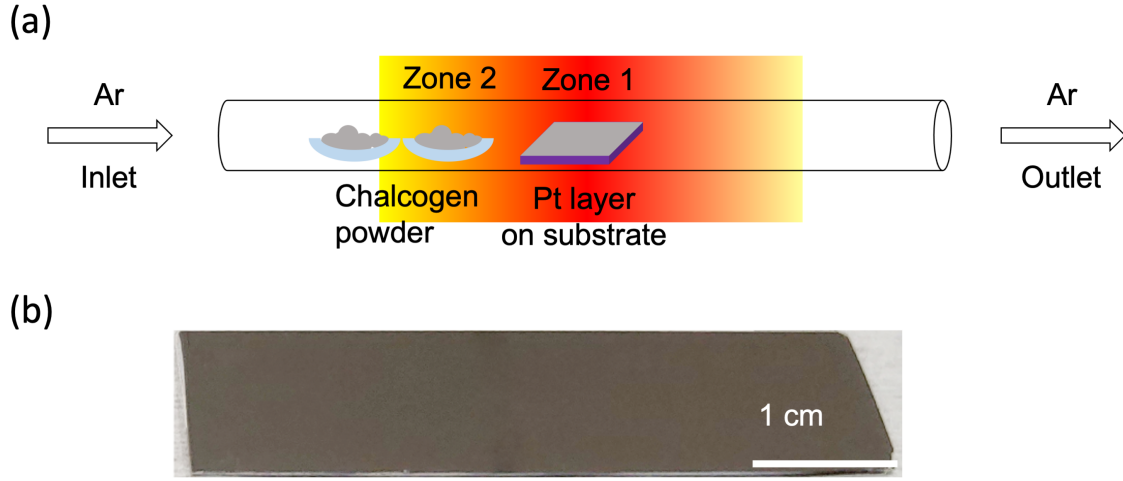


Figure 2.1: (a) Schematic illustration of quartz tube CVD furnace used for thermally assisted conversion of transition metal into transition metal dichalcogenide. (b) Image of a large-area  $\text{PtTe}_2$  synthesized on  $\text{SiO}_2/\text{Si}$  substrate. Adapted with permission from reference.[5]

then placed inside a quartz tube CVD furnace with an alumina boat containing the chalcogen powder placed in the furnace upstream side (temperature  $\sim 200^\circ\text{C}$ ). Ar gas purging was carried out until a base pressure of  $\sim 1$  mTorr was reached. The temperature inside the furnace was subsequently ramped up to  $400^\circ\text{C}$  at a rate of  $7.6^\circ\text{C}/\text{min}$  was maintained at  $400^\circ\text{C}$  for another 50 min. Ar gas of 100 standard cubic centimeters per minute (SCCM) flow rate was maintained during the growth, making the pressure inside the quartz tube  $\sim 80$  mTorr. Figure 2.1 b presents a digital camera image of large area  $\text{PtTe}_2$  synthesized on  $\text{SiO}_2/\text{Si}$  substrate.

### Thickness Dependent 2D Layer Orientation Transition

We systematically grew 2D  $\text{PtTe}_2$  layers by tellurizing Pt films of varying thickness on  $\text{SiO}_2/\text{Si}$  wafer and characterized their morphological transition. Figure 2.2 a–c illustrates the morphology of 2D  $\text{PtTe}_2$  layers obtained with Pt thin films in three different thickness regimes, i.e., small (e.g.,  $\sim 0.5$  nm) for Figure 2.2 a, intermediate (e.g.,  $\sim 1\text{--}3$  nm) for Figure 2.2 b, and large (e.g.,  $> 6$  nm)

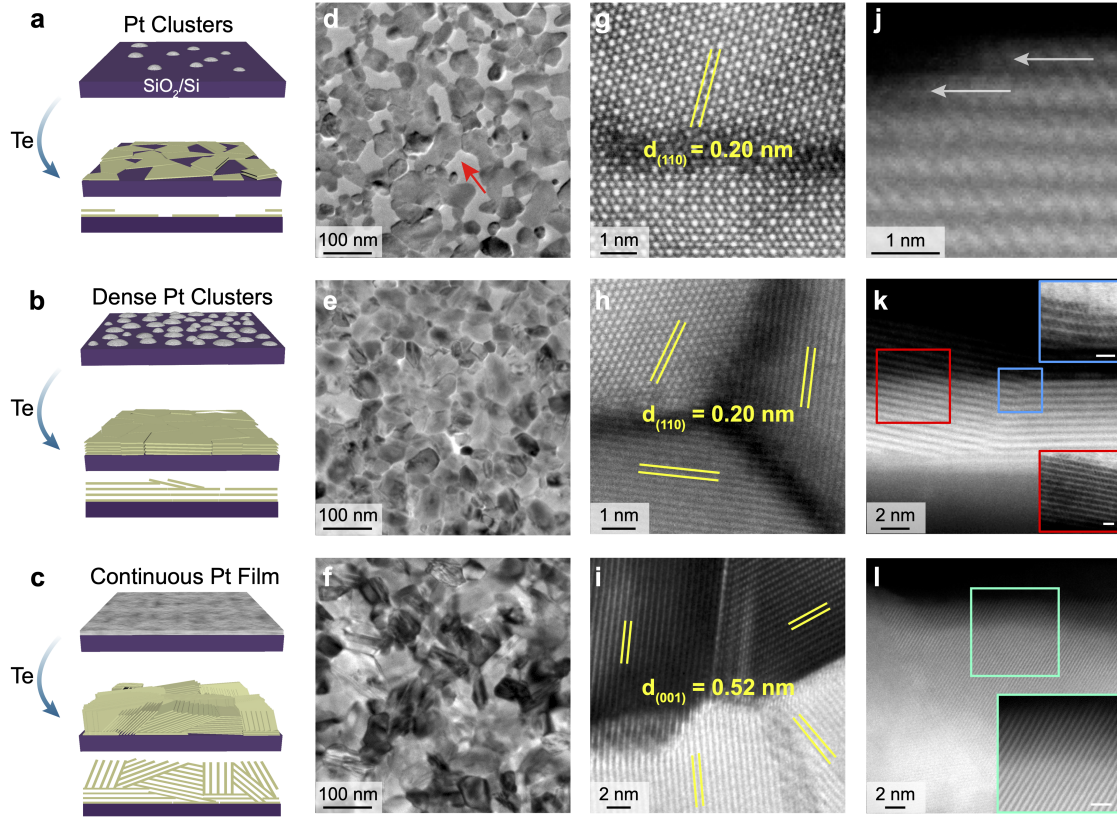


Figure 2.2: (a) Schematics for growth characteristics of 2D PtTe<sub>2</sub> layers obtained by tellurizing (a) scattered Pt nanoclusters, (b) dense Pt nanoclusters, and (c) continuous Pt films. (d-f) HAADF-STEM images of (d) holey layers with the pores indicated by the red arrow, (e) continuous layers, and (f) continuous layers with pronounced imaging contrast. (g-i): High-resolution HAADF-STEM images of (g) (110) lattice fringes in crystalline grains with a grain boundary, (h) (110) lattice fringes from crystalline 2D basal planes of three distinct orientations, and (i) (001) lattice fringes denoting 2D layer vertical orientation. (j-l): Cross-sectional STEM images of (j) edge-terminated horizontally aligned 2D layers, (k) reorientation of 2D layers along with the top and bottom insets corresponding to the blue and red boxed regions, and (l) vertically aligned 2D layers along with the inset corresponding to the green boxed region. The scale bars of the insets are 1 nm. Adapted with permission from Reference [5]

for Figure 2.2 c. These values denote the "nominal" thickness of deposited Pt films set by their e-beam evaporation conditions. Its correlation with the experimentally verified actual thickness of 2D PtTe<sub>2</sub> layers is to be presented in the following section.

In conjunction with the thickness variation of Pt films, three different growth modes have been observed. Growth mode (i) in Figure 2.2 a: Holey PtTe<sub>2</sub> films composed of horizontally aligned 2D layers are obtained by tellurizing Pt films of  $\sim 0.5$  nm thickness. This is a consequence that depositing Pt films of such a small thickness form scattered Pt nanoclusters of low areal density (top). As a result, 2D PtTe<sub>2</sub> layers grow without entirely covering the substrate surface (mid and bottom). Growth mode (ii) in Figure 2.2 b: Continuous PtTe<sub>2</sub> films composed of all horizontally aligned 2D layers are obtained by tellurizing Pt films of  $\sim 1\text{--}3$  nm thickness. Tellurizing Pt nanoclusters of a much higher area density (top) convert them to continuous 2D PtTe<sub>2</sub> layers, which laterally expand, covering the free spaces on the substrate (mid and bottom). Growth mode (iii) in Figure 2.2 c: Continuous PtTe<sub>2</sub> films constituting a mixture of horizontally and vertically aligned 2D layers are obtained by tellurizing continuous Pt films of  $> 6$  nm thickness (top). Conversion of the continuous Pt films to 2D PtTe<sub>2</sub> layers involves a significant volume expansion since Pt atoms take in additional Te atoms as well as forming vdW physical gaps. Accordingly, growing 2D PtTe<sub>2</sub> layers will experience a substantial amount of accumulating strain, and some of their crystalline domains will prefer to reorient 2D layers in a vertical manner to release the strain (mid and bottom). This growth event is similar to the recently observed and verified strain-driven vertical growth of 2D MoS<sub>2</sub> layers.[59]

Figure 2.2 d–l presents scanning transmission electron microscopy (STEM) characterization to verify the thickness-dependent 2D PtTe<sub>2</sub> layer morphological transition. Figure 2.2d–f shows low-magnification STEM images of 2D PtTe<sub>2</sub> layers obtained from various Pt thicknesses of  $\sim 0.5$ ,  $\sim 3$ , and  $\sim 15$  nm. Figure 2.2 d reveals that 2D PtTe<sub>2</sub> layers indeed exhibit rich porosity (red arrow), while the others show their continuous film morphology. 2D PtTe<sub>2</sub> layers in Figure 2.2 d present an average domain size of  $\sim 50$  nm with a spatial coverage ratio of  $\sim 74\%$ , supporting their conversion from scattered Pt nanoclusters of low density illustrated in Figure 2.2 a. It is also noted that 2D PtTe<sub>2</sub> layers grown from the larger Pt thickness (Figure 2.2 e) exhibit higher STEM

imaging contrast over the other (Figure 2.2 f), indicating significant inhomogeneity of 2D layer orientation. Figure 2.2 g–i presents high angle annular dark-field (HAADF)-STEM characterization of 2D PtTe<sub>2</sub> layers obtained with various Pt thickness.

Figure 2.2 g shows a high-resolution HAADF-STEM image obtained from holey 2D PtTe<sub>2</sub> layers, revealing highly crystalline domains along with a grain boundary. The measured lattice spacing of 0.20 nm corresponds to (110) lattice fringes exposed on PtTe<sub>2</sub> basal planes, indicative of horizontally aligned 2D layers. Figure 2.2 h shows a representative high-resolution HAADF-STEM image of continuous 2D PtTe<sub>2</sub> layers obtained from Pt thin films of intermediate thickness. The image reveals three crystalline domains of distinct crystallographic orientation, while (110) lattice fringes are uniformly observed in each grain. This observation indicates that horizontally aligned individual 2D layers of distinct orientation laterally "stitch" in an in-plane manner, evidencing their layer-by-layer growth nature. This study is fully consistent with our group's previous study on thickness-dependent 2D layer transition in 2D PtSe<sub>2</sub>.<sup>[44]</sup>

### Thickness Dependent Electrical Transport

We electrically characterized the carrier transport properties of horizontally- vs. vertically aligned 2D PtSe<sub>2</sub> layers presented in Figure 2.3. We fabricated field-effect transistors (FETs) employing 2D PtSe<sub>2</sub> layers as active channels and identified their carrier transport types by characterizing back gate responses, as illustrated in Figure 2.3 a. FET characterization results for both 2D layer orientation are presented in Figure 2.3 b–e; i.e. horizontally-aligned 2D PtSe<sub>2</sub> layers in Figure 2.3 b and Figure 2.3 c and vertically-aligned 2D PtSe<sub>2</sub> layers in Figure 2.3 d and e, respectively. We note distinct carrier transport characteristics depending on the layer orientation of 2D PtSe<sub>2</sub>. Figure 2.3 b shows the FET transfer characteristics of drain-source current vs. voltage ( $I_{ds} - V_{ds}$ ) with varying back-gate voltage ( $V_g$ ) obtained from horizontally-aligned 2D PtSe<sub>2</sub> layers. It

is observed that  $I_{ds}$  monotonically decreases with increasing  $V_g$  at given  $V_{ds}$  values, indicating that horizontally-aligned 2D PtSe<sub>2</sub> layers exhibit p-type semiconductor transport characteristics. Figure 2.3 c shows the corresponding  $I_{ds}$ - $V_g$  transfer characteristics obtained at a fixed  $V_{ds}$  of 2V, which reveals hole-transport FET gate responses. These FET characterization results combined confirm that horizontally-aligned 2D PtSe<sub>2</sub> layers prepared with thin Pt (0.5 nm in this case) are intrinsically p-doped semiconductors.

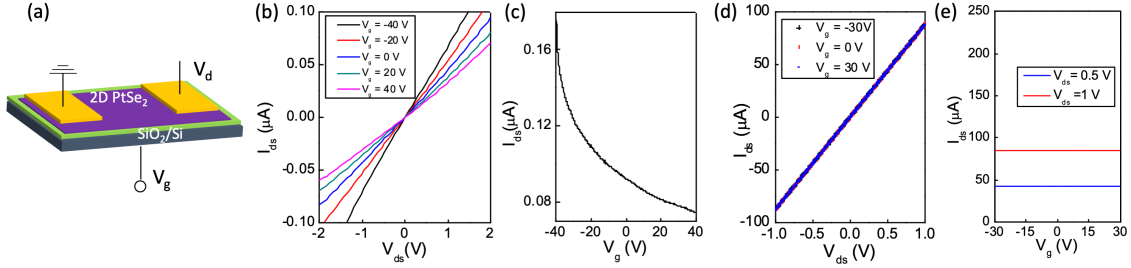


Figure 2.3: Electrical characterizations of vertically aligned 2D PtSe<sub>2</sub> layers. (a) Schematic of a back-gated FET device based on vertically aligned 2D PtSe<sub>2</sub> layers. (b, c) Characterization of a horizontally-aligned 2D PtSe<sub>2</sub> layers-based FET demonstrating (b)  $I_{ds}$ - $V_{ds}$  and (c)  $I_{ds}$ - $V_g$  transfer characteristics. (d, e) Characterization of a vertically-aligned 2D PtSe<sub>2</sub> layers-based FET demonstrating (d)  $I_{ds}$ - $V_{ds}$  and (e)  $I_{ds}$ - $V_g$  transfer characteristics. Adapted with permission from Reference [6]

Interestingly, vertically-aligned 2D PtSe<sub>2</sub> layers exhibit drastically distinguishable transport characteristics. Figure 2.3 d and Figure 2.3 e show the FET transfer characteristics of  $I_{ds}$ - $V_{ds}$  and  $I_{ds}$ - $V_g$  obtained from vertically-aligned 2D PtSe<sub>2</sub> layers, respectively. Unlike the horizontally-aligned 2D PtSe<sub>2</sub> layers displaying p-type semiconducting transports, vertically-aligned 2D PtSe<sub>2</sub> layers do not exhibit any FET gate response indicating they are highly metallic; i.e., transfer characteristics of  $I_{ds}$ - $V_{ds}$  completely overlap irrespective of  $V_g$  (Figure 2.3 d), and  $I_{ds}$  does not change as a function of  $V_g$  (Figure 2.3 e). This observation of orientation-dependent semiconducting-to-metallic transition in 2D PtSe<sub>2</sub> layers is consistent with our previous studies.[44] As the focus

of the present study is on exploring 2D PtSe<sub>2</sub>/Si Schottky junctions, we have deliberately chosen vertically-aligned 2D PtSe<sub>2</sub> layers with metallic transport characteristics to ensure good Schottky junction properties throughout all measurement data presented in a later section.

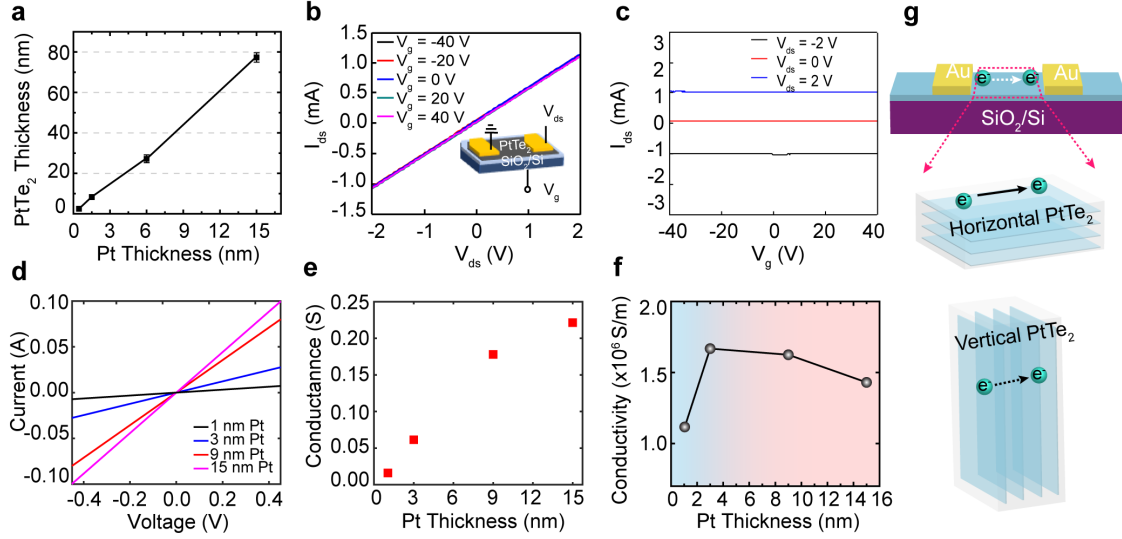


Figure 2.4: Electrical characterizations of vertically aligned 2D PtTe<sub>2</sub> layers. (a) Thickness of 2D PtTe<sub>2</sub> layers as a function of Pt thickness. (b, c) Back-gate FET measurements of 2D PtTe<sub>2</sub> layers obtained from  $\sim 0.5$  nm Pt thickness, showing (b)  $I_{ds}$ - $V_{ds}$  and (c)  $I_{ds}$ - $V_g$  transfer characteristics. (d)  $I$ - $V$  curves of 2D PtTe<sub>2</sub> prepared from various Pt thicknesses. (e) Conductance as a function of Pt thickness. (f) Conductivity as a function of Pt thickness showing a presence of its thickness-dependent maximum point. The junction of the blue and red shading represents a transition of horizontal-to-vertical layer orientation. (g) Schematics of electron transports in horizontally vs. vertically aligned 2D PtTe<sub>2</sub> layers. Adapted with permission from [5]

We also studied the thickness-dependent electrical transport property of 2D PtTe<sub>2</sub> layers. We first identified the relationship of Pt film thickness and resulting 2D PtTe<sub>2</sub> layer thickness by performing atomic force microscopy (AFM) height profile measurements, as presented in Figure 2.4 a. We note that the actual thickness of 2D PtTe<sub>2</sub> layers is  $\sim 5$  times larger than the nominal thickness of Pt films, set by the deposition conditions inherent to our e-beam evaporator. We then investigated the carrier type of as-grown 2D PtTe<sub>2</sub> layers on SiO<sub>2</sub>/Si wafers by characterizing their field-effect transistor (FET) gate responses. From various theory studies[60], it is well established that 2D

PtTe<sub>2</sub> layers do not possess bandgap energies even in a few-layer form.

We focused our measurements on 2D PtTe<sub>2</sub> layers obtained from Pt films of a very small thickness (e.g.,  $\sim 0.5$  nm corresponding to a 2D layer thickness of  $\sim 2.5$  nm), as presented in Figure 2.4 b, c. Figure 2.4 b shows transfer characteristics of drain-source voltage ( $V_{ds}$ ) vs. drain-source current ( $I_{ds}$ ) with varying back-gate voltage ( $V_g$ ), and Figure 2.4 c shows  $I_{ds}$ - $V_g$  at varying  $V_{ds}$ . As anticipated, 2D PtTe<sub>2</sub> layers reveal strong metallic characteristics, as manifested by the complete overlap of  $I_{ds}$  -  $V_{ds}$  irrespective of  $V_g$  (Figure 2.4 b) and the  $V_g$ -independent  $I_{ds}$  (Figure 2.4 c). The inset in Figure 2.4 b illustrates a schematic of 2D PtTe<sub>2</sub> layer-based FET in a back-gate configuration. Having confirmed the intrinsically metallic nature of 2D PtTe<sub>2</sub> layers, we investigated their thickness-dependent electron transports. For rigorous quantification, we precisely defined the geometrical dimension of 2D PtTe<sub>2</sub> layers by AFM characterization of their actual thickness (2.4 a) and by patterning gold (Au) electrodes with an identical channel length (width:  $200\ \mu\text{m}$ , spacing:  $100\ \mu\text{m}$ ).

Figure 2.4 d shows I-V characteristics obtained from 2D PtTe<sub>2</sub> layers of varying Pt thickness, and Figure 2.4 e presents the corresponding electrical conductance obtained from their tangential slopes. Electrical conductivity was determined by combining the geometrical dimension with the measured conductance, and its thickness-dependency is presented in Figure 2.4 f. The conductivity steadily increases with increasing Pt thickness, yielding the highest value of  $\sim 1.7 \times 10^6$  S/m at  $\sim 3$  nm thickness. This thickness is the critical point where 2D PtTe<sub>2</sub> multilayers exhibit horizontally aligned layer orientation with full surface coverage and high structural homogeneity. The lower conductivity value from a smaller Pt thickness is attributed to their intrinsically holey morphology (Figure 2.4 a, d). Beyond this critical point, vertically aligned 2D layers start to emerge. The conductivity gradually decreases with further increasing thickness, reaching  $\sim 1.4 \times 10^6$  S/m at Pt thickness of 15 nm. This thickness-dependent conductivity decrease well agrees with the thickness-dependent transition of 2D layer orientation, i.e., the emergence of vertically aligned 2D

layers beyond a certain critical thickness continuously becomes more pronounced with further increasing thickness. This suppressed conductivity from the vertically aligned 2D layers is attributed to the increasing contribution of “out-of-plane” transports of electrons across vdW physical gaps, as illustrated in Figure 2.4 g. This observation is well supported by previous experimental and theoretical studies that report much higher energy barriers for the electrons undergoing out-of-plane transports across vdW gaps over those traveling in an “in-plane” manner.[61, 62]

It is also worth mentioning that the overall conductivity values are on the order of  $10^6$  S/m, highly comparable to those of previously reported 2D PtTe<sub>2</sub> layers of much smaller dimensions, which fall in the range of  $3.3\text{--}6.4 \times 10^6$  S/m.[45, 46, 53] Moreover, these conductivity values are significantly higher than those of any other 2D TMD layers, e.g., the highest reported being vanadium diselenide (VSe<sub>2</sub>) with a conductivity of  $\sim 1 \times 10^6$  S/m. [63] Such an unusual combination of extremely high electrical conductivity, wafer-scale dimension, and tunable geometry offers numerous opportunities beyond electronics applications, e.g., electrochemical or catalytic applications requiring high electrical conductivity coupled with large structural porosity and surface area.

## CHAPTER 3: CONSTRUCTION OF 2D/3D SCHOTTKY JUNCTIONS

The contents of this chapter have been published in:

M. S. Shawkat, H.-S. Chung, D. Dev, S. Das, T. Roy, and Y. Jung, “Two-Dimensional/Three-Dimensional Schottky Junction Photovoltaic Devices Realized by the Direct CVD Growth of vdW 2D PtSe<sub>2</sub> Layers on Silicon,” ACS Applied Materials Interfaces, vol. 11, no. 30, pp. 27251-27258, 2019.

M. S. Shawkat, T. A. Chowdhury, H.-S. Chung, S. Sattar, T.-J. Ko, J. A. Larsson, and Y. Jung, “Large-area 2D PtTe<sub>2</sub>/Silicon Vertical-Junction Devices with Ultrafast and High-sensitivity Photodetection and Photovoltaic Enhancement by Integrating Water Droplets,” Nanoscale, vol. 12, no. 45, pp. 23116-23124, 2020.

### Introduction

Having successfully demonstrated large-area low-temperature synthesis of 2D PtSe<sub>2</sub> and 2D PtTe<sub>2</sub> with metallic property on SiO<sub>2</sub>/Si wafer, we further looked into directly synthesizing 2D PtSe<sub>2</sub> on Si wafer. Given that Si is a highly matured technology, it is highly timely to study the application of 2D PtSe<sub>2</sub> and 2D PtTe<sub>2</sub> directly integrated on silicon. In previous section we confirmed highly metallic nature of 2D PtSe<sub>2</sub> synthesized on SiO<sub>2</sub>/Si wafer with Pt precursor thickness  $\sim 4.5$  nm. Additionally, we confirmed high-quality synthesis of PtTe<sub>2</sub> on SiO<sub>2</sub>/Si wafer with highly metallic nature even with a Pt precursor thickness of  $\sim 0.5$  nm.

In this chapter we demonstrated 2D/3D Schottky junction devices based on vertically aligned metallic 2D PtSe<sub>2</sub> and 2D PtTe<sub>2</sub> layers integrated on Si wafers. We directly grew 2D PtSe<sub>2</sub> and 2D PtTe<sub>2</sub> layers of controlled orientation and carrier transport characteristics via a low-temperature

chemical vapor deposition process and investigated a comprehensive set of material parameters.

### Process of Fabrication of 2D/3D Schottky Junctions

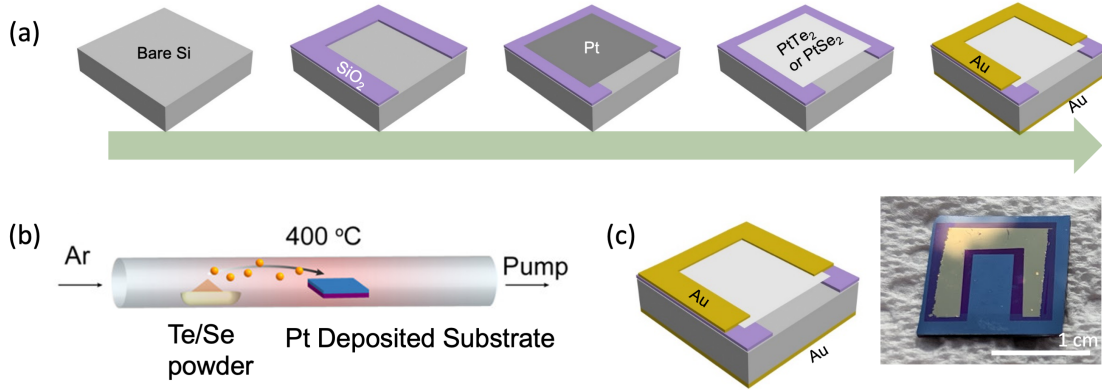


Figure 3.1: Fabrication of 2D TMD/Si Schottky devices. (a) Illustration of step-by-step procedures to fabricate a 2D PtSe<sub>2</sub>/Si or 2D PtTe<sub>2</sub>/Si Schottky device (b) Schematic diagram describing thermally assisted conversion assisted method used to synthesize 2D PtSe<sub>2</sub> or or 2D PtTe<sub>2</sub>. (c) Schematic (left) and digital camera image (right) of the final device (c) Representative image of a completed 2D PtSe<sub>2</sub>/Si Schottky device. Adapted with permission from Reference [7], [5]

Figure 3.1 a illustrates the sequential procedures for the device fabrication, starting with the patterned deposition of silicon dioxide (SiO<sub>2</sub>) on p-doped Si wafers (resistivity  $\sim 1\text{-}5\ \Omega\text{cm}$ ). Pt thin films of controlled thickness are selectively deposited on the wafers via an electron beam evaporator using a shadow mask. Subsequently, 2D PtX<sub>2</sub> (PtSe<sub>2</sub>/PtTe<sub>2</sub>) layers are grown at 400 °C through the CVD selenization/tellurization method developed in our previous studies,[44] defining the lateral dimension of PtX<sub>2</sub>/Si vertical heterojunctions. Lastly, gold (Au) electrodes are selectively deposited on the top PtX<sub>2</sub>/SiO<sub>2</sub> side as well as the wafer bottom side. 2D PtX<sub>2</sub> layers are observed to exhibit two distinct layer orientations; horizontal and vertical, which is controlled by CVD conditions – verified in previous section. Figure 3.1 b shows the schematic representation of thermally assisted conversion method of prepared Pt-deposited Si wafer which is placed in the

center of a quartz tube CVD furnace with a pre-loaded alumina boat containing selenium/tellurium powders at the furnace upstream side. The CVD furnace is pumped down to a base pressure of  $\sim 1\text{mTorr}$ , followed by purging with argon (Ar) gas to remove any residual impurities inside the quartz tube. Subsequently, it is heated up to  $400\text{ }^{\circ}\text{C}$  in 50 min for a dwell time of 50 min under a continuous flow of Ar gas. After the CVD reaction, the furnace is naturally cooled down to room temperature, and conversion of Pt to 2D  $\text{PtX}_2$  layers is confirmed by noticeable color change in the pre-Pt-deposited area. Figure 3.1 c shows a schematic diagram and a photo image of a complete Schottky junction device. It is worth mentioning that the low growth temperature of  $400\text{ }^{\circ}\text{C}$  for 2D  $\text{PtX}_2$  layers is comparable to the thermal budget back-end-of-line (BEOL) temperature adopted in complementary metal oxide semiconductor (CMOS) processes,[64] indicating potential advantages of CMOS-compatible large-scale manufacturing employing 2D  $\text{PtX}_2$  layers.

### Direct Synthesis of $\text{PtSe}_2$ on Silicon Substrate

#### *Structural and Chemical Characterization*

The strong metallic nature of 2D  $\text{PtSe}_2$  layers projects metal/semiconductor Schottky junction based on “mixed-dimensional” vdW heterostructures[65] when they are interfaced with three-dimensional (3D) semiconductors. The most well-established form of 2D/3D vdW heterostructure-based Schottky junctions can be found in graphene/semiconductor heterojunctions such as mechanically integrated graphene on top of silicon (Si). Although these graphene/Si Schottky junctions are recently gaining significant interest in a variety of electronic applications such as photovoltaic devices,[66, 67] their preparation requires the mechanical separation of high-temperature CVD-grown graphene from growth substrates (e.g., copper (Cu)) and its subsequent transfer to Si wafers.[68, 69, 69] Accordingly, the process stands a high chance of introducing unwanted contamination throughout the chemical/mechanical treatment of graphene for delamination and inte-

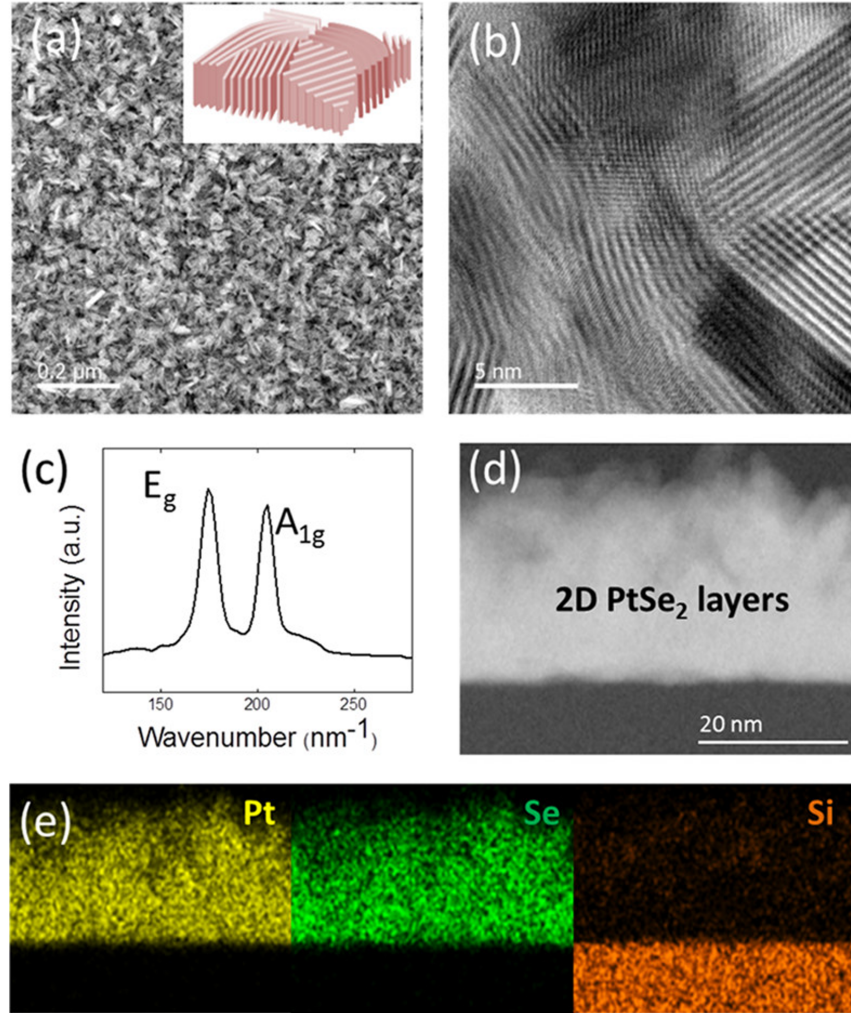


Figure 3.2: Structural and chemical characterizations of vertically aligned 2D PtSe<sub>2</sub> layers. (a–e) Structural and chemical characterizations: (a, b) TEM characterization of vertically aligned 2D PtSe<sub>2</sub> layers in (a) low-magnification and (b) high-magnification views. (c) Raman spectroscopy characterization. (d) Cross-sectional STEM image of vertically aligned 2D PtSe<sub>2</sub> layers. (e) STEM-EDS elemental mapping images corresponding to (d). Adapted with permission from Reference [6].

gration. In this work we achieved high quality large-area low-temperature direct synthesis of 2D PtSe<sub>2</sub> layers on silicon substrate. Therefore, developing process to directly synthesize large-area 2D PtSe<sub>2</sub> layers on silicon substrate is crucial.

Microstructures and atomic-bonding natures of the 2D PtSe<sub>2</sub> layers with Pt precursor thickness 4.5 nm directly grown on Si wafers were characterized by transmission electron microscopy (TEM) and Raman spectroscopy. We have previously identified that two distinguishable 2D layer orientations of horizontal and vertical can be achieved by CVD-selenizing Pt films of controlled thickness;[44] horizontally aligned 2D PtSe<sub>2</sub> layers are grown by the CVD selenization of thin Pt (typically <1 nm), while vertically aligned 2D layers are achieved with thick Pt (typically >4 nm). In this work, we have deliberately grown vertically aligned 2D PtSe<sub>2</sub> layers only as they present strong metallic transports suitable for Schottky junction formation-details are to be confirmed in the next section. Figure 3.2 shows low-magnification and high-resolution scanning TEM (HR-STEM) images of vertically aligned 2D PtSe<sub>2</sub> layers, respectively. The HR-STEM image in 3.2 b reveals that vertically aligned 2D PtSe<sub>2</sub> layers expose their 2D layer edges on the surface consistent with previous studies,[44] indicating the good morphological controllability of our CVD process.

Figure 3.2 c shows the Raman spectra of vertically aligned 2D PtSe<sub>2</sub> layers exhibiting two characteristic peaks corresponding the in-plane  $E_g$  and out-of-plane  $A_{1g}$  vibration modes.[70] It is noted that vertically aligned 2D PtSe<sub>2</sub> layers exhibit  $E_g$  and  $A_{1g}$  peaks of comparable intensity, indicating a significant enhancement of out-of-plane vibration, similarly observed with vertically aligned 2D MoS<sub>2</sub> layers.[54] Figure 3.2 d shows a cross-sectional STEM image of vertically aligned 2D PtSe<sub>2</sub> layers on a growth substrate, indicating that they are ~30 nm thick. Figure 3.2 e shows the corresponding energy-dispersive X-ray spectroscopy (EDS) elemental mapping images, revealing the spatial distribution of Pt, Se, and Si. From field-effect transistors (FETs) employing 2D PtSe<sub>2</sub> layers as active channels and identified their carrier transport types by characterizing FET back-gate responses we confirmed in previous section that 2D PtSe<sub>2</sub> is highly metallic with Pt precursor thickness 4.5 nm, consistent with our previous studies.[44]

## Direct Synthesis of PtTe<sub>2</sub> on Silicon Substrate

### Structural and Chemical Characterization

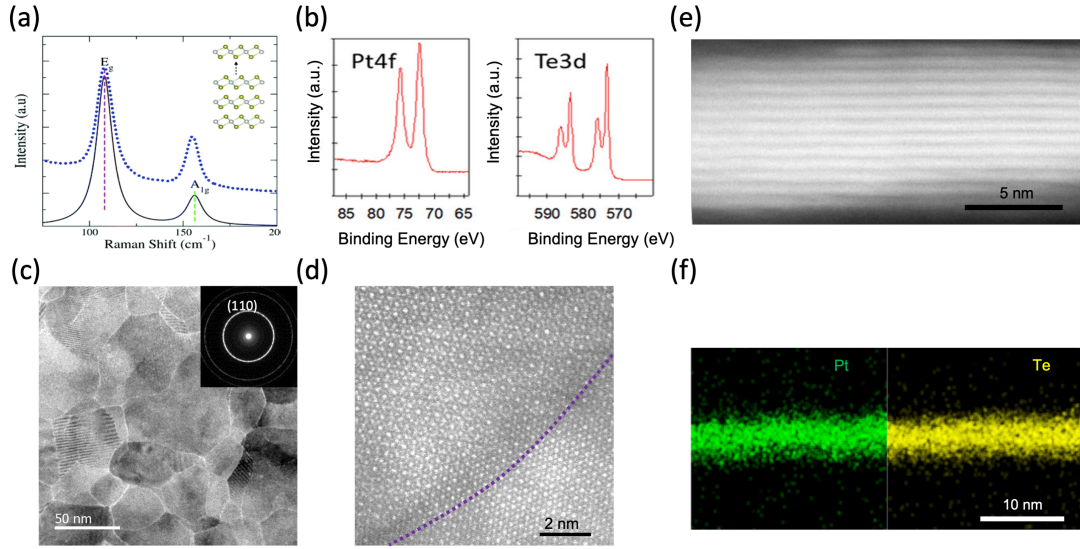


Figure 3.3: Material characterization of 2D PtTe<sub>2</sub> synthesized on Silicon. (a) Raman spectroscopy characterization of few-layered 2D PtTe<sub>2</sub>, comparing the theoretically calculated spectrum (black solid line) with the experimentally determined one (blue dotted line). (b) XPS spectra of Pt 4f (left) and Te 3d (right) core levels obtained from 2D PtTe<sub>2</sub> layers grown on a Si wafer. (c) Plane-view STEM image of 2D PtTe<sub>2</sub> layers and the corresponding SAED pattern in the inset. (d) Plane-view HR-STEM image revealing two neighboring stitching grains, separated by the grain boundary (purple dotted curve). (e) Cross-sectional HR-STEM image of 2D PtTe<sub>2</sub> multilayers. (f) Cross-sectional STEM-EDS elemental mapping images corresponding to (e). Adapted with permission from Reference [7], [8].

Figure 3.3 shows the structural/chemical characterization of the 2D PtTe<sub>2</sub> layers synthesized on silicon. Figure 3.3 a shows the Raman spectroscopy characterization of few-layered 2D PtTe<sub>2</sub> obtained by the CVD tellurization of Pt  $\sim$  0.3 nm, comparing experimentally determined (blue dotted line) vs. theoretically calculated (black solid line) characteristics. Two characteristic peaks of  $E_g$  and  $A_{1g}$  are noted, where  $E_g$  ( $A_{1g}$ ) peaks depict the in-plane (out-of-plane) vibrational modes

of Te atoms within the 2D layers, respectively. Excellent agreement is observed between these two spectra of experimental vs. theoretical in terms of their peak positions. X-ray photoelectron spectroscopy (XPS) was employed to confirm the successful growth of 2D PtTe<sub>2</sub> layers on top of Si wafers. The XPS spectra in Figure 3.3 b reveal core-energy level peaks of Pt 4f at 72.4 and 75.7 eV corresponding to 4f<sub>7/2</sub> and 4f<sub>5/2</sub>, respectively, which is fully consistent with the previous reports on 2D PtTe<sub>2</sub> layers.[53,71] Also, Te 3d core-energy level peaks corresponding to the Te(IV) oxidation state appear at 576 and 586.3 eV, as well as additional peaks of Te(0) appearing at 573.3 and 583.4 eV. This observation is also consistent with previous studies,[71, 72] further confirming the successful CVD growth of 2D PtTe<sub>2</sub> layers.

The atomic crystallinity of the CVD-grown 2D PtTe<sub>2</sub> layers was studied using a scanning transmission electron microscope (STEM). Figure 3.3 c presents the dark-field STEM image of the as-grown 2D PtTe<sub>2</sub> layers, unveiling a large number of polycrystalline grains. Each grain is individually “stitched” with respect to its neighbouring ones, achieving a high spatial homogeneity over the entire sample area. The inset in Figure 3.3 c is the corresponding selective area diffraction (SAED) pattern, showing the dominant appearance of the (110) PtTe<sub>2</sub> plane.[5] Figure 3.3 d shows the plane-view high-resolution STEM (HR-STEM) image of the polycrystalline 2D PtTe<sub>2</sub> layers, revealing two adjacent stitching grains separated by the grain boundary (purple curve). Each grain exhibits distinguishable Moire fringes, indicating vertical stacking of individual 2D layers with misaligned crystallographic orientation. Figure 3.3 e shows the cross-sectional HR-STEM image to reveal the well-defined van der Waals (vdW) gaps in vertically stacked 2D PtTe<sub>2</sub> layers, indicating their layer-by-layer growth. Figure 3.3 f shows the corresponding energy-dispersive X-ray spectroscopy (EDS) elemental mapping images, unveiling the spatial homogeneity of constituent elements.

## Conclusion

We fabricated large-area 2D PtSe<sub>2</sub>/3D Si and 2D PtTe<sub>2</sub>/3D Si Schottky junction diodes using direct synthesis method. We utilised thermally assisted conversion method to directly synthesize large-area 2D PtSe<sub>2</sub> and 2D PtTe<sub>2</sub> on silicon in a relatively low temperature of  $\sim 400$  °C. Finally, we carried out extensive material, chemical and structural characterization to verify high-quality growth of 2D PtSe<sub>2</sub> and PtTe<sub>2</sub> on Silicon.

## **CHAPTER 4: SEMICONDUCTING-TO-METALLIC CONVERSION IN WAFER-SCALE 2D PTSE<sub>2</sub> LAYERS BY PLASMA-DRIVEN CHALCOGEN DEFECT ENGINEERING**

The contents of this chapter have been published in:

M. S. Shawkat, J. Gil, S. S. Han, T.-J. Ko, M. Wang, D. Dev, J. Kwon, G.-H. Lee, K. H. Oh, H.-S. Chung, T. Roy, Y. Jung, Y. Jung, “Thickness-Independent Semiconducting-to-Metallic Conversion in Wafer-Scale Two-Dimensional PtSe<sub>2</sub> Layers by Plasma-Driven Chalcogen Defect Engineering,” ACS Applied Materials Interfaces, vol. 12, no. 12, pp. 14341-14351, 2020.

### **Introduction**

The co-existence of semiconducting and metallic phases within identical 2D PtSe<sub>2</sub> layers can be utilized for several novel applications, such as in-plane, atomically thin Schottky junctions with components of similar chemical composition,[73] unlike other 2D heterostructures based on laterally stitching layers of distinct compositions.[53, 74] Additionally, this semiconducting-metallic phase tenability is an “intrinsic” feature of 2D PtSe<sub>2</sub> layers set by their intrinsic crystallinity, i.e., layer thickness and/or orientation and can be controlled by their preparation methods such as chemical growth conditions.[6] These dissimilar carrier transport characteristics are particularly interesting for the contact engineering of 2D layers toward improving their Ohmic transports, i.e., atomically seamless Ohmic contacts within 2D layers.[75] Accordingly, it is of interest to develop post-growth methods to “externally” modulate such features in a spatially defined and controlled manner, which will greatly broaden the application versatility of 2D PtSe<sub>2</sub> layers. Towards this effort, structural engineering such as controlling defect concentrations via physical/chemical means

has been explored with conventional 2D TMD semiconductor layers including Mo or W disulfide ( $\text{MoS}_2$  or  $\text{WS}_2$ ) and diselenide ( $\text{MoSe}_2$  or  $\text{WSe}_2$ ).[76]

The atomic concentration of chalcogen vacancies is known to alter their electronic band structures, thereby resulting in altered carrier transport properties.[55,76] Theory suggests that a selective creation of chalcogen vacancies can contribute to forming unsaturated electrons surrounding transition metals acting as electron donors.[77] The prediction is consistent with recent experimental observations that corroborate the vacancy-driven closing of band-gap energies in 2D  $\text{WS}_2$  and  $\text{WSe}_2$  layers.[78] However, these approaches have been demonstrated with initially single-crystalline 2D flakes of small ( $\sim \mu\text{m}^2$ ) lateral dimensions and inhomogeneous spatial distribution/coverage. Accordingly, they are practically limited toward realizing the aforementioned opportunities for atomically thin circuitry, which should rely on “wafer-scale” 2D layers produced by mass production routes such as chemical vapor deposition (CVD). It is highly demanded to develop scalable methods to externally and controllably fabricate both semiconducting and metallic phases within identical 2D layers toward the direct writing of wafer-scale circuitry. The feasibility of such defect engineering for modulating carrier transports in large- area ( $>\text{cm}^2$ ) CVD-grown 2D  $\text{PtSe}_2$ , a relatively unexplored 2D material, with intrinsic polycrystallinity has remained largely unexplored. We aim to establish method to controllably tune the electronic transport property in specific region of large-area noble metal based 2D TMDs using a simple process.

We carried out controlled modulation of carrier transport properties in CVD-grown centimeter-scale 2D  $\text{PtSe}_2$  layers via argon (Ar) plasma irradiation. Two-dimensional (2D)  $\text{PtSe}_2$  layers are known to be metallic above a certain critical thickness (typically more than  $\sim 10$  nm), below which they prefer to possess semiconducting properties. We grew 2D  $\text{PtSe}_2$  layers of very small (a few nanometer) thickness and confirmed their intrinsic semiconducting characteristics. We then applied a controlled Ar-plasma irradiation to them and investigated the resulting carrier transport properties. It is observed that 2D  $\text{PtSe}_2$  layers display a transition from semiconducting to metallic

property due to Se deficiency after plasma treatment.

## Results and Discussion

### *Process of Plasma Treatment*

Figure 4.1 illustrates the process steps employed in the CVD growth of 2D PtSe<sub>2</sub> layers and their partially selected Ar-plasma irradiation. A Pt film of  $\sim 0.6$  nm was deposited on a SiO<sub>2</sub>/Si wafer by electron beam deposition (deposition rate:  $\sim 0.1$  Å/s), and it was then converted into 2D PtSe<sub>2</sub> layers via CVD selenization at 400 °C using the growth recipe developed in our laboratory.[6, 44] The as-grown 2D PtSe<sub>2</sub> layers exhibit a highly uniform morphology and thickness, entirely covering the original growth wafer, to be verified in the next section. A thermal release tape (TRT) was subsequently attached to the surface of the as-grown 2D PtSe<sub>2</sub> layers, and care was taken to ensure that there were no gaps between the tape and the 2D layers. Subsequently, the sample of TRT/2D PtSe<sub>2</sub>/SiO<sub>2</sub>/Si was immersed in deionized water, similar to the procedure demonstrated with 2D MoS<sub>2</sub> layers,[10] and a mechanical force was exerted to peel off the stack of TRT/2D PtSe<sub>2</sub> from the growth substrate. The separated stack was flipped over, exposing the 2D PtSe<sub>2</sub> layers on the top surface. Next, the 2D PtSe<sub>2</sub> layers were partially covered with a stainless steel shadow mask and were exposed to mild Ar plasma for controlled duration times. The partially plasma-treated sample was then transferred onto a fresh SiO<sub>2</sub>/Si wafer, and the TRT was subsequently removed upon heating at 80 °C. As a result, a lateral junction containing both pristine and plasma-treated areas was realized within identical 2D PtSe<sub>2</sub> layers. The aim of performing the Ar-plasma irradiation onto the 2D PtSe<sub>2</sub> layers “separated” from their underlying SiO<sub>2</sub>/Si growth wafers was to rule out any unwanted effects from the degradation of SiO<sub>2</sub> dielectric and metal contacts caused by the plasma irradiation. In fact, we have observed that “direct” Ar-plasma irradiation onto as-grown 2D PtSe<sub>2</sub>/SiO<sub>2</sub>/Si samples often leads to the degradation and instability of the underlying

SiO<sub>2</sub> dielectric and SiO<sub>2</sub>/metal contacts in electrical measurements.

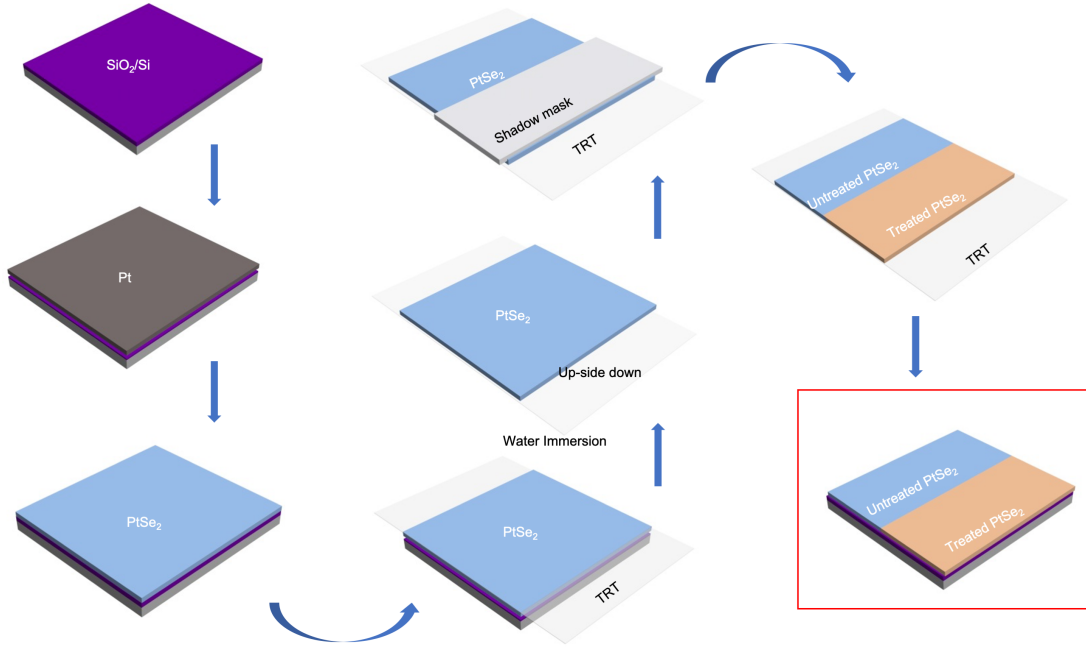


Figure 4.1: Schematic illustration for the preparation of Ar-plasma-treated and -untreated areas within identical 2D PtSe<sub>2</sub> layers. Adapted with permission from reference [9].

### *Structural and Chemical Characterization of As-Grown 2D PtSe<sub>2</sub>*

Figure 4.2 shows the structural and chemical analyses of as-grown 2D PtSe<sub>2</sub> layers prior to the Ar-plasma treatment. Figure 4.2 a presents an image of as-grown 2D PtSe<sub>2</sub> layers on a SiO<sub>2</sub>/Si wafer with a size of  $> 1 \text{ cm}^2$ , prepared by the CVD selenization of an  $\sim 0.6 \text{ nm}$  thick Pt film. Figure 4.2 b shows the Raman spectroscopy characteristic peaks from the corresponding sample, exhibiting two dominant peaks of  $E_g$  at  $\sim 175 \text{ cm}^{-1}$  and  $A_{1g}$  at  $\sim 205 \text{ cm}^{-1}$ , corresponding to the in-plane and out-of-plane vibration modes of 2D PtSe<sub>2</sub> layers, respectively.[44]

Figure 4.2 c–f exhibits the TEM characterization of the corresponding sample, identifying the general structural and chemical integrity of CVD-grown 2D PtSe<sub>2</sub> layers. Figure 4.2 c shows a

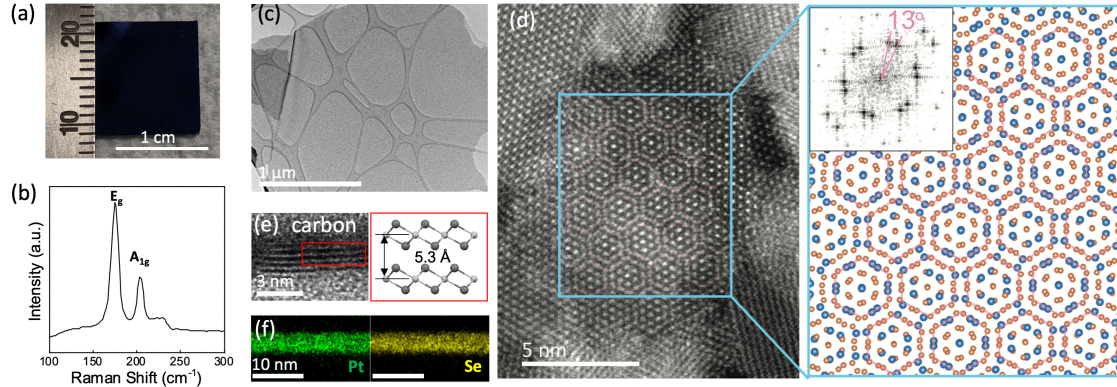


Figure 4.2: Structural and chemical characterization of as-grown 2D PtSe<sub>2</sub> layers. (a) Image of large-area 2D PtSe<sub>2</sub> layers grown on a SiO<sub>2</sub>/Si substrate. (b) Raman spectroscopy profile from the corresponding sample. (c) Low-magnification plane-view TEM image. (d) Corresponding HR-STEM image revealing Moiré fringe patterns (blue box) and their corresponding atomic structure simulation (right). The inset shows the FFT image corresponding to the blue box, depicting a misalignment angle of 13°. (e) Cross-sectional HR-TEM image (left) revealing horizontally aligned 2D PtSe<sub>2</sub> multilayers and their corresponding atomic structure model (right). (f) STEM-EDS elemental mapping images corresponding to (e), confirming the homogeneous spatial distribution of Pt and Se. Adapted with permission from reference [9]

plane-view TEM image of the sample at a low magnification, confirming the spatially continuous and homogenous film morphology. Figure 4.2 d shows the corresponding high-resolution scanning TEM (HR-STEM) image and its analysis, revealing the detailed atomic-scale structure of the CVD 2D PtSe<sub>2</sub> layers. The left HR-STEM image reveals their intrinsic polycrystallinity contributed by multiple crystalline grains of various crystallographic orientations, i.e., a mixture of crystal lattice fringes resulting from (001) zone axis-oriented hexagonal 2D PtSe<sub>2</sub> along with Moiré fringe patterns (blue box) from misaligned crystalline domains, a decisive signature of vertical stacking of horizontally aligned 2D basal planes. The blue-boxed image presented in the right panel was obtained from an atomic simulation of horizontally stacked 2D PtSe<sub>2</sub> layers with a misorientation angle of 13°, which precisely matches the Moiré fringe patterns in the HR-STEM image. The fast Fourier transform (FFT) corresponding to the HR-STEM image presented as the inset further

confirms the misorientation angle of  $13^\circ$ .

Figure 4.2 e presents a cross-sectional TEM image of the corresponding sample, revealing horizontally aligned 2D PtSe<sub>2</sub> layers with uniformly resolved van der Waals (vdW) gaps. The interlayer spacing of  $\sim 5.3$  Å (Pt-to-Pt distance) is identified, which matches the (001) planar distance of the hexagonal 2D PtSe<sub>2</sub> crystal illustrated in the atomic structure model in the right panel. Figure 4.2 f reveals the STEM-EDS elemental map images corresponding to Figure 4.2 e, unveiling the highly uniform distribution of constituting Pt and Se atoms.

### *Electrical Characterization After Plasma Treatment*

Having confirmed the chemical and structural homogeneity of horizontally aligned 2D PtSe<sub>2</sub> multilayers (layer number:  $\sim 4$ –5 in Figure 4.2 e), we then characterized their electron transport properties via FET measurements. Layer-number-dependent semiconducting-to-metallic transitions in 2D PtSe<sub>2</sub> layers have been previously verified, e.g., a transition at 2D PtSe<sub>2</sub> of four to five layers,[3, 79, 80] while the exact layer numbers for such transitions vary in the literature,[36, 41, 73, 81–83] which must be attributed to multiple variables associated with sample preparations. Two-dimensional (2D) PtSe<sub>2</sub> layer-based FET devices were fabricated by depositing gold (Au) electrodes through a shadow mask onto the 2D PtSe<sub>2</sub> layers, which contain both pristine and Ar-plasma-treated areas, as prepared in Figure 4.1. Figure 4.3 a illustrates a back-gated FET device with 2D PtSe<sub>2</sub> layers integrated on a fresh SiO<sub>2</sub>/Si wafer, and Figure 4.3 b shows an optical microscopy image of a representative device with an array of Au top electrodes. Figure 4.3 c presents an optical microscopy image of 2D PtSe<sub>2</sub> layers with both Ar-plasma-treated vs untreated areas, revealing a slightly distinct optical contrast.

Figure 4.3 d,e exhibit the FET transfer characteristics of untreated and treated 2D PtSe<sub>2</sub> layers, respectively. Drain–source current ( $I_{ds}$ ) vs drain–source voltage ( $V_{ds}$ ) plots were obtained with

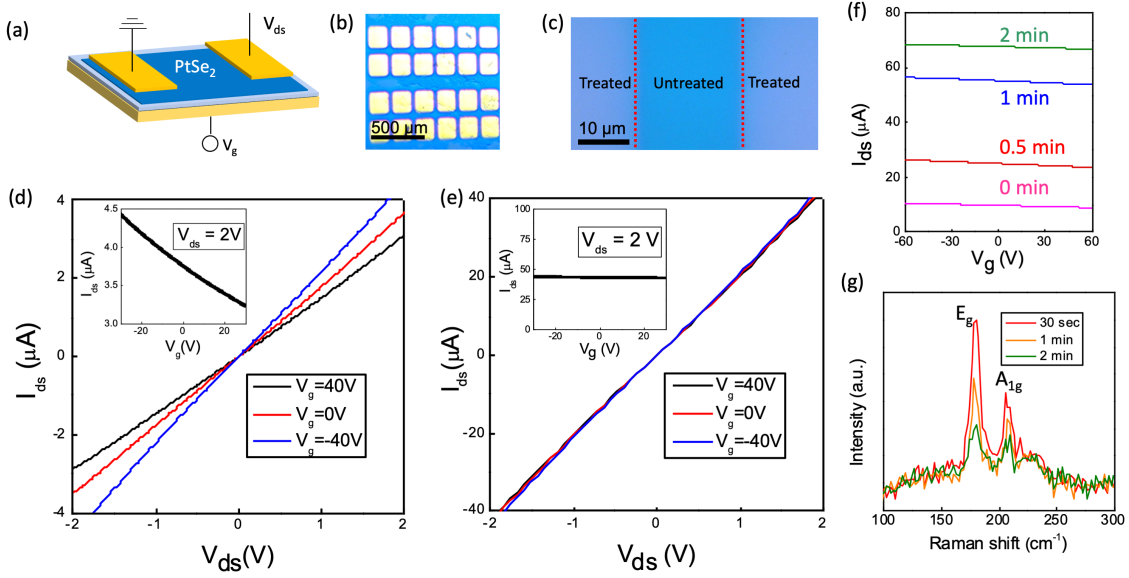


Figure 4.3: Electrical and Raman characterization of 2D PtSe<sub>2</sub> layers in their pristine and Ar-plasma-treated states. (a) Schematic of a 2D PtSe<sub>2</sub> layer-based FET device with Au electrodes in a back-gate configuration. (b) Optical microscopy image of a representative FET device. (c) Optical microscopy image unveiling color contrast between plasma-treated and -untreated regions within identical 2D PtSe<sub>2</sub> layers. (d)  $I_{ds}$ - $V_{ds}$  FET transfer plots from pristine 2D PtSe<sub>2</sub> layers, confirming p-type semiconducting characteristics. The inset shows the corresponding  $I_{ds}$ - $V_g$  transfer characteristics. (e)  $I_{ds}$ - $V_{ds}$  FET transfer plots from plasma-irradiated 2D PtSe<sub>2</sub> layers, confirming metallic characteristics with almost zero-gate modulation. The inset shows the corresponding  $I_{ds}$ - $V_g$  transfer characteristics. (f)  $I_{ds}$ - $V_{ds}$  characteristics from another FET device with thicker 2D PtSe<sub>2</sub> layers systematically irradiated with Ar-plasma for varying durations. The drain voltage was set at 1 V. (g) Raman spectroscopy profiles obtained from the sample corresponding to (f) with varying plasma irradiation times. Adapted with permission from reference [9]

varying amplitudes of back-gate voltage ( $V_g$ ) for both. In Figure 4.3 d, the pristine (i.e., untreated) 2D PtSe<sub>2</sub> layers display p-type semiconducting characteristics manifested by the decrease of  $I_{ds}$  with increasing  $V_g$  from  $-40$  to  $40$  V, consistent with the  $I_{ds}$ - $V_g$  transfer plot in the inset. The result is in good agreement with the previous FET study with CVD 2D PtSe<sub>2</sub> layers of comparable thickness.[44, 84] On the other hand, the 2D PtSe<sub>2</sub> layers treated with Ar plasma (duration time: 2 min in this case) display very distinct characteristics as presented in Figure 4.3 e, i.e., the nearly complete overlap of  $I_{ds}$ - $V_{ds}$  plots irrespective of  $V_g$  with increasing conductance, a signature of

metallic transport. The corresponding  $I_{ds}-V_g$  plot presented in the inset is also distinct from that in Figure 4.3 d. This metallic behavior is quite interesting and unexpected, given that 2D PtSe<sub>2</sub> layers of such a small thickness ( $\sim 3$  nm as shown in Figure 4.2 e) should belong to the semiconducting regime, as theoretically predicted and experimentally verified.[36, 83]

We also prepared 2D PtSe<sub>2</sub> layers by selenizing Pt films of a slightly larger thickness ( $\sim 0.75$  nm compared to  $\sim 0.6$  nm in Figure 4.3 a–e) and systematically identified their FET characteristics before/after the Ar-plasma treatment. Figure 4.3 f presents  $I_{ds}-V_g$  transfer plots of the corresponding 2D PtSe<sub>2</sub> layers, revealing a systematic increase of  $I_{ds}$  with prolonged plasma treatment, which further confirms pronounced metallic properties. As mentioned in Figure 4.1, we have observed that the direct Ar-plasma irradiation onto fabricated PtSe<sub>2</sub>/SiO<sub>2</sub>/Si FET devices leads to significantly increased leakage current in them. This indicates that the charge density state of underlying SiO<sub>2</sub> might have been significantly alternated by the plasma irradiation, leading to unstable (generally high)  $I_{ds}$  even when  $V_g = 0$  V.

Figure 4.3 g shows the Raman spectroscopy characterization of the identical 2D PtSe<sub>2</sub> layers prepared with varying Ar-plasma treatment times. While their relative peak intensity is observed to decrease systematically, it is evident that 2D PtSe<sub>2</sub> layers still well retain characteristic  $E_g$  and  $A_{1g}$  peaks even up to 2 min Ar-plasma treatment. A slight ( $\sim 32\%$ ) broadening of the  $E_g$  peak is noticed after the plasma treatment, which indicates a localized breaking of the crystal symmetry in 2D PtSe<sub>2</sub> layers, as previously reported.[85] Moreover, the plasma-induced decrease of both  $E_g$  and  $A_{1g}$  peak intensities is mainly attributed to the loss of Se atoms, to be verified in the next section. Additionally, we performed atomic force microscopy (AFM) characterization and confirmed that this mild Ar-plasma treatment does not significantly alter the overall thickness of 2D PtSe<sub>2</sub> layers.

### Temperature-Variant Electrical Characterization After Plasma Treatment

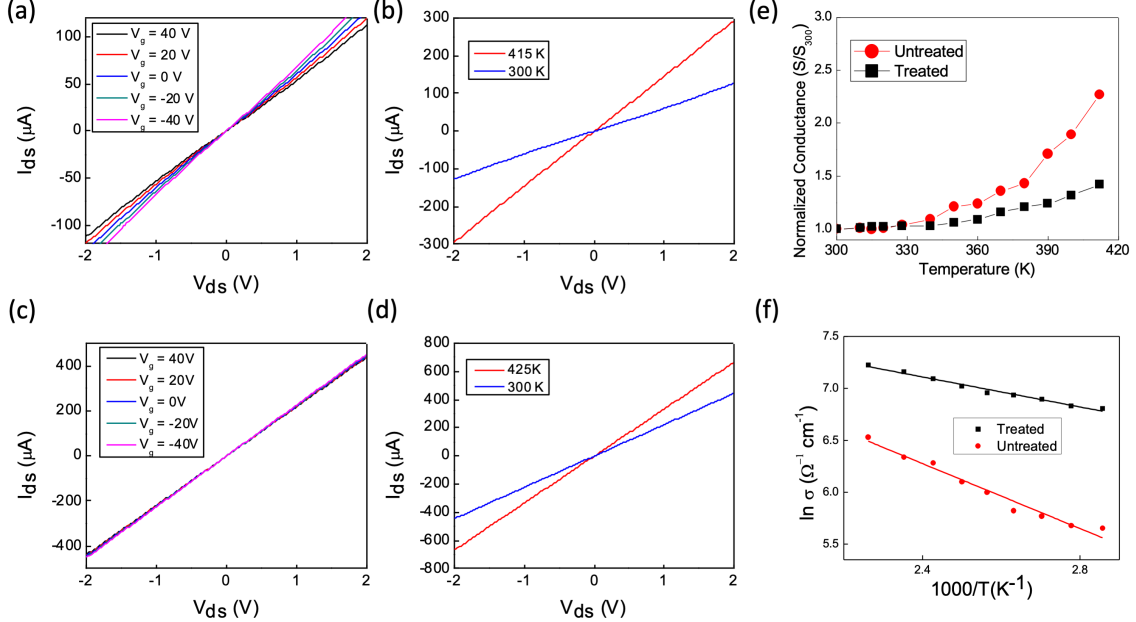


Figure 4.4: Temperature-variant FET transport characteristics of 2D PtSe<sub>2</sub> layers in pristine vs Ar-plasma-irradiated states. Pristine 2D PtSe<sub>2</sub> layers revealing (a)  $V_g$ -dependent  $I_{ds}$ - $V_{ds}$  transfer curves at 300 K and (b)  $I_{ds}$ - $V_{ds}$  characteristics under  $V_g = 0$  V obtained at 300 and 412 K. Ar-treated 2D PtSe<sub>2</sub> layers revealing (c)  $V_g$ -dependent  $I_{ds}$ - $V_{ds}$  transfer curves at 300 K and (d)  $I_{ds}$ - $V_{ds}$  characteristics under  $V_g = 0$  V obtained at 300 and 412 K. (e) Comparison of the current ratio with respect to 300 K as a function of temperature for the corresponding pristine and Ar-treated samples. (f) Comparison of activation energies for thermally driven transports of charge carriers in pristine vs Ar-plasma-treated 2D PtSe<sub>2</sub> layers. Adapted with permission from reference [9].

Temperature-variant FET measurements were performed with both pristine and Ar-treated 2D PtSe<sub>2</sub> layers to gain insights toward better understanding the plasma-driven conversion of semiconducting-to-metallic transports. Figure 4.4 a shows representative  $I_{ds}$ - $V_{ds}$  FET transfer curves from a sample of pristine 2D PtSe<sub>2</sub> layers with varying  $V_g$  at 300 K. A clear gate modulation is observed, indicating its intrinsic semiconducting transport. Figure 4.4 b presents  $I_{ds}$ - $V_{ds}$  FET transfer curves from the same sample under a fixed zero-gate bias (i.e.,  $V_g = 0$  V) at two different temperatures of 300 and 412 K. A significant ( $\sim 2.3$  times) increase of  $I_{ds}$  is observed with increasing tem-

perature by 112 K, which is a typical characteristic of temperature-dependent carrier transports in semiconducting crystals. Figure 4.4c shows  $I_{ds}$ - $V_{ds}$  FET transfer curves from the identical 2D PtSe<sub>2</sub> layers after Ar-plasma exposure with varying  $V_g$  at 300 K. Unlike the obvious p-type gate response observed in Figure 4.4b, the Ar-plasma-exposed sample shows significantly suppressed  $V_g$  dependency with increased electrical conductance, similar to that in Figure 4.4 e. Upon increasing temperature from 300 to 412 K, the sample also exhibits increased  $I_{ds}$ , as shown in Figure 4.4 d. However, the degree of this current increase is much smaller than that observed with the initially semiconducting pristine sample (Figure 4.4 b). Plots of temperature-dependent electrical conductance ratio values with respect to that at 300 K, i.e.,  $S/S_{300}$ , are presented for both pristine and Ar-plasma-treated samples in Figure 4.4 e. The pristine sample exhibits a much stronger temperature-dependent conductance increase, reflecting its intrinsic semiconducting nature and thermal generation of charge carriers, consistent with the temperature dependency observed with 2D MoS<sub>2</sub> layers.[86]

Moreover, the Ar-plasma-exposed sample exhibits a much weaker temperature dependency of electrical conductance with a smaller increase of  $S/S_{300}$ , i.e.,  $\sim 1.3$  compared to  $\sim 2.3$  for the pristine sample at 412 K. Although this slight increase of temperature-dependent conductance deviates from the standard behavior of typical metallic materials, this observation is fully consistent with recent studies on the temperature dependency of “metallic” 2D WSe<sub>2</sub> layers converted from their initial semiconducting phases.[78] This phenomenon must be attributed to the “incomplete” closing of the band-gap energy of 2D PtSe<sub>2</sub> layers and its associated hopping-dominated transports.[78, 86] Moreover, thermal activation energy ( $E_a$ ) values for majority carrier transports were calculated at a given temperature,  $T$ , using the Arrhenius equation, i.e.,  $\sigma(T) = \sigma_0 e^{\frac{-E_a}{kT}}$ , where  $\sigma_0$  is the electrical conductivity at  $T = 0$  K and  $k$  is Boltzmann’s constant. Figure 4.4 f displays the Arrhenius plots for both cases, revealing the linear relationship of  $\ln\sigma$  vs  $\frac{1000}{T}$ , where  $E_a$  values can be extracted from the slopes of the linear fittings. The activation energies of pristine and Ar-

treated 2D PtSe<sub>2</sub> layers are 134.43 and 62.04 meV, respectively. The reduced  $E_a$  value indicates relaxed band-to-band transports in semiconducting 2D PtSe<sub>2</sub> layers after the plasma treatment, further suggesting a reduction of their band-gap energy, to be verified in the next section.

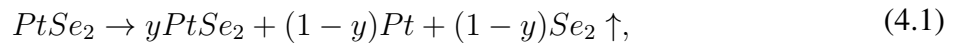
### *Chemical and Structural Characterization Before and After Plasma Treatment*

To better clarify the mechanism for the Ar-plasma-induced semiconducting-to-metallic conversion, we performed extensive structural and chemical characterization of 2D PtSe<sub>2</sub> layers before/after the Ar-plasma treatment. Figure 4.5 a,b presents the XPS characterization of 2D PtSe<sub>2</sub> layers, comparing their core-level spectra of Pt 4f (Figure 4.5a) and Se 3d (Figure 4.5b) in pristine vs plasma-treated states. In Figure 4.5 a, the red plot obtained from 2D PtSe<sub>2</sub> layers in their pristine state predominantly exhibits the characteristics peaks of Pt<sup>4+</sup> oxidation states, indicating stoichiometric PtSe<sub>2</sub>, fully consistent with previous studies.[44] Meanwhile, the blue plot obtained from the identical 2D PtSe<sub>2</sub> layers after the Ar-plasma treatment exhibits additional peaks that correspond to Pt<sup>0</sup> oxidation states.[87] XPS peak deconvolution analysis identifies the areal ratio of Pt<sup>4+</sup>/Pt<sup>0</sup> to be 53:47, which leads to the Pt/Se atomic ratio of  $\sim 1:1.1$ . The core-level spectra of Se 3d in Figure 4.5 b also exhibit characteristic peaks corresponding to stoichiometric PtSe<sub>2</sub>, consistent with previous studies.[44] This XPS analysis suggests that the Ar-plasma treatment leads to the formation of elemental Pt atoms, i.e., increasing amount of Pt<sup>0</sup> oxidation states without causing a noticeable change in the oxidation state of Se atoms. The peak intensity decrease observed in Figure 4.5 b indicates a pronounced loss of Se atoms, further to be verified by EDS characterization.

Moreover, extensive TEM characterization was performed to unveil a possibility for the formation of any new crystalline phases within 2D PtSe<sub>2</sub> layers induced by the Ar plasma. Figure 4.5 c,d presents low-magnification TEM images of 2D PtSe<sub>2</sub> layers (left) and their corresponding se-

lected area electron diffraction (SAED) patterns (right) before and after the Ar-plasma treatment, respectively. The TEM and SAED characterization confirms no formation of additional crystalline phases, except for hexagonal PtSe<sub>2</sub> crystals. Moreover, the dominant appearance of (110) and (100) SAED ring patterns for both samples indicates that individual 2D PtSe<sub>2</sub> layers are horizontally aligned, which is well preserved irrespective of the Ar-plasma treatment, consistent with the previous studies.[73] Figure 4.5 e shows EDS profiles obtained from the 2D PtSe<sub>2</sub> layers before/after Ar treatment, corresponding to the TEM images in Figure 4.5 c,d. Pristine 2D PtSe<sub>2</sub> layers exhibit a stoichiometric atomic ratio of Pt/Se  $\sim$  1:2 as anticipated, consistent with the XPS characterization. However, it is interesting to note that the Ar-plasma treatment leads to a Pt-rich compositional change of Pt/Se  $\sim$  1:x, where  $x = 1.1\text{--}1.25$ , even though there is no signature of new crystalline phase formation or significant structural transformation (SAED in Figure 4.5d). This combined analysis of XPS, plane-view TEM/SAED, and EDS indicates that 2D PtSe<sub>2</sub> layers turn into Pt-rich due to a loss of Se atoms by the Ar-plasma treatment while well retaining their original crystalline integrity.

This pronounced loss of Se over Pt caused by external Ar-plasma energy is consistent with the recent observation of significant S loss in 2D MoS<sub>2</sub> layers under in situ heating.[88] This phenomenon is attributed to the intrinsically higher volatility of chalcogen components over transition metals, owing to their lower cohesive energies.[89] The chemical conversion takes place according to the following reaction



$$\text{where, } 0.524 \leq y \leq 0.556$$

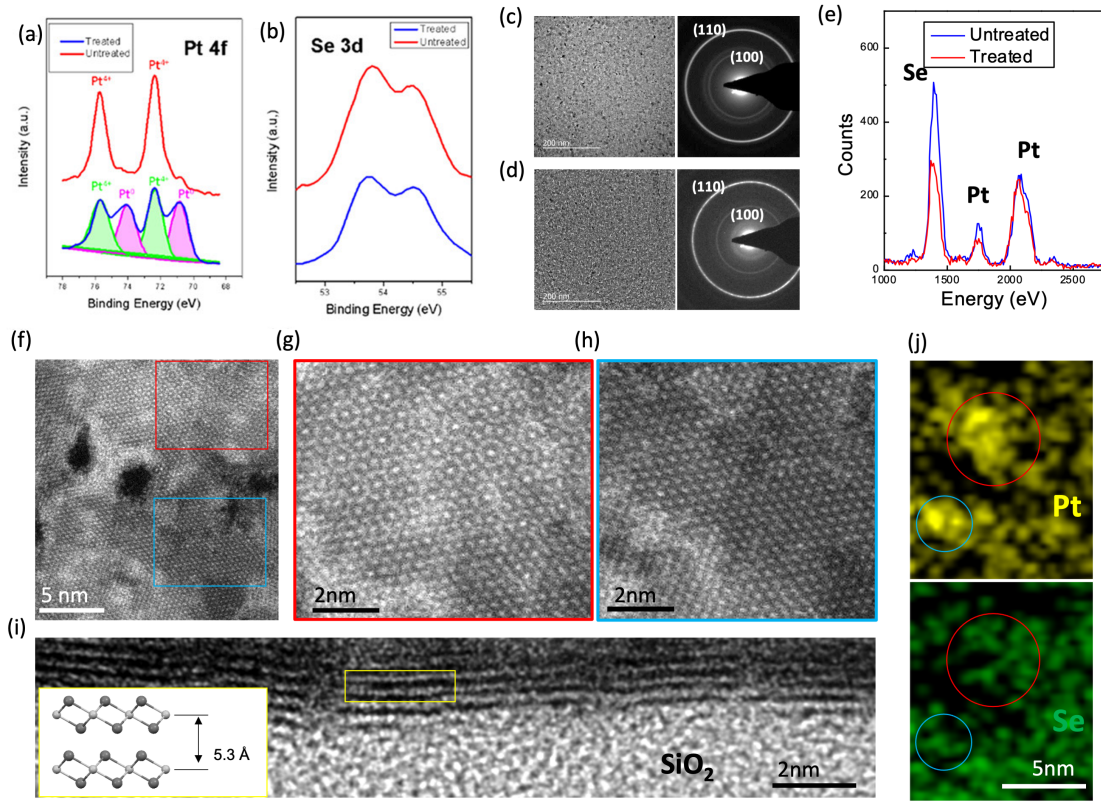


Figure 4.5: Structural and chemical characterization of 2D PtSe<sub>2</sub> layers before/after the Ar-plasma treatment. XPS spectra of (a) Pt 4f and (b) Se 3d core levels obtained from 2D PtSe<sub>2</sub> layers in pristine vs Ar-plasma-treated states. Low-magnification TEM images (left) and corresponding SAED patterns (right) from 2D PtSe<sub>2</sub> layers in (c) untreated and (d) treated states. (e) EDS spectra obtained from 2D PtSe<sub>2</sub> layers in Ar-plasma-treated and -untreated states. (f) HR-STEM image of Ar-plasma-irradiated 2D PtSe<sub>2</sub> layers. Zoom-in images corresponding to the (g) red and (h) blue boxes in (f). (i) Cross-sectional HRTEM image of Ar-plasma-irradiated 2D PtSe<sub>2</sub> layers. (j) EDS elemental map images visualizing a localized distribution of Pt and deficiency of Se. Adapted with permission from reference [9].

Detailed crystalline structures of Ar-plasma-treated 2D PtSe<sub>2</sub> layers were characterized by HR-STEM, which was performed for the sample corresponding to the low-magnification TEM in Figure 4.5 d. The HR-STEM image in Figure 4.5 f clarifies the structural distinction of 2D PtSe<sub>2</sub> layers after the Ar-plasma treatment, revealing that tiny atomic vacancy-like areas (typically  $\sim 1$ -3

nm) are “sparsely” observed throughout the entire sample area. The red and blue box regions in Figure 4.5 f are zoomed-in and presented in Figure 4.5 g,h, respectively. Interestingly, we note that Ar-plasma-treated 2D PtSe<sub>2</sub> layers still well preserve their high polycrystallinity, as evidenced by the clearly observed crystalline lattice fringes, particularly the Moiré fringe patterns in Figure 4.5 g.

We further carried out cross-section TEM characterization of the Ar-plasma-treated 2D PtSe<sub>2</sub> layers, and the corresponding cross-sectional TEM image is presented in Figure 4.5 i. We observe that the horizontal alignment of 2D PtSe<sub>2</sub> layers is well preserved even after the plasma treatment accompanying the original vdW interlayer spacing of  $\sim 5.3$  Å (the inset corresponding to the yellow box) without any discontinuity of individual layers and significant thickness change. We also performed STEM-EDS elemental mapping on the Ar-plasma-treated 2D PtSe<sub>2</sub> layers to identify the spatial distribution of constituting Pt and Se atoms. The STEM-EDS elemental map images in figure 4.5 j reveal a relatively higher intensity of Pt over Se at multiple locations (red and blue circles), which was consistently observed throughout the entire sample area.

This very comprehensive structural and chemical analysis suggests that the following events must have occurred by being responsible for the electrically observed semiconducting-to-metallic transition in 2D PtSe<sub>2</sub> layers; the mild Ar-plasma treatment employed in this study neither significantly alters the original crystallinity and thickness of 2D PtSe<sub>2</sub> layers nor introduces any new crystalline phases. It mainly causes the decomposition of Se atoms, which in turn results in the “spill” of Pt elemental atoms achieving Pt-rich (Se-deficient) PtSe<sub>x</sub> layers with  $x < 2$ . Accordingly, a large concentration of “Se-deficient” atomic vacancies and layer edge sites coupled with exposed Pt nanoparticles formed within 2D basal planes will reduce the original band-gap energy of 2D PtSe<sub>2</sub> layers by forming percolated networks for efficient charge carrier transport.

## Conclusion

We irradiated wafer-scale CVD-grown few-layer 2D PtSe<sub>2</sub> samples with controlled Ar plasma and externally converted their intrinsic semiconducting properties into metallic transports, confirmed by FET measurements. By employing extensive structural and chemical characterization, we identified that the plasma-irradiated initially stoichiometric 2D PtSe<sub>2</sub> layers became Se-deficient while well preserving their overall crystallinity. This corroborative experimental and theoretical study fully accounts for the origin of the externally modulated semiconducting-to-metallic conversion in 2D PtSe<sub>2</sub> layers, suggesting their extended technological implications for near-atom-thickness electronic devices.

## **CHAPTER 5: 2D PtSe<sub>2</sub>/3D SILICON SCHOTTKY JUNCTION FOR SOLAR CELL APPLICATION**

The contents of this chapter have been published in:

M. S. Shawkat, H.-S. Chung, D. Dev, S. Das, T. Roy, and Y. Jung, “Two-Dimensional/Three-Dimensional Schottky Junction Photovoltaic Devices Realized by the Direct CVD Growth of vdW 2D PtSe<sub>2</sub> Layers on Silicon,” ACS Applied Materials Interfaces, vol. 11, no. 30, pp. 27251-27258, 2019.

### **Introduction**

Strong metallic nature of 2D PtSe<sub>2</sub> layers projects metal/semiconductor Schottky junction based on “mixed-dimensional” vdW heterostructures[65] when they are interfaced with three-dimensional (3D) semiconductors. The most well-established form of 2D/3D vdW heterostructure-based Schottky junctions can be found in graphene/semiconductor heterojunctions such as mechanically integrated graphene on top of silicon (Si). Although these graphene/Si Schottky junctions are recently gaining significant interest in a variety of electronic applications such as photovoltaic devices,[66, 67] their preparation requires the mechanical separation of high-temperature CVD-grown graphene from growth substrates (e.g., copper (Cu)) and its subsequent transfer to Si wafers.[68,69,90] Accordingly, the process stands a high chance of introducing unwanted contamination throughout the chemical/mechanical treatment of graphene for delamination and integration. As shown in previous section, we directly synthesized 2D PtSe<sub>2</sub> on 3D silicon and evaluated their material property. With this direct synthesis method, we are able to synthesize large-area Schottky junction devices

In this chapter, we evaluated the 2D PtSe<sub>2</sub>/ 3D Si Schottky Junction devices and verified a com-

prehensive set of material parameters, which define excellent Schottky junction characteristics, i.e., small ideality factor, large current rectification, and temperature-dependent variation of Schottky barrier heights. Moreover, we observed strong photovoltaic effects in these 2D PtSe<sub>2</sub>/3D Si Schottky junction devices.

## Results and Discussion

### *Temperature-Variant Electrical Characterization*

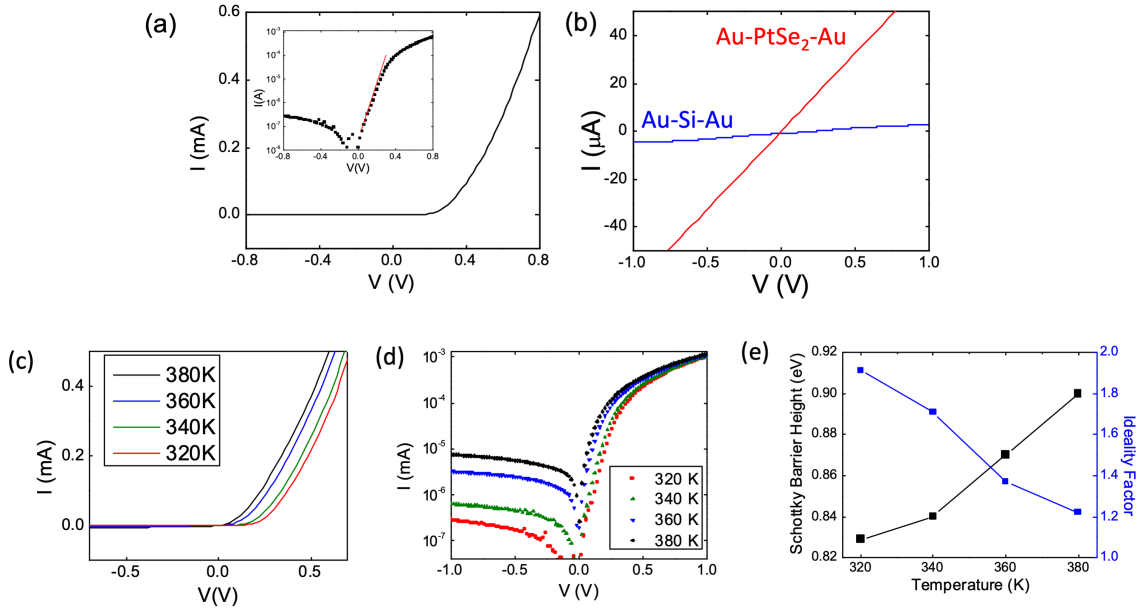


Figure 5.1: Characterization of Schottky junction characteristics in 2D PtSe<sub>2</sub>/Si devices. (a)  $I$ – $V$  characteristics of a 2D PtSe<sub>2</sub>/Si Schottky junction device. The inset presents the corresponding semilog plot. (b)  $I$ – $V$  characteristics from only-2D PtSe<sub>2</sub> layers and only-Si wafers without 2D PtSe<sub>2</sub>/Si junctions obtained with Au contacts. (c)  $I$ – $V$  characteristics with varying temperature in a range of 320–380 K. (d) Semilog plots corresponding to (c). (e) Temperature-dependent Schottky barrier height and ideality factor. Adapted with permission from reference [6].

Figure 5.1 presents the electrical characterization results of 2D PtSe<sub>2</sub>/Si Schottky junction devices.

Figure 5.1 a shows the two-terminal current–voltage (I–V) characteristics of a 2D PtSe<sub>2</sub>/Si Schottky junction device measured with Au contacts. The device exhibits asymmetric rectifying I–V characteristics with a high rectification ratio of  $> 10^3$  as manifested in the corresponding semilog plot in the inset. Moreover, from the linear tangential (red slope) to the semilog plot belonging to a forward bias regime, a diode ideality factor,  $n$ , can be extracted and it is found to be  $\sim 1.9$ . Details for the ideality factor extraction are presented in the next section. The deviation of  $n$  from unity indicates that the device performance is presently impaired by recombination of majority carriers, which is most likely attributed to unoptimized device process conditions. To confirm that the observed current rectification indeed reflects Schottky junction characteristics, we separately characterized the I–V characteristics of only-2D PtSe<sub>2</sub> layers and only-Si wafers without 2D PtSe<sub>2</sub>/Si junctions. 5.1 b reveals that both 2D PtSe<sub>2</sub> layers and Si wafers exhibit highly symmetric Ohmic transport characteristic with Au contacts, which decisively confirms that the observed rectification originates from the 2D PtSe<sub>2</sub>/Si junction.

To better understand the underlying transport mechanism of 2D PtSe<sub>2</sub>/Si Schottky junction devices, we employed temperature-variant I–V measurements. 5.1 c presents the variation of I–V characteristics under varying temperature, revealing an increase of current in the forward bias regime with increasing temperature. 5.1 d shows the semilog plots of the corresponding I–V characteristics with varying temperature. In addition to the increase of current in the forward bias regime, it is observed that there is a significant increase ( $> 50$  times) of current in the reverse bias regime as temperature increases from 320 to 380 K. Such a temperature-dependent increase of current indicates the thermal excitation of electrons within semiconducting Si, reflecting an increase of carrier concentration in its conduction band.[91, 92] From these temperature-dependent I–V plots, we further extract important material parameters, which define the performances of the Schottky junction devices; i.e., Schottky barrier height,  $\Phi_B$ , and ideality factor,  $n$ . According to thermionic emission theory,[93] the current,  $I$ , through a Schottky diode is expressed as

$$I = I_0 e^{\frac{q(V-IR_s)}{nkT}} \quad (5.1)$$

Here,  $I_0$  is the reverse saturation current, which can be modeled as

$$I_0 = AA^{**}T^2 e^{\frac{-q\Phi_B}{kT}} \quad (5.2)$$

Here,  $q$  is the charge of an electron,  $A^{**}$  is the Richardson constant for Si,  $A$  is the active diode surface area,  $T$  is the absolute temperature,  $k$  is the Boltzmann constant,  $R_s$  is the series resistance, and  $V$  is the voltage applied across the diode. Moreover, the diode equation can be re-expressed as[94].

$$\frac{dV}{d\ln J} = IR_s + n \frac{kT}{q} \quad (5.3)$$

where  $J = I/A$ , Then

$$IR_s + n\Phi_B = V - n \frac{kT}{q} \ln \frac{I}{AA^{**}T^2} \quad (5.4)$$

Figure 5.1e presents the variation of  $\Phi_B$  and  $n$  as a function of temperature extracted from the above equation, revealing that  $\Phi_B$  increases with increasing temperature. The observation is consistent with previous studies on similarly structured 2D/3D Schottky junction devices such as graphene/Si,[95] indicating that current density is dominated by thermal excitation rather than  $\Phi_B$ . Meanwhile,  $n$  decreases with increasing temperature, indicating diminished carrier recombination possibly due to the thermal annihilation of structural defects at 2D PtSe<sub>2</sub>/Si interfaces. Moreover, the room-temperature series resistance was determined to be  $\sim 529 \Omega$  extracted from equation 5.4, which is consistent with previous studies.[70, 96]

## Photovoltaic Characterization

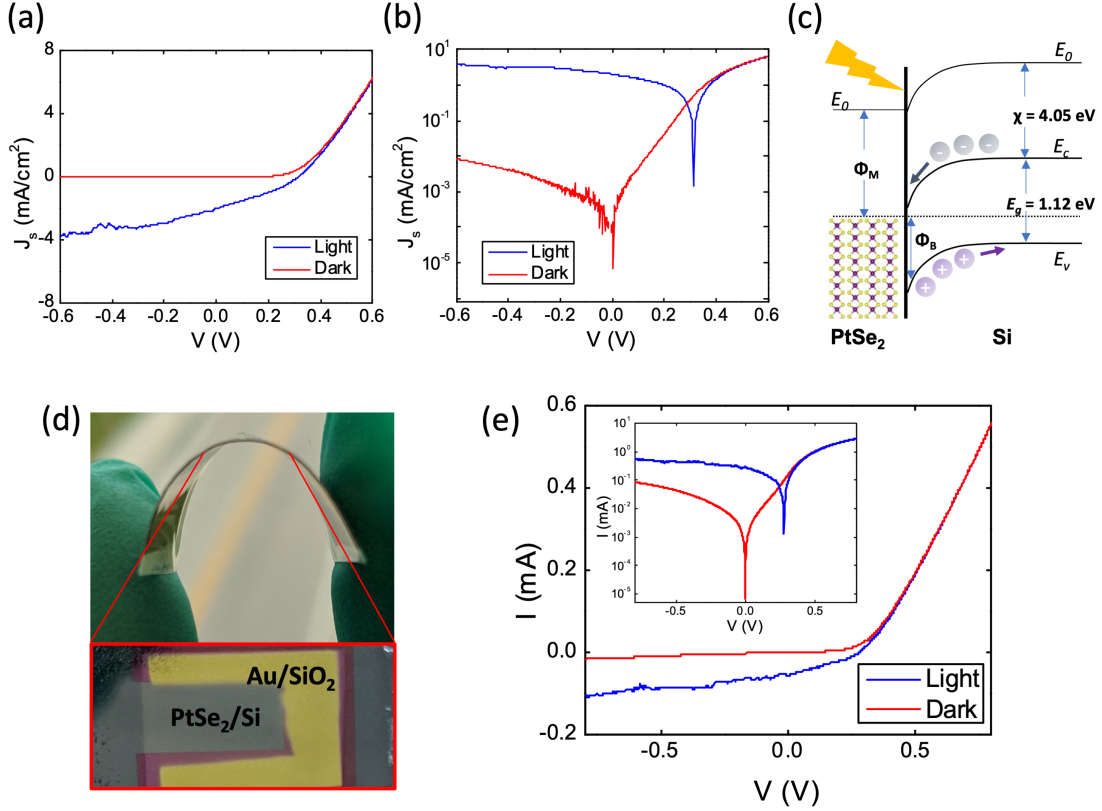


Figure 5.2: Photovoltaic characteristics of 2D PtSe<sub>2</sub>/Si devices. (a, b) J–V characteristics of a 2D PtSe<sub>2</sub>/Si Schottky junction device in dark (red) and under illumination (blue) in (a) linear and (b) semilog scales. (c) Representative band diagram of a 2D PtSe<sub>2</sub>/Si Schottky junction under zero bias. (d) Photo image of a flexible 2D PtSe<sub>2</sub>/Si Schottky junction device. (e) I–V characteristics of the device in (d) in dark (red) and under illumination (blue). The inset presents the corresponding characteristics on a semilog scale. Adapted with permission from reference [6].

We investigated the photovoltaic properties of 2D PtSe<sub>2</sub>/Si Schottky junction devices by measuring their photoresponsiveness. Figure 5.2 a demonstrates the current density–voltage (J–V) characteristics of a 2D PtSe<sub>2</sub>/Si junction device in dark (red) and under illumination (blue). Upon illumination with a  $400 \text{ W/m}^2$  illumination source, the device exhibits a significant photovoltaic effect as manifested by a generation of reverse current density. Figure 5.2 b shows the semilog plot

of the corresponding J–V characteristics better demonstrating photovoltaic device parameters, i.e., open-circuit voltage  $V_{oc}$  and short-circuit current density  $J_{sc}$ . By analyzing both Figure 5.2 a,b, we extract  $V_{oc} \sim 0.35$  V, fill factor (FF) of  $\sim 26\%$ , and  $J_{sc} \sim 4$  mA/cm<sup>2</sup>, which leads to a power conversion efficiency (PCE) of  $\sim 1\%$ . Figure 5.2 c describes a diagram of the energy band bending formed at the 2D PtSe<sub>2</sub>/Si Schottky junction, which justifies that the generation of photoexcited carriers is responsible for the observed photovoltaic effect under zero bias. The band-bending diagram is constructed based on the room-temperature  $\Phi_B$ , and the electron affinity ( $\chi$ ) and band gap ( $E_g$ ) of Si known from the literature.[97]  $E_c$  and  $E_v$  are the conduction band edge and the valence band edge of Si, respectively. We note that the operational principle of 2D PtSe<sub>2</sub>/Si Schottky junction photovoltaics is, in principle, similar to those of other metallic 2D layers/Si-based systems.

The most extensively studied one is graphene/Si heterojunction devices whose initial PCE were  $\sim 1.5\%$  in 2010,[69] comparable to that of 2D PtSe<sub>2</sub>/Si. Since then, significant efforts have been made to further improve the PCE of graphene/Si devices by engineering their intrinsic electronic/physical structures; these efforts include adjusting band offsets and heterojunction interfaces, as well as incorporating light-trapping structures.[98] P-type doping of graphene can increase FF by reducing its sheet resistance, as well as increasing its work function (thus, Schottky barrier), as previously reported.[99, 100] Additionally, light-trapping materials and passivation layers have been incorporated to reduce light reflection from Si surface, as well as to improve graphene/Si interfacial morphology, respectively.[101, 102] The highest PCE of graphene/Si Schottky junction photovoltaics is now up to 16.2%,[103] reflecting a drastic improvement over the last several years. Considering the similarity of their operational principle, we project that the photovoltaic performances of 2D PtSe<sub>2</sub>/Si Schottky junction devices can also be significantly improved by employing those engineering schemes developed for graphene/Si systems.

The fabrication of photovoltaic Schottky junctions via a direct growth of metallic 2D PtSe<sub>2</sub> layers

on Si can be further extended to realize 2D PtSe<sub>2</sub>/Si flexible photovoltaic devices. 2D PtSe<sub>2</sub> layers were directly grown on thin Si wafers (thickness < 50 μm), which were prepared by potassium hydroxide (KOH) etch followed by the device fabrication procedure described in Figure 3.1 a. Figure 5.2 d shows a camera image of a 2D PtSe<sub>2</sub>/Si flexible device under mechanical bending, as well as its device components described in the inset. Figure 5.2 e presents the I–V characteristics of the same device without bending in dark (red) and under illumination (blue), as well as the corresponding semilog plot in the inset. The device exhibits a significant photovoltaic effect with  $V_{oc} \sim 0.28$  V,  $I_{sc} \sim 0.282$  mA/cm<sup>2</sup>, and FF  $\sim 28.75\%$ .

### *Opto-Mechanical Properties*

We further evaluated the photovoltaic performances of 2D PtSe<sub>2</sub>/Si photovoltaic devices under mechanical deformation. A flexible 2D PtSe<sub>2</sub>/Si photovoltaic device was tested under a systematic application of controlled bending; it first underwent 100 bending cycles at a bending radius of R1 = 9.43 mm and subsequently underwent another 100 bending cycles at a bending radius of R2 = 5.95 mm (Figure 5.3 a–f). Characteristics of current density vs. voltage (J–V) were obtained after 0th, 10th, and 100th bending cycles at each radius. Figure 5.3 a shows an image of the device at a bending radius, R1. Figure 5.3 b, c represents J–V curves obtained before and after the first 100 bending cycles at R1, respectively, revealing good retention of significant photovoltaic effects. Figure 5.3 d shows an image of the same device at a bending radius, R2, after the bending shown in Figure 5.3 b,c. Figure 5.3 e, f represents J–V curves obtained before and after the first 100 bending cycles at R2, respectively. We extract  $J_{sc}$  and  $V_{oc}$  for each bending radius and present them as a function of bending cycles in Figure 5.3 g, h, respectively. We note that  $V_{oc}$  remains nearly constant, while  $J_{sc}$  slightly decreases with increasing bending cycles possibly due to a pronounced generation of charge recombination sites within 2D PtSe<sub>2</sub> layers. The measurements were carried out under an AM 1.5 solar spectral irradiance with an intensity of 245 W/m<sup>2</sup>.

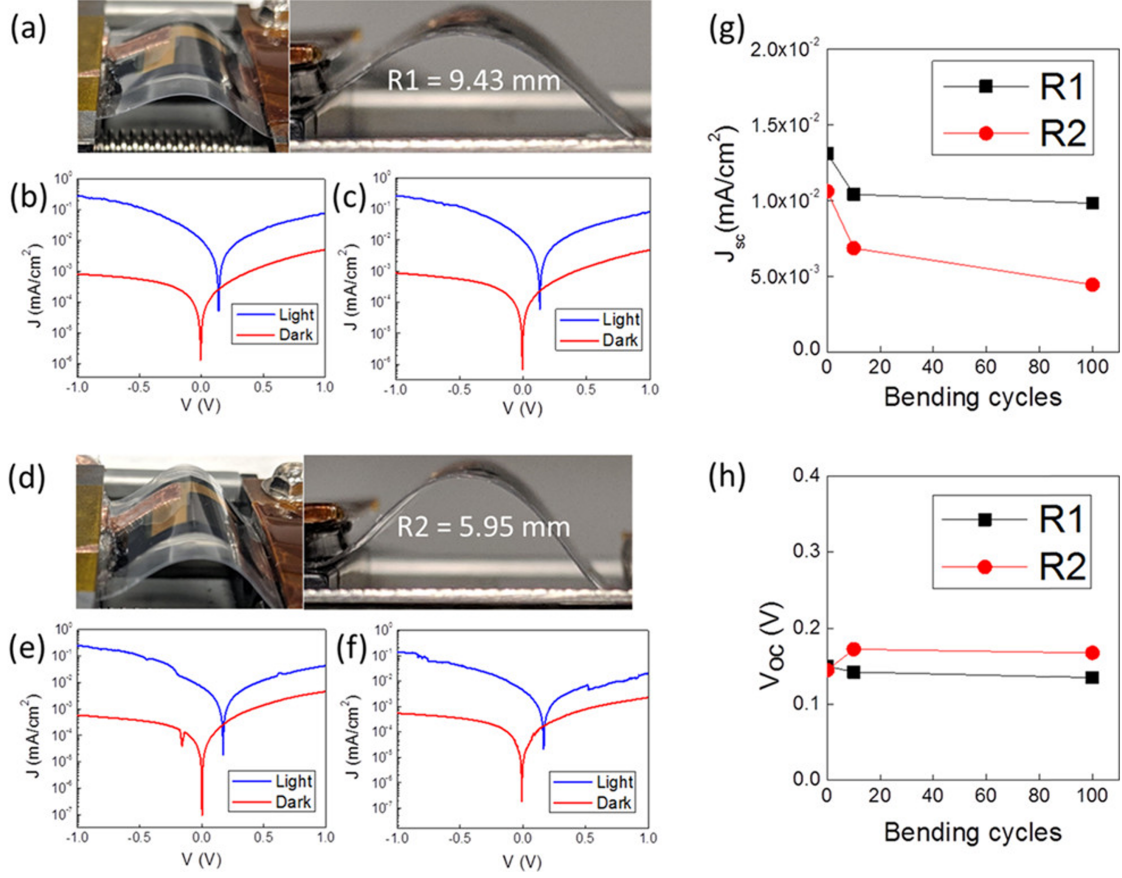


Figure 5.3: Flexible photovoltaic 2D PtSe<sub>2</sub>/Si devices. (a–c) Photovoltaic responses before/after repeated bending at a bending radius of  $R_1 = 9.43$  mm. (a) Corresponding image. (b) Photovoltaic characteristics before bending. (c) Photovoltaic characteristics after 100 times bending at  $R_1$ . (d–f) Photovoltaic responses before/after repeated bending at a bending radius of  $R_2 = 5.95$  mm. (d) Corresponding image. (e) Photovoltaic characteristics before bending. (f) Photovoltaic characteristics after 100 times bending at  $R_2$ . (g)  $J_{sc}$  with varying bending cycles. (h)  $V_{oc}$  with varying bending cycles. Adapted with permission from reference [6].

## Conclusion

In summary, we have directly grown 2D PtSe<sub>2</sub> layers of controlled morphological orientation and carrier transport on Si wafers and fabricated 2D PtSe<sub>2</sub>/Si heterojunction devices. With vertically aligned 2D PtSe<sub>2</sub> layers of metallic transports interfaced with Si, we have identified pronounced

Schottky junction characteristics such as high-current rectification ratio, temperature-dependent barrier height, and diode ideality factors. Such intrinsic Schottky junction characteristics lead to significant photovoltaic effects upon light illumination, suggesting a technological versatility and promise of these 2D/3D electronic junctions.

## CHAPTER 6: 2D $\text{PtTe}_2$ /3D SILICON SCHOTTKY JUNCTION FOR VISIBLE LIGHT PHOTODETECTION

The contents of this chapter have been published in:

M. S. Shawkat, T. A. Chowdhury, H.-S. Chung, S. Sattar, T.-J. Ko, J. A. Larsson, and Y. Jung, “Large-area 2D  $\text{PtTe}_2$ /Silicon Vertical-Junction Devices with Ultrafast and High-sensitivity Photodetection and Photovoltaic Enhancement by Integrating Water Droplets,” *Nanoscale*, vol. 12, no. 45, pp. 23116-23124, 2020.

### Introduction

Although a large number of semiconducting 2D TMD layers have been explored for unconventional opto-electronics,[104,105] their carrier mobility values still remain uncompetitive with those of traditional semiconductors.[24,29] In this regard, noble metal (particularly, platinum (Pt))-based ones provide distinguishable advantages of high carrier mobility[6,9,36,42,60,106] and air stability even better than black phosphorus (BP) as well as low-temperature synthesis.[41,107] 2D platinum ditelluride ( $\text{PtTe}_2$ ) layers are a recent addition to them and exhibit a large set of unparalleled properties compared to other Pt-based 2D TMD layers.[57,108,109] Most notably, they exhibit an extremely high electrical conductivity of  $> 10^6 \text{ S/m}$  – superior to most of the previously reported 2D TMD layers, which is well maintained even with scalable wafer-level growth.[5,45–47] Such intrinsic superiority is projected to be further promoted when they are merged with conventional 3D semiconductors yielding well-controlled 2D/3D heterojunctions, particularly for opto-electronic applications.[110] In general, such 2D/3D heterojunctions exist in two distinct configurations, i.e., lateral vs. vertical, determined by the ways that 2D layers are interfaced with the 3D materials. Although the lateral integration of small-sized 2D flakes onto 3D semiconductors has accomplished

high photosensitivity, the resulting devices exhibited limited photo-response speeds in the range of a few-to milli-seconds.[3, 111, 112] The vertical integration approach would provide advantages of small diffusion length and depletion dimensions for photo-generated carriers, thereby leading to faster photo-responsiveness. However, it remains difficult to achieve 2D/3D vertical junctions on a laterally large ( $\sim cm^2$ ) dimension via a scalable process avoiding the unreliable manual transfer of 2D layers.[113, 114]

Having fabricated 2D PtTe<sub>2</sub>/ 3D Silicon Schottky junction devices as described in previous section, we unveiled the “intrinsically” superior photovoltaic and photodetection performances of these 2D/3D schottky junctions over previously explored devices. Additionally in this chapter, we identified methods to “externally” further promote such superiority.

## Results and Discussion

### *Photovoltaic Performance*

Figure 6.1 shows the electrical properties of the stand-alone 2D PtTe<sub>2</sub> layers as well as the PtTe<sub>2</sub>/Si heterojunction devices. The CVD-2D PtTe<sub>2</sub> layers exhibit an extremely high electrical conductivity of  $\sim 10^5\text{--}10^6 S/m$  and intrinsically metallic transport characteristics irrespective of their layer numbers, as confirmed in previous section.[5] Having confirmed the highly metallic nature of 2D PtTe<sub>2</sub> layers, we developed the heterojunction devices by optimizing their layer thickness. Figure 6.1 a shows the photovoltaic characterization of the device incorporating 2D PtTe<sub>2</sub> layers prepared with Pt of an  $\sim 4.5$  nm thickness, revealing the current density–voltage (J–V) characteristics without (red) and with (blue) a solar illumination (intensity:  $400 W/m^2$ ). The device shows pronounced photovoltaic effects corroborated by a large amount of photo-induced current density in the reverse bias regime. Figure 6.1 b presents the corresponding J–V plot in a semi-log

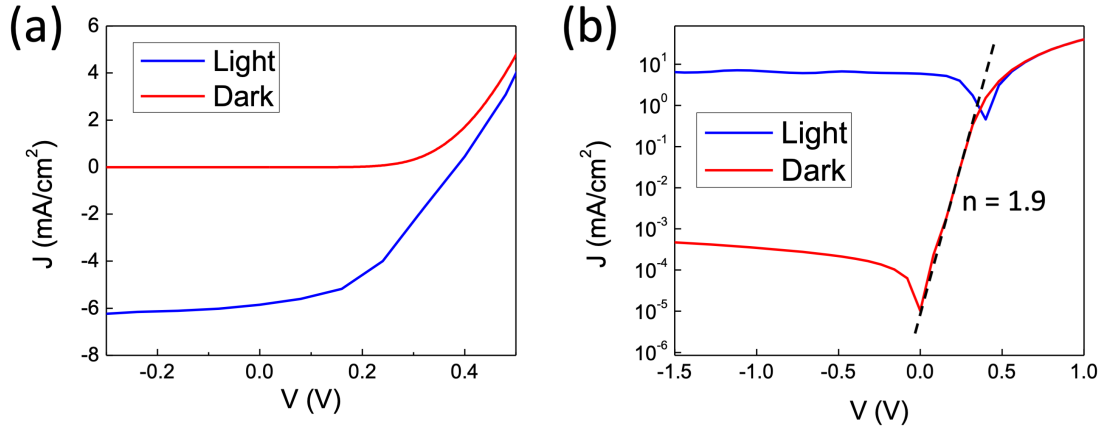


Figure 6.1: (a-b) Photovoltaics of PtTe<sub>2</sub>/p-Si devices prepared with Pt of 4.5 nm thickness; (a) J–V characteristics in the dark (red) and under illumination (blue), and (b) the corresponding presentation in the semi-log scale. Adapted with permission from Reference [7].

scale, yielding the following parameters; open circuit voltage ( $V_{oc}$ )  $\sim 0.41$  V, short circuit current density ( $J_{sc}$ )  $\sim 5.9$  mA/cm<sup>2</sup>, fill factor (FF)  $\sim 44\%$ , and rectification ratio  $\sim 10^5$  at  $\pm 1.5$  V. The device ideality factor,  $n$ , extracted from the linearity (black line) in the forward bias regime is  $\sim 1.9$  and the power conversion efficiency (PCE) is  $\sim 2.5\%$ . This observation of strong current rectification and photovoltaic characteristics confirms the presence of metal (PtTe<sub>2</sub>)–semiconductor (Si) Schottky junctions whose mechanism will be discussed in the next section. Additionally, we confirmed the Ohmic transport characteristics from 2D PtTe<sub>2</sub> layers and p-Si wafers interfaced with Au electrodes, which further confirms that the rectification originates from the junctions. We note that these PtTe<sub>2</sub>/Si heterojunction devices perform much better than the previously explored Pt TMD-based ones including platinum diselenide (PtSe<sub>2</sub>)/Si of comparable thickness,[6] i.e., an increase of  $\sim 15\%$  and  $\sim 47\%$  for  $V_{oc}$  and  $J_{sc}$ , respectively.

### Photodetection Performance

In addition to photovoltaics, we also investigated their photo-responsiveness using an illumination source of a fixed wavelength. Figure 6.2 a shows the semi log-scaled I–V characteristics of another device different from the one in Figure 6.1 a and b under intensity-varying illumination at 625 nm wavelength. The photocurrent at the reverse bias regime steadily increases with increasing intensity, reflecting the increasing concentration of photo-generated charge carriers.[111] Figure 6.2 b shows the time-dependent train of photocurrent generation at a zero external bias under periodic illumination of varying intensities revealing highly reliable photo-responsiveness. We also confirmed that the device was still very sensitive even at a much lower intensity of  $0.1 \text{ mW/cm}^2$ . Photo-responsivity and specific detectivity are two key parameters used to evaluate the photo-responsiveness performance of the device; photo-responsivity,  $R$ , indicates its efficiency in responding to changes in optical signals, whereas specific detectivity,  $D^*$ , delineates its ability to detect small signals. They are obtained from the following equations.[115, 116]

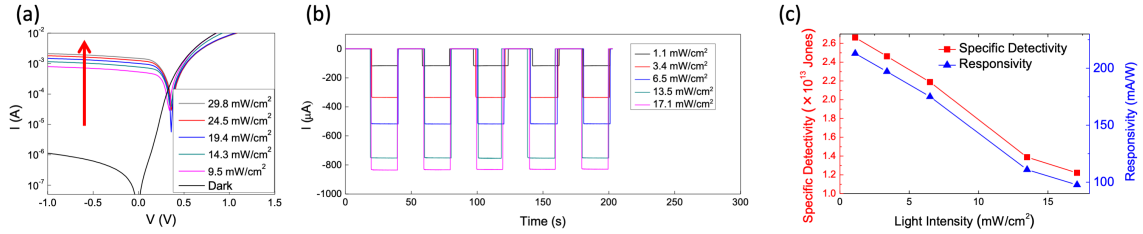


Figure 6.2: (a) I–V characteristics of a 2D PtTe<sub>2</sub>/3D Si device in the semi-log scale measured under 625 nm illumination of varying intensities. (b, c) Photo-responsiveness measured at zero external bias; (b) Temporal response of a device under 625 nm illumination of varying intensities. (c) Light intensity-dependent specific detectivity (red) and responsivity (blue) of the same device in (d). Adapted with permission from Reference [7].

$$R = \frac{I_{ph}}{P_{in}} \quad (6.1)$$

$$D^* = \frac{A^{\frac{1}{2}} R}{(2eI_d)^{\frac{1}{2}}} \quad (6.2)$$

where  $I_{ph}$ ,  $I_d$ ,  $P_{in}$ ,  $A$  and  $e$  are the photocurrent, dark current, incident light power, active device area, and elementary charge, respectively. Figure 6.2 c presents the plots of  $R$  (blue) and  $D^*$  (red) vs. light intensity extracted from the above equations for the  $\text{PtTe}_2/\text{Si}$  device at a zero external bias. Both  $R$  and  $D^*$  show the inverse relationship with intensity, consistent with the observations with other 2D/3D photodetectors.[96, 117, 118] The  $R$  value reaches up to  $0.213 \text{ A/W}$  at an intensity of  $1.1 \text{ mW/cm}^2$ , comparable to those of other 2D/3D photodetectors at a zero external bias.[115, 118, 119] Furthermore, the  $D^*$  value is as high as  $2.66 \times 10^{13}$  Jones, which is much higher than those of previously developed 2D/3D and stand-alone 2D devices – to be confirmed in the next section. This finding is particularly encouraging given that the lateral dimension of the active junction area in our device is quite large ( $1\text{cm} \times 0.5\text{cm}$ ), while previous developments mostly employed small-sized (typically,  $\sim m^2$ ) exfoliated 2D flakes. Additionally, the external quantum efficiency (EQE) of the device was extracted using the following equation:

$$EQE = \frac{h_c R}{e\lambda} \quad (6.3)$$

which yields a moderately high ECE of 42.2%. In the above equation,  $h$  is Planck's constant,  $c$  is the velocity of light,  $R$  is the responsivity, and  $\lambda$  is the wavelength of the illumination source. It is noted that the performance of our  $\text{PtTe}_2/\text{Si}$  device is comparable to those of the previously explored ones despite its much larger junction area.

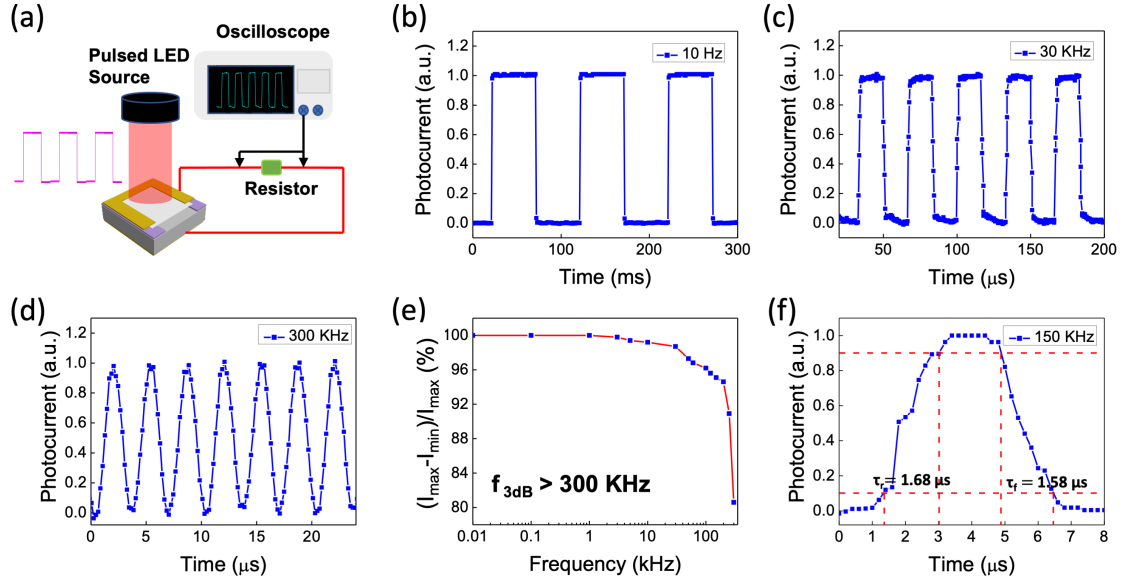


Figure 6.3: Schematic illustration of the experimental setup for recording the temporal photo-responsiveness of  $\text{PtTe}_2/\text{p-Si}$  devices under periodically pulsed 625 nm illumination. (b–d) Temporal photo-responsiveness of a device measured at varying illumination frequencies of (b) 10 Hz, (c) 30 kHz, and (d) 300 kHz. (e) Relative balance,  $(I_{\max} - I_{\min})/I_{\max}$ , of the same device as a function of illumination modulation frequency revealing a 3-dB cutoff frequency of  $>300$  kHz. (f) Magnified view of photo-switching characteristics obtained at 150 kHz clarifying rise ( $\tau_r$ ) and fall ( $\tau_f$ ) times. Adapted with permission from Reference [7].

### Characterization of Photoresponse Speed

Furthermore, we studied the practical suitability of the  $\text{PtTe}_2/\text{Si}$  device for high-performance photodetection applications. Particularly, photo-response speed is of paramount importance in optical communication and imaging applications as it dictates their efficiency for optical-to-electrical signal conversion. For the precise quantification of response speed, a 625 nm wavelength light was pulsed and introduced to the device using a signal generator as demonstrated in Figure 6.3 a. The temporal photo-response of the device at a zero external bias was recorded using a digital oscilloscope at several frequencies. Figure 6.3 b–d present the normalised transient photocurrents

generated by the pulsed illumination with frequencies of 10 Hz, 30 kHz and 300 kHz, respectively. The results show well-resolved and retained photo-responsiveness even up to a very high frequency of 300 kHz for multiple cycles, confirming fast and reliable photo-switching. Figure 6.3 e presents the relative current balance of the device, i.e.,  $(I_{max} - I_{min})/I_{max}$ , as a function of modulation frequency, where  $I_{max}$  ( $I_{min}$ ) is the maximum (minimum) current obtained at each frequency with (without) illumination over multiple cycles, respectively. A high balance of  $>95\%$  is well preserved up to a frequency of 100 kHz, after which it steadily attenuates with increasing frequencies. This current attenuation still maintains  $\sim 80.6\%$  of its maximum value even at a very high frequency of 300 kHz, significantly surpassing the 3-dB cut-off frequency standard in commercial applications.[120, 121] as well as the values observed with previously developed 2D/3D devices.[115, 116, 122]

Figure 6.3 f shows the representative plot of the photocurrent generation/decay transient characteristics obtained at 150 kHz, quantifying photoresponse intervals. The rise ( $\tau_r$ ) and fall ( $\tau_f$ ) times are determined from the 90% and 10% of the maximum current value, respectively, yielding  $\tau_r \sim 1.68 \mu s$  and  $\tau_f \sim 1.58 \mu s$ , respectively. What is noteworthy is that this PtTe<sub>2</sub>/Si device exhibits well-balanced characteristics of high photo-detectivity and fast photo-responsiveness, while responsivity,  $R$ , is observed to be similar in the measured wavelength range ( $\sim 600$ -850 nm),[115–117, 119, 121–125] both the response time and photodetectivity are much better than those observed with most of the 2D/3D, 2D/2D, and stand-alone 2D layer-based devices.[53, 112, 113, 116, 117, 122, 124, 126–135] This is particularly encouraging given the large ( $\sim 0.5 \text{ cm}^2$ ) lateral dimension of the PtTe<sub>2</sub>/Si junction enabled by the scalable CVD growth, while a large number of the previously developed ones are based on the manual integration of small-sized 2D flakes.[3, 112–114, 124, 127, 128, 134, 136, 137]

### Band Diagram

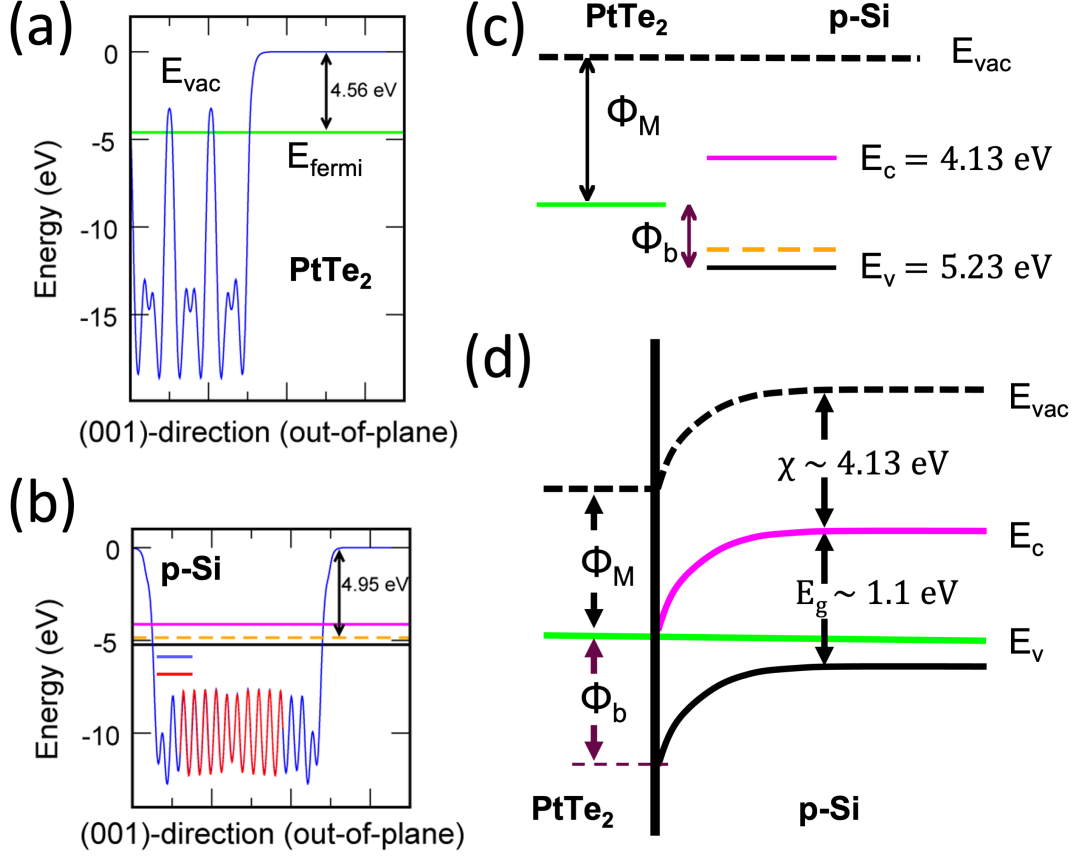


Figure 6.4: (a) PAEP diagram of few layered 2D PtTe<sub>2</sub> and its calculated work function, (4.56 eV, green line) with the vacuum level at 0 eV. (b) Determination of the work function of p-Si (4.95 eV, orange line) and band offsets by superimposing the PAEP of bulk Si on that of the slab and calibrating the vacuum level to 0 eV. (c) Energy band diagrams for 2D PtTe<sub>2</sub> and p-Si that form a p-type Schottky contact upon interfacing. (d) Band bending diagram revealing the presence of PtTe<sub>2</sub>/p-Si Schottky barrier whose height is determined to be 0.67 eV (violet line). Adapted with permission from Reference [7].

To confirm the charge transport mechanism of the device, we study the PtTe<sub>2</sub>/Si heterojunction contact characteristics by theoretically determining its Schottky barrier height using first principles calculations. The planar average electrostatic potential (PAEP) of the PtTe<sub>2</sub>/Si interface is computed in the out-of- plane direction along the Si (100) orientation, as presented in Figure 6.4

a. The work function of few-layered 2D PtTe<sub>2</sub>,  $\phi_M$ , is defined as  $\phi_M = E_{vac} - E_{Fermi}$ , where  $E_{vac}$  is the vacuum level set to 0 eV to calibrate the energy scale, and  $E_{Fermi}$  is the highest occupied electron energy state at 0 K. The work function value is determined to be  $\sim 4.56$ – $4.57$  eV with the layer number ranging from three to six.

We also computed the band offset and the work function of p-Si by superimposing the PAEP of bulk Si on that of the slab. The PAEP diagram in 6.4 b shows the work function of p-Si,  $\phi_{Si}$ , is  $\sim 4.95$  eV, determined from the experimental bandgap ( $\sim 1.1$  eV) of Si. Since the work function of the metallic 2D PtTe<sub>2</sub> layers is smaller than that of p-Si, a p-type Schottky junction is anticipated to form when these two materials are interfaced, as depicted in Figure 6.4 c. To determine the Schottky barrier height,  $\phi_b$ , for this junction, we refer to the known equation,  $\phi_b = E_g + \chi - \phi_M$ , [97] where  $E_g$  ( $\sim 1.1$  eV) is the bandgap and  $\chi$  ( $\sim 4.13$  eV) is the electron affinity of Si, and  $\phi_M$  is the work function of 2D PtTe<sub>2</sub> layers. We identify that 2D PtTe<sub>2</sub> layers form an obvious Schottky junction, yielding  $\phi_b = 0.67$  eV. Figure 6.4 d shows the diagram of the energy band bending at the PtTe<sub>2</sub>/p-Si interface, which strongly justifies that the experimentally observed characteristics are a result of 2D/3D Schottky junctions. In the diagram,  $E_c$ , and  $E_v$  represent the conduction and valence band edge of Si, respectively. We also determined the  $\phi_b$  value by analysing experimentally obtained I–V characteristics and observed good agreement with the theoretically calculated one.

### *Super-Hydrophobicity Driven Photovoltaic Improvement*

Lastly, we demonstrated externally tunable opto-electrical properties in the PtTe<sub>2</sub>/Si devices by taking advantage of the intrinsic structural uniqueness of 2D PtTe<sub>2</sub> layers. We identified that the large-area 2D PtTe<sub>2</sub> layers intrinsically exhibit “super-hydrophobic” surfaces as manifested by the very large ( $>110^\circ$ ) water contact angle as shown in Figure 6.5 a. Indeed, this hydrophobicity is the highest among all previously explored 2D TMD layers, [138] which can be exploited to further

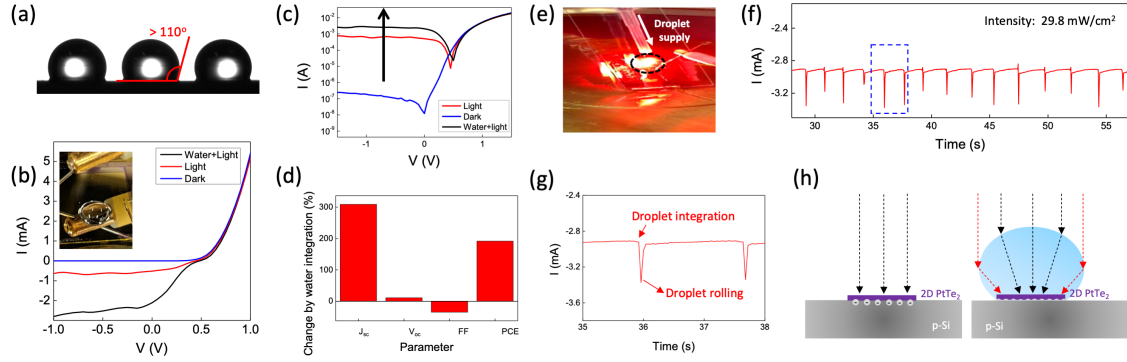


Figure 6.5: (a) Image of water droplets integrated on a  $\text{PtTe}_2$  /p-Si device. (b) I–V characteristics of the  $\text{PtTe}_2$  /p-Si device in the dark (blue), under illumination (red), and after integrating the water droplet shown in the inset (black). (c) I–V characteristics in the semi-log scale corresponding to (b). (d) Change of photovoltaic parameters induced by the water droplet integration in (b) and (c). (e) Integration of water droplets on the  $\text{PtTe}_2$  /p-Si device slanted at  $\sim 45^\circ$  under continuous illumination from a 625 nm LED source at an intensity of  $29.8 \text{ mW/cm}^2$ . (f) Temporal current obtained from the device in (e) with a periodic integration of water droplets at an interval of  $\sim 1.6$  s. (g) Enlarged view of the blue dotted region in (f) highlighting the current change by the droplet integration and rolling-off due to gravity. (h) Schematic illustration of the increased concentration of photo-generated carriers by the light concentration effect. Adapted with permission from Reference [7].

improve device performances as presented in Figure 6.5 b–g. Figure 6.5 b shows the representative I–V characteristics of an identical  $\text{PtTe}_2$ /Si device under three different conditions; i.e., in the dark (blue), under illumination (red), and under the same illumination with water droplet integration (black) which drastically improved the photovoltaic effect as manifested by a significant increase in reverse current. Figure 6.5 c shows the corresponding semi-log scaled I–V characteristics, better visualizing the photovoltaic enhancement.

Figure 6.5 d shows the summary of the water droplet-driven change in photovoltaic parameters, revealing enhancements in  $J_{sc}$  by  $\sim 309\%$ ,  $V_{oc}$  by  $\sim 9\%$ , PCE by  $\sim 192\%$ , and a reduction of FF by  $\sim 35\%$ . The much larger enhancement in  $J_{sc}$  over the other parameters indicates the significantly increased concentration of photo-generated charge carriers. Photo-responsiveness of another de-

vice slanted at  $\sim 45^\circ$  was also evaluated under a continuous illumination (29.8 mW/cm<sup>2</sup> intensity and 625 nm wavelength) by periodically integrating water droplets on it, as shown in Figure 6.5 e. Figure 6.5 f presents the corresponding temporal photo-responsiveness, revealing that a train of current spikes periodically appears following the periodic water droplet application. Figure 6.5 g corresponds to the blue box in Figure 6.5 f, highlighting the periodic and instant increase in reverse current upon integrating water droplets, measured at a voltage of - 2 V. The current reversibly returns to the original value once the droplets subsequently roll down from the sample surface and disappear. We believe that this significant increase in reverse current is the result of the light concentration effect introduced by the integrated water droplets; i.e. the hemispherical water droplet caused by the super-hydrophobic surface enables the in-ward refraction of incident light rays increasing the concentration of photo-generated charge carriers, as schematically illustrated in Figure 6.5 h.

The phenomenon is qualitatively consistent with the effects resulting from integrating light concentrating optical lenses on top of photovoltaic cells.[139] Indeed, Li et al. demonstrated significantly enhanced photovoltaic effects by directly integrating water droplets onto the surface of hydrophobic carbon-nanotube photovoltaic cells,[140] which well agrees with the observation in this study. As a control experiment to verify this hypothesis, we prepared a glass slide with hydrophobic coating and integrated it on top of the PtTe<sub>2</sub>/Si device. We then integrated water droplets on top of the glass slide/device and performed photovoltaic measurements, mimicking the experiments in Figure 6.5 f and g. As predicted, a significant increase in photocurrent is observed by integrating water droplets, which decisively confirms the super-hydrophobicity enabled light concentration effect.

## Conclusion

In summary, we have developed the large-area PtTe<sub>2</sub>/Si heterojunction devices by directly growing metallic 2D PtTe<sub>2</sub> multilayers on p-Si wafers and explored their photovoltaic and photodetection properties. The devices exhibit a comprehensive set of promising Schottky junction characteristics, i.e., large rectification ratio, small ideality factor, high photosensitivity and small photoresponse time. Extensive comparisons with previously explored 2D layer-based similar devices confirm their excellence in high-efficiency opto-electrical applications. Furthermore, the devices present improved performances upon integrating water droplets on their surfaces owing to the unusually high hydrophobic nature of 2D PtTe<sub>2</sub> layers. This study is believed to greatly broaden the versatility of 2D PtTe<sub>2</sub> layers – a relatively unexplored 2D crystal with high electrical conductivity – towards scalable 2D/3D hybrid device applications in a wide range of emerging opto-electronics.

## **CHAPTER 7: 2D PTTE<sub>2</sub>/3D SILICON SCHOTTKY JUNCTION FOR NEAR-TO-MID INFRARED PHOTODETECTION**

The content of this chapter has been published in:

M. S. Shawkat, S. B. Hafiz, M. M. Islam, S. A. Mofid, M. M. A. Mahfuz, A. Biswas, H.-S. Chung, E. Okogbue, T.-J. Ko, D. Chanda, T. Roy, D.-K. Ko, Y. Jung, “Scalable Van der Waals Two-Dimensional PtTe<sub>2</sub> Layers Integrated onto Silicon for Efficient Near-to-Mid Infrared Photodetection,” ACS Applied Materials Interfaces, vol. 13, no. 13, pp. 15542-15550, 2021.

### **Introduction**

Mid-infrared (MIR) radiation spans a vital part of the electromagnetic spectrum with special emphasis on spectroscopic applications employed for chemical analysis, military surveillance, and night vision.[141] The MIR-responsive active layers in current photodetectors are mostly based on thin-film or bulk materials composed of conventional three-dimensional (3D) compound semiconductors, for example, mercury cadmium telluride (MCT, HgCdTe alloys),[142] indium antimonide (InSb),[143] and their quantum-wells of complex structures and compositions.[144] However, their fabrication for MIR photodetectors to achieve desired performances are generally non-trivial. For instance, highly costly and sophisticated techniques (e.g., molecular beam epitaxy) are required to grow high-quality crystals, often entailing special conditions (e.g., cooling) for device operation.[145] Recently, two-dimensional (2D) materials have emerged as promising building blocks to alleviate these limitations owing to their rich set of unique properties; that is, tunable band gap energies covering a broad range of spectrum into MIR,[146, 147] thickness-dependent tunable optical absorption,[1, 6, 23] decently high carrier mobility,[36, 60] and relaxed assembly requirement

benefiting from their weak van der Waals (vdW) bonding.

Additionally, the ultra-thin nature of 2D materials enables a low thermal noise, eliminating the strict requirement of device cooling. Some proof-of-concept methods utilizing graphene and 2D transition metal dichalcogenides (TMDs) have been demonstrated for photodetection in the MIR regime and beyond.[141, 148–151] However, despite their intrinsic property advantages, these 2D materials are often limited to be employed as “stand-alone” active layers in MIR applications owing to their preparation issues. For example, while black phosphorus (BP) exhibits a small band gap energy of  $\sim 0.3$  eV and a high carrier mobility of  $\sim 1000$  cm<sup>2</sup>/Vs attractive for MIR detection, its poor air stability significantly limits resulting detection performance and reliability. Large-area graphene grown by a high temperature chemical vapor deposition (CVD) method generally requires an additional step of mechanical transfer and integration, severely limiting its process scalability.

Similarly, conventional 2D TMD layers employing refractory metals [e.g., molybdenum (Mo) or tungsten (W)] exhibit band gap energies matching the visible spectrum range and thus are less suitable for MIR detection compared to BP or graphene. Recently, there has been growing interest in “noble metals”-based 2D TMD layers which offer unparalleled properties such as small band gap energies matching the MIR range, low growth temperature, and high carrier mobility. Particularly, 2D platinum ditelluride (2D PtTe<sub>2</sub>) layers exhibit ideal combination of various essential properties such as an extremely high electrical conductivity of  $>10^6$  S/m [5, 45, 46] and a layer-number-dependent transition to a gapless metallic state.[9, 60] A variety of preparation methods have been explored,[46, 53] which have generally yielded randomly oriented small-sized 2D PtTe<sub>2</sub> flakes. A recently developed CVD method employing a thermal tellurization of Pt thin films enables their direct and deterministic growth on “wafer-scale” substrates even at a relatively low temperature of 400 °C.[5, 7, 47, 105] This combined advantage of relaxed preparation requirement and superior material properties projects unprecedented opportunities of 2D PtTe<sub>2</sub> layers for MIR detection,

which has remained largely unexplored till now.

In this chapter, we explore a new form of broadband MIR photodetectors by coupling 2D vdW-bonded PtTe<sub>2</sub> layers with 3D covalently bonded Si wafers through a CVD method. Even though stand-alone 2D PtTe<sub>2</sub> layers as well as Si wafers are not strongly MIR-sensitive, 2D PtTe<sub>2</sub>/Si heterojunctions are observed to exhibit a significant amount of photoexcited carriers under MIR illumination measured up to  $\sim 7 \mu\text{m}$  in wavelength. The underlying working principle of these 2D/3D MIR photodetectors is discussed in the context of Schottky junction characteristics enabled by ultra-thin metallic 2D PtTe<sub>2</sub> layers interfaced with semiconducting Si as well as their optical absorbance competition.

## Results and Discussion

### *Near Infrared Photodetection Performance*

Figure 7.1 presents key electrical and optical properties of 2D PtTe<sub>2</sub> layers as well as photodetection performances of 2D PtTe<sub>2</sub>/Si heterojunction devices. Figure 7.1 a presents the variation of optical transmittance and electrical conductivity of 2D PtTe<sub>2</sub> layers measured by an ultraviolet–visible (UV–vis) spectroscopy and a probe station, respectively. The plot reveals decreasing optical transmittance and increasing electrical conductivity with an increase of Pt seed thickness. Notably, 2D PtTe<sub>2</sub> layers are highly metallic, as confirmed in our previous studies,[7] reaching a high electrical conductivity of  $\sim 10^6 \text{ S/m}$ . [5] We then explored intrinsic transport characteristics of 2D PtTe<sub>2</sub>/Si devices and their photo-responsiveness under illumination. Figure 7.1 b represents a two-terminal current–voltage (I–V) curve obtained from a representative device prepared with Pt of  $\sim 4.5 \text{ nm}$  thickness. Highly asymmetric I–V characteristics are observed in dark, yielding a large rectification ratio of  $\sim 10^4$  defined at  $\pm 2 \text{ V}$ . This strong rectification originates from a Schottky

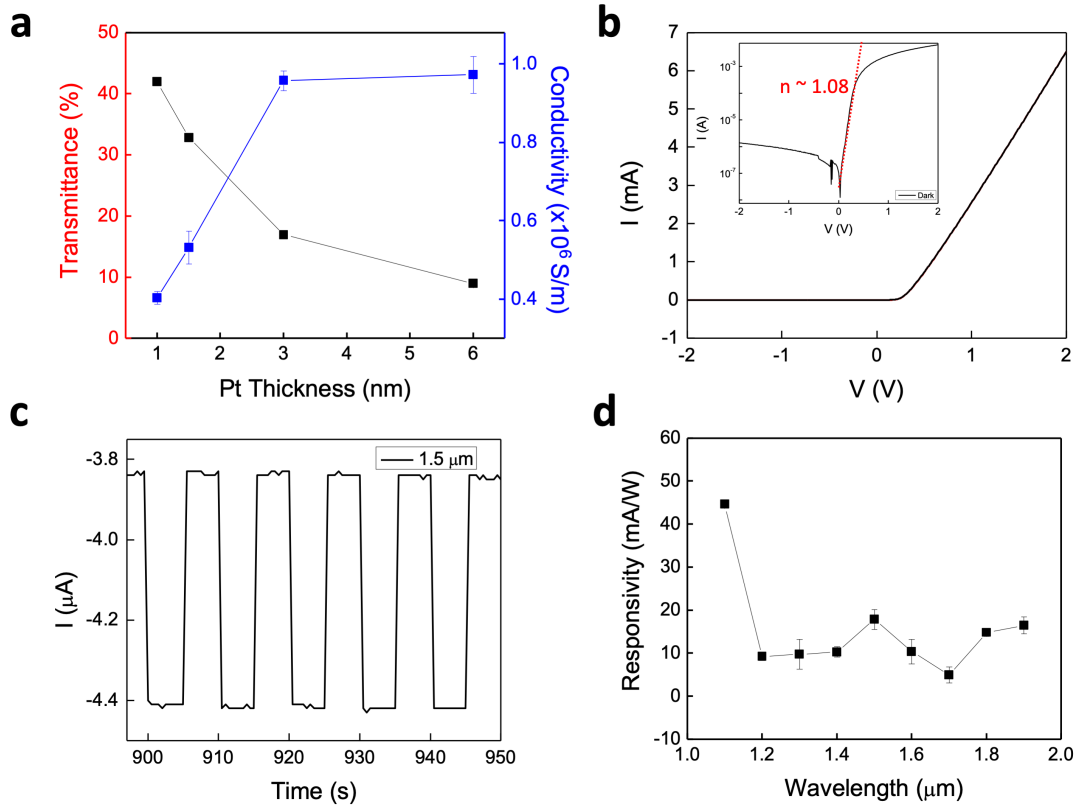


Figure 7.1: (a) Plot of optical transmittance (red) vs electrical conductivity (blue) for 2D PtTe<sub>2</sub> layers prepared with varying Pt thickness values. (b) I–V curve in dark and its corresponding semilog plot (inset) denoting an ideality factor of  $\sim 1.08$ . (c) Temporal photo-response of the same device in (b) under 1.5  $\mu$ m illumination. (d) Illumination wavelength-dependent responsivity. Adapted with permission from reference [7].

junction enabled by metallic 2D PtTe<sub>2</sub> layers interfaced with a semiconducting Si, as previously clarified.[7] We further analyzed the I–V characteristics by employing a thermionic emission transport model. Within a forward bias regime of  $V > \sim \frac{3kT}{q}$ , the current transport through a Schottky diode can be expressed as following.[152]

$$I \approx I_0 e^{\frac{V - IR_s}{n k T / q}} \quad (7.1)$$

$$I_0 \approx AA^*T^2 e^{\frac{-\phi_B}{kT}} \quad (7.2)$$

where  $n$ ,  $V$ ,  $R_s$ ,  $k$ ,  $T$ ,  $q$ ,  $A$ ,  $A^*$ , and  $\phi_B$  are the device ideality factor, bias voltage, series resistance, Boltzmann's constant, temperature, elementary charge, device active area, Richardson's constant, and Schottky barrier height, respectively. Excellent agreement is observed between the experimental versus modeled I–V characteristics with the  $\phi_B \sim 0.84$  eV. The inset shows the corresponding semilog plot where a device ideality factor of  $\sim 1.08$  is extracted from the linear fit (red dotted line) in the forward bias regime. This ideality factor being close to unity combined with the large rectification ratio indicates a high quality of the Schottky junction (i.e., minimal trap-assisted recombination in the depletion region). The photo-responsiveness of the device was first investigated at the near-infrared (NIR) regime ranging  $\sim 1.1$ – $1.9$   $\mu\text{m}$  in wavelength. Figure 7.1 c presents temporal photo-response obtained from the same device under a periodic NIR illumination of  $1.5$   $\mu\text{m}$  in wavelength. The results confirm a significant generation of NIR-excited photocarriers, measured at a constant bias of  $-2$  V under  $0.1$   $\text{mW}/\text{cm}^2$  intensity.

One of the key performance metrics for photodetection is responsivity, which is defined as the ratio of the photocurrent to the optical power of incident radiation.[7] Figure 7.1 d presents a plot of responsivity versus illumination wavelength in the NIR range of  $\sim 1.1$ – $1.9$   $\mu\text{m}$ . The responsivity initially decreases after  $\sim 1.1$   $\mu\text{m}$ , possibly due to the significant absorbance reduction in Si,[96, 116] and then it becomes nearly saturated beyond that wavelength. Interestingly, the responsivity is observed to be significantly larger than the values previously observed with stand-alone 2D  $\text{PtTe}_2$  layers in the similar wavelength range; for instance, at a wavelength of  $1.5$   $\mu\text{m}$ , the responsivity for the 2D  $\text{PtTe}_2/\text{Si}$  device is observed to be  $\sim 13$   $\text{mA}/\text{W}$ . This value is approximately 1000 times larger than that from stand-alone 2D  $\text{PtTe}_2$  layers at the same wavelength[153] despite the significantly larger ( $> 10^{10}$  times) active area of the device. 2D materials can absorb IR radiation in a wide

range of wavelengths through interband and/or intersubband transitions,[154, 155] while precise electronic structures and transition mechanisms of 2D PtTe<sub>2</sub> layers need to be further investigated.

Photoexcited carriers can give rise to photocurrent if they are energetically positioned to overcome the Schottky barrier via thermionic or thermionic-field emission (typically, reverse-biased operation). The achievable cutoff wavelength of our 2D PtTe<sub>2</sub>/Si Schottky diode is then predominantly determined by the height of the potential barrier. Analysis of the I–V characteristics (Figure 7.1 b) reveals the presence of a Schottky junction with an appropriate barrier height enabling the device to generate photoexcited carriers even at longer wavelengths.

#### *Mid Infrared Photodetection Performance*

Figure 7.2 a shows a representative plot of the temporal photocurrent measurement carried out by illuminating the device with MIR radiation with the photon wavelength longer than 2  $\mu\text{m}$ . The radiation was provided by a calibrated blackbody heated at 900 °C, which was then filtered through germanium (Ge) that only allowed mid- to long-IR radiation to pass through. A distinct increase in the photocurrent suggests that our device is indeed responsive in the thermal IR regimes. To further identify the photo-response characteristics, spectral photocurrent measurements were then carried out by replacing the Ge filter with various Fabry–Perot band-pass filters having a center wavelength in the  $\sim 2\text{--}7\ \mu\text{m}$  range, as shown in Figure 7.2 b. Interestingly, an appreciable photocurrent was observed up to 7  $\mu\text{m}$  even at room temperature (Figure 7.2 c), although a large number of thermal carriers present at 300 K are expected to annihilate photogenerated carriers through the Auger recombination process, which typically necessitates device cooling.[156, 157] The quality of a photodetector is evaluated with specific detectivity,  $D^*$ , a performance parameter defined by

$$D^* = \frac{R\sqrt{A\Delta f}}{I_n} \quad (7.3)$$

where  $A$ ,  $\Delta f$ ,  $I_n$ , and  $R$  are the device area, detection bandwidth, noise current, and responsivity, respectively.[158] Here, the optical power of the incident radiation for each specific filter was calculated based on the spectral irradiance of the calibrated blackbody estimated from the Planck radiation formula expressed as follows

$$P = AW \frac{a^2}{4d^2} t\eta \quad (7.4)$$

where  $A$  ( $0.5 \text{ cm}^2$ ),  $W$ ,  $a$  ( $2.54 \text{ cm}$ ),  $d$  ( $13.5 \text{ cm}$ ),  $t$  ( $0.92$ ), and  $\eta$  ( $1.33$ ) are the device area, emittance of radiation for each specific filter, diameter of the source aperture, source aperture to device distance, transmission of the optical path, and amplification factor of the parabolic mirror, respectively. The inset in Figure 7.2 b shows the calculated optical power at each center wavelength. With the measured noise current density of  $3.3 \times 10^{-12} \text{ A}\cdot\text{Hz}^{-1/2}$  at  $150 \text{ Hz}$ , specific detectivity values were plotted as a function of wavelength, as shown in Figure 7.2 d. While the device detectivity remains nearly constant in the low wavelength regime, it steadily increases beyond  $\sim 6 \mu\text{m}$ . The obtained specific detectivity values are on par with some of the earlier studies on various nanomaterials studied at the similar wavelength range.[159, 160] Based on the observed trend, the cutoff wavelength of our 2D  $\text{PtTe}_2/\text{Si}$  device is believed to exist beyond the wavelength limit of the current optoelectronic measurement setup, that is,  $7 \mu\text{m}$ , thus warranting further investigation.

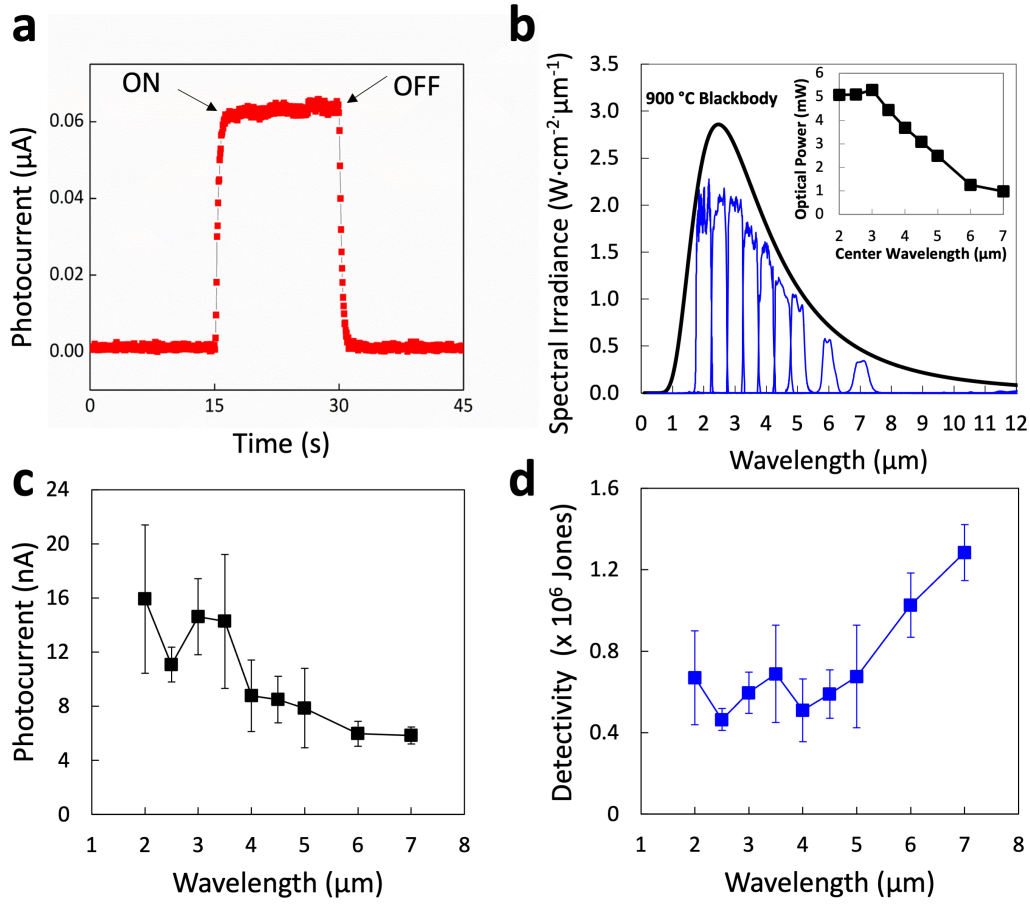


Figure 7.2: (a) Plot of MIR photocurrent measured using 900 °C-calibrated blackbody radiation filtered with Ge as an illumination source. (b) Spectral irradiance of the blackbody obtained from a band-pass filter in a center wavelength range of 2–7  $\mu\text{m}$ , estimated using the Planck radiation formula. The inset displays the calculated optical power obtained by integrating the area under the respective blue curves at each wavelength. (c) Photocurrents measured with illumination of varying wavelengths. (d) Illumination wavelength-dependent specific detectivity. All measurements were conducted at room temperature 300 K using a constant bias of - 0.6 V. Adapted with permission from reference [7].

### *Fourier Transform IR (FTIR)*

To gain insights into the working principle of the observed wavelength-dependent detectivity, we performed Fourier transform IR (FTIR) spectroscopy characterization. Figure 7.3 a presents ab-

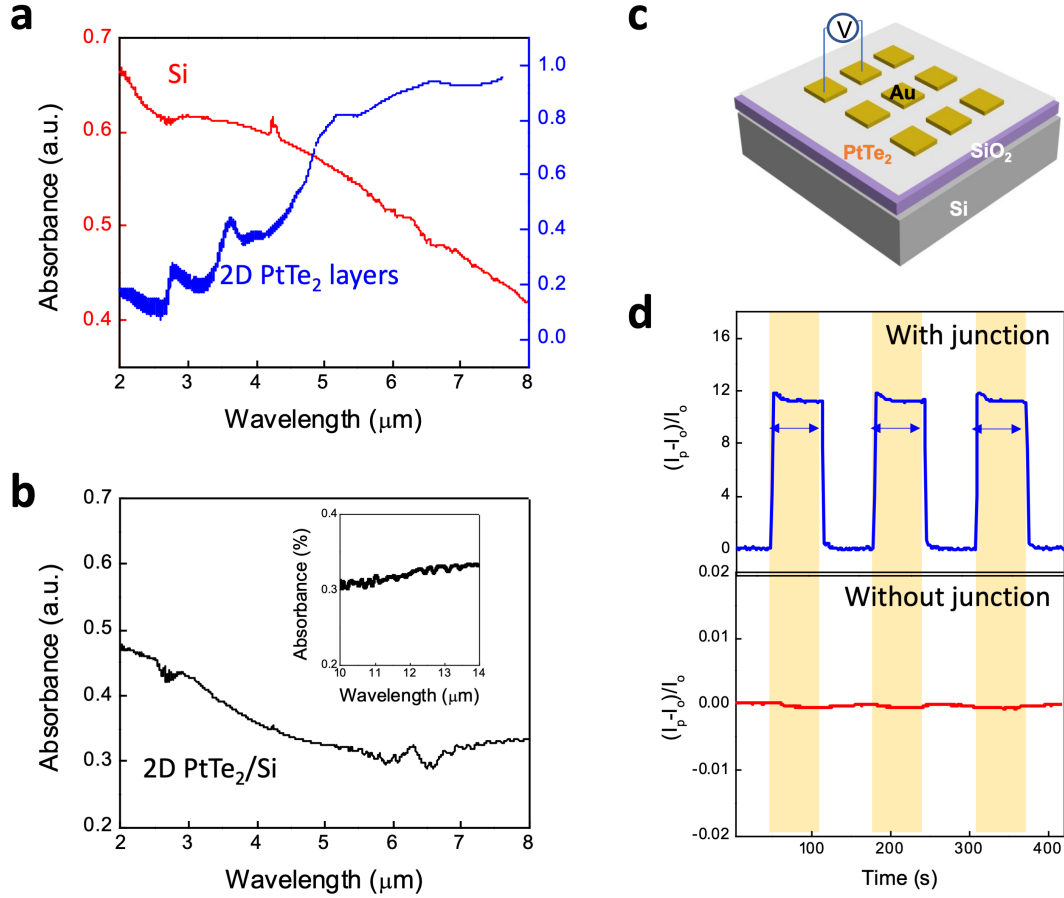


Figure 7.3: (a) FTIR absorbance spectra of a bare Si wafer (red) and 2D PtTe<sub>2</sub> layers integrated on a glass (blue). (b) FTIR absorbance spectrum of a 2D PtTe<sub>2</sub>/Si device and the corresponding characteristics up to 14 μm in wavelength (inset). (c) Schematic illustration of a stand-alone 2D PtTe<sub>2</sub> layer-based device. (d) Temporal photo-response of devices with and without the 2D PtTe<sub>2</sub>/Si junction. The device with the junction was characterized with an illumination frequency of 1000 Hz (blue arrow). Adapted with permission from reference [7].

sorbance spectra of a bare Si wafer as well as 2D PtTe<sub>2</sub> layers on a glass substrate. It is observed that the Si wafer displays decreasing absorbance with the increasing wavelength, while the 2D PtTe<sub>2</sub>/glass sample exhibits the opposite characteristics. Furthermore, we performed FTIR characterization of a 2D PtTe<sub>2</sub>/Si device, as presented in Figure 7.3 b. Despite the continued decrease of absorbance in the Si wafer (Figure 7.3 a), the device shows a slight increase in absorbance beyond

$\sim 6 \mu\text{m}$  in wavelength, which becomes continuously pronounced even with the longer wavelength (inset). This observation indicates that the decreasing absorbance of the underlying Si wafer in the 2D PtTe<sub>2</sub>/Si device is efficiently compensated by the increasing absorbance of 2D PtTe<sub>2</sub> layers. Accordingly, the overall absorbance of the device continuously increases after a certain critical wavelength, that is,  $\sim 6 \mu\text{m}$ , which possibly accounts for the wavelength-dependent increase of detectivity shown in Figure 7.2 d.

Furthermore, to better clarify an exclusive role of the 2D PtTe<sub>2</sub>/Si Schottky junction in resulting IR photodetection, we performed a control experiment by exploring a device without the junction. Figure 7.3 c shows a schematic illustration of the device where patterned 2D PtTe<sub>2</sub> layers are directly grown on a SiO<sub>2</sub>/Si wafer, and their responsivity was evaluated by a two-terminal characterization under IR illumination. Figure 7.3 d presents plots of temporal photo-response obtained from the devices with (top panel) and without (bottom panel) the Schottky junction, manifested by a photocurrent ratio, that is,  $(I_p - I_0)/I_0$ , where  $I_p$  is the IR-induced photocurrent and  $I_0$  is the dark current. The device without the junction corresponding to Figure 7.3 c does not exhibit pronounced photocurrent in sharp contrast to the one with the junction, evidencing that the presence of the junction is essential for improved IR detection.

### *Opto-Mechanical Characterization*

Lastly, we extend the scope of this study by exploring mechanically flexible IR photodetectors employing 2D PtTe<sub>2</sub> layers grown on thin ( $50 \mu\text{m}$ ) Si wafers. Figure 7.4 a demonstrates the mechanical flexibility of a thin Si wafer supported on a plastic substrate (top panel) and shows an image of a fabricated 2D PtTe<sub>2</sub>/Si device (bottom panel). Figure 7.4 b presents plots of temporal photo-response obtained from the corresponding device, represented as a photocurrent ratio of  $(I_p - I_0)/I_0$ . The results confirm illumination intensity-dependent photocurrent generation with well-

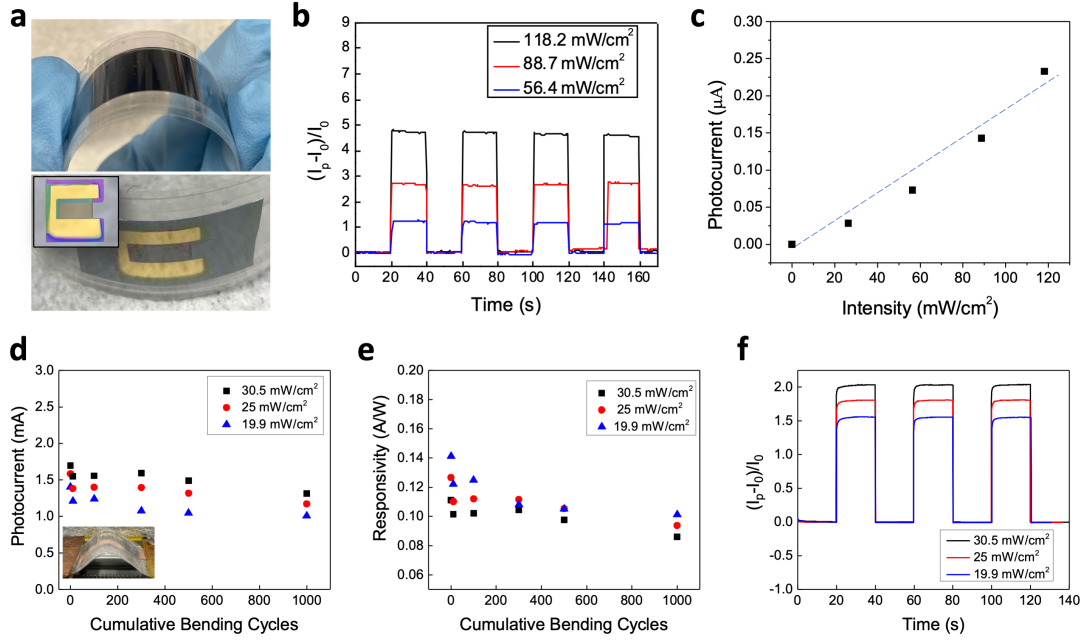


Figure 7.4: (a) Images of a thin Si wafer under bending (top) and a 2D PtTe<sub>2</sub>/Si flexible photodetector (bottom). The inset shows the top view of the device prior to its attachment to the supporting substrate. (b) Intensity-dependent temporal photo-response obtained from the flexible 2D PtTe<sub>2</sub>/Si device at an illumination wavelength of 0.94 m. (c) Plot of photocurrent vs illumination intensity. (d) Plot of photocurrent vs bending cycles for a flexible device subjected to a reduction of lateral length by 20%. (e) Plot of responsivity vs bending cycles. (f) Plot of intensity-dependent temporal photo-response obtained after a completion of 1000 bending cycles. Adapted with permission from reference [7].

defined responsiveness. Figure 7.4 c shows a plot of photocurrent generation versus illumination intensity showing high linearity, which suggests that the flexible device reliably responds to the illumination of varying intensities.

Furthermore, mechano-optoelectrical properties of the flexible device were characterized by cyclic bending tests. The device was subjected to a sequential application of bending/unbending for a large number of cycles, where the bending degree was set to be a 20% reduction of its original lateral length. Figure 7.4 d shows a plot of illumination intensity-dependent photocurrents with varying cycle numbers, and the insets shows a representative image of a device at its 20% bent

state. Figure 7.4 e shows a plot of illumination intensity-dependent responsivity corresponding to Figure 5d. After 1000 cycle numbers, only  $\sim 20$  and  $\sim 27\%$  reduction of photocurrent (Figure 7.4 d) and responsivity (Figure 7.4 e) are observed, respectively. Figure 7.4 f presents a plot of intensity-dependent temporal photo-response after a completion of cumulative bending/unbending tests for 1000 cycles, confirming the reliable operation of the device.

### Conclusion

In conclusion, we explored IR photodetection of 2D PtTe<sub>2</sub> layers directly integrated onto Si wafers. 2D PtTe<sub>2</sub>/Si Schottky junctions exhibited excellent photo-responsiveness in a NIR-to-MIR spectral range of  $\sim 1\text{--}7\ \mu\text{m}$  owing to the diminished carrier recombination manifested by their close-to-unity ideality factor. A wavelength-dependent increase of specific detectivity was observed beyond  $5\ \mu\text{m}$ , which was attributed to be the result of absorbance competition between 2D PtTe<sub>2</sub> layers versus Si. Furthermore, the low-temperature growth nature of 2D PtTe<sub>2</sub> layers enabled us to create mechanically flexible photodetectors where the presence of 2D PtTe<sub>2</sub>/Si Schottky junctions was identified to be critical for IR photodetection. This study is projected to greatly broaden the versatility of Si-based IR photodetectors by incorporating 2D materials in a simple and cost-efficient manner.

## **CHAPTER 8: WATER-ASSISTED TRANSFER AND VAN DER WAALS ASSEMBLY OF NEAR-ATOM THICKNESS HETERO-MEMBRANES**

The content of this chapter has been published in:

M. S. Shawkat, S. S. Han, H.-S. Chung, S. A. Mofid, C. Yoo, and Y. Jung, “Wafer-Scale Van der Waals Assembly of Free-Standing Near Atom Thickness Hetero-Membranes for Flexible Photo-Detectors,” *Advanced Electronic Materials*, vol. 7, no. 8, p. 2100395, 2021.

J.H. Kim, T.J. Ko, E. Okogbue, S.S. Han, M.S. Shawkat, M.G. Kaium, K.H. Oh, H.-S. Chung, Y. Jung, “Centimeter-scale Green Integration of Layer-by-Layer 2D TMD vdW Heterostructures on Arbitrary Substrates by Water-Assisted Layer Transfer,” *Scientific Reports*, vol. 9, no. 1, 1641, 2019.

### **Introduction**

Creating functional hetero-structures by rationally integrating dissimilar materials provides opportunities to develop building blocks used in many optoelectronic device systems such as quantum cascade lasers and light emitting diodes. Commonly adopted methods primarily rely on the sequential chemical growth of constituting materials in an epitaxial manner using molecular beam epitaxy (MBE) or metal-organic chemical vapor deposition (MOCVD). However, these chemical growth-based integration approaches require stringent lattice-matching constraints to preserve the material quality of each individual device component. Furthermore, they often involve chemical reactions of materials at very high temperatures and thus significantly limit the choice of underlying substrates. To overcome these limitations, alternative approaches have been explored toward the physical assembly of chemically and structurally distinct materials in a deterministic

manner. In this regard, Van der Waals (vdW) assembly methods have been recently gaining increasing attention as they enable the “non-chemical” integration of intrinsically low-dimensional materials.[161–164] They adopt the heterogeneous assembly of physically disjointed materials in a layer-by-layer manner, thus are intrinsically free of the lattice-matching epitaxial constraints in conventional chemical approaches. Heterogeneous vdW assemblies of various functional materials have been previously demonstrated, resulting in a successful development of unconventional devices.[20, 165–168] However, the previous demonstrations were mainly limited to integrating “layered” 2D crystals such as graphene and transition metal dichalcogenides (TMDs) possessing anisotropic crystallography.[10, 169–171] The versatility of the vdW assembly approach has yet to be extended to integrate “non-layered” covalently-bonded 3D materials of more common structures. Furthermore, the lateral dimensions of the vdW-assembled 2D TMD or graphene/2D TMD hetero-materials are generally very small, that is, typically,  $<100\ \mu\text{m}^2$ , [170, 172, 173] inadequate for the manufacturing scalability demanded for matured device technologies.

In this chapter, we report on a wafer-scale vdW integration of layered 2D TMDs and non-layered 3D membranes realizing heterojunctions on flexible substrates. Finally, we demonstrate hetero-materials of wafer-scale 2D platinum ditelluride ( $\text{PtTe}_2$ ) metallic[5] multi-layers and 3D platinum sulfide ( $\text{PtS}$ ) non-layered semiconductors via thermally assisted conversion method in a CVD furnace. We created large-area ( $>\text{cm}^2$ ) 2D/3D heterostructures of near atom thickness. This method offers significant advantages over the existing Van der Waals assembly approaches, as it enables the production of near atom thickness hetero-junctions on a wafer-scale without necessitating additional supporting polymers.[174] This method projects forming un-conventional hetero-junctions with tailored band offsets and also transfer of hetero-membranes onto substrates with unconventional form factors or melting temperatures, widening the versatility of these hetero-membranes.

## Results and Discussion

### *Water-Assisted Transfer and Van Der Waals Assembly Method*

Figure 8.1 schematically illustrates the water-assisted delamination of large area nano-membranes from their  $\text{SiO}_2/\text{Si}$  growth substrate onto an assortment of substrates. The process involves following steps: (1) Deposition of thin-film of precursor metal onto growth substrates (i.e.,  $\text{SiO}_2/\text{Si}$ ). (2) Thermally assisted conversion of precursor metal via chemical vapor deposition (CVD). (3) Delamination of the nano-membrane grown on  $\text{SiO}_2/\text{Si}$  substrates followed by submerging inside water, re-use of substrate for growth is optional (4) Transfer of nano-membranes onto secondary substrate via mechanical scooping inside water. The growth of nano-membranes follows similar process described in previous section for growth of  $\text{PtSe}_2$  and  $\text{PtTe}_2$ . This water-assisted nano-membrane separation happens due to surface energy difference between growth substrate and as-grown nanomembrane. Mechanism will be discussed in detail in later section. It is important to note that this process only uses water and no additional chemicals for the delamination and transfer of nano-membranes is not required. This method is in stark contrast to previous approaches that required use of polymeric protective materials and chemical etchants for the removal of  $\text{SiO}_2$ . [175] Due to this method, the nano-membranes do not go through chemical degradation posed by some of chemicals used, e.g. hydrogen fluoride (HF) or strong bases (sodium or potassium hydroxide (NaOH or KOH)). [176, 177] Moreover, there is the added advantage of avoiding structural damage due to rinsing polymer protective layer with solution-based chemicals (e.g. acetone).

### *Mechanism for Water-Assisted Method*

Figure 8.2 demonstrates the water-assisted vdW delamination/assembly method and studies the underlying mechanism. Figure 8.2 a presents time-lapsed snapshots of PtS membranes sequentially

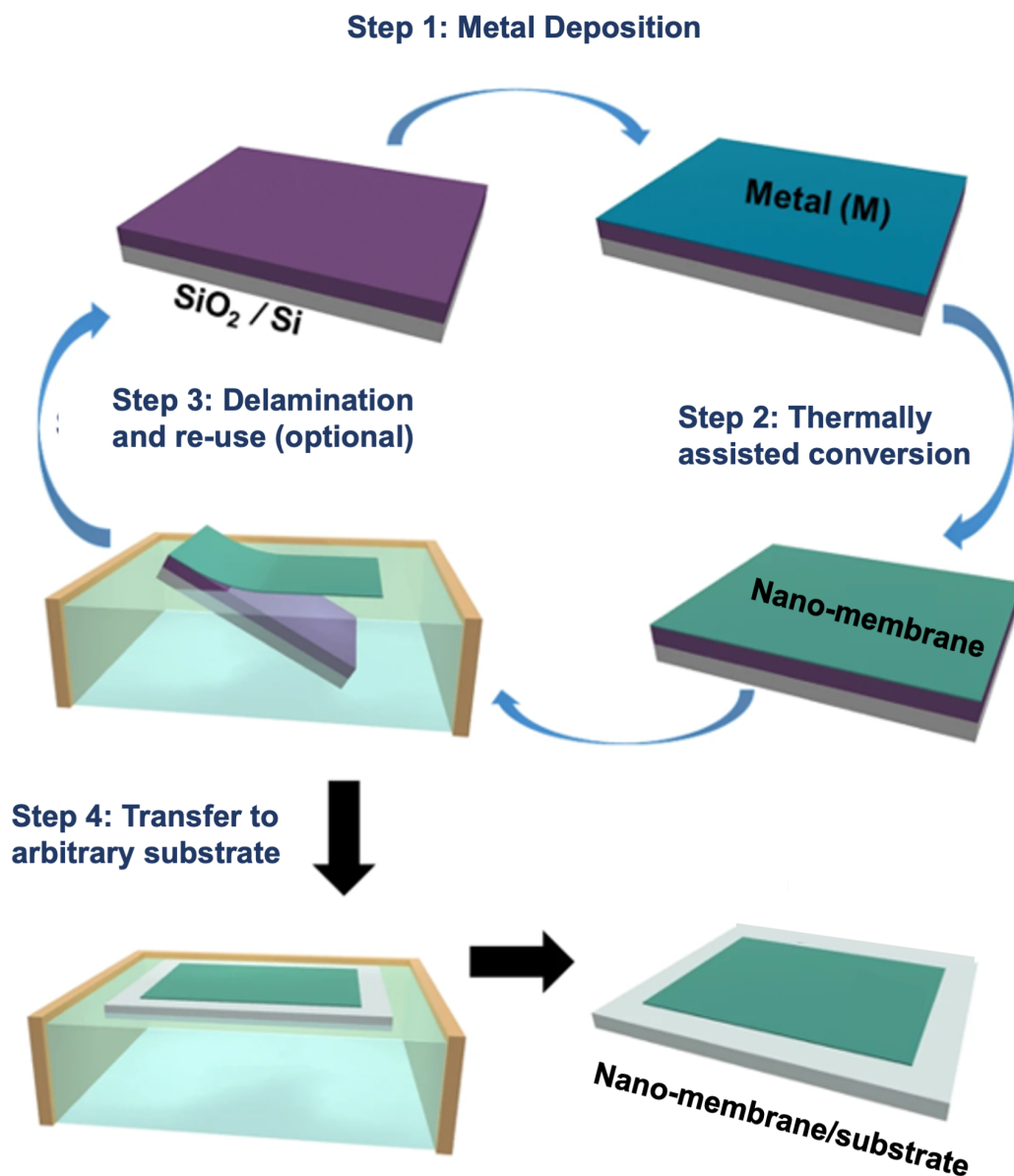


Figure 8.1: (a) Schematic illustration describing water-assisted, polymer-free green integration of CVD-grown nano-membranes on arbitrary substrates. Adapted with permission from reference [10].

undergoing delamination inside water. The underlying principle for this water-assisted preparation of PtS membranes can be understood by the capillary force-driven delamination of thin films.[178]

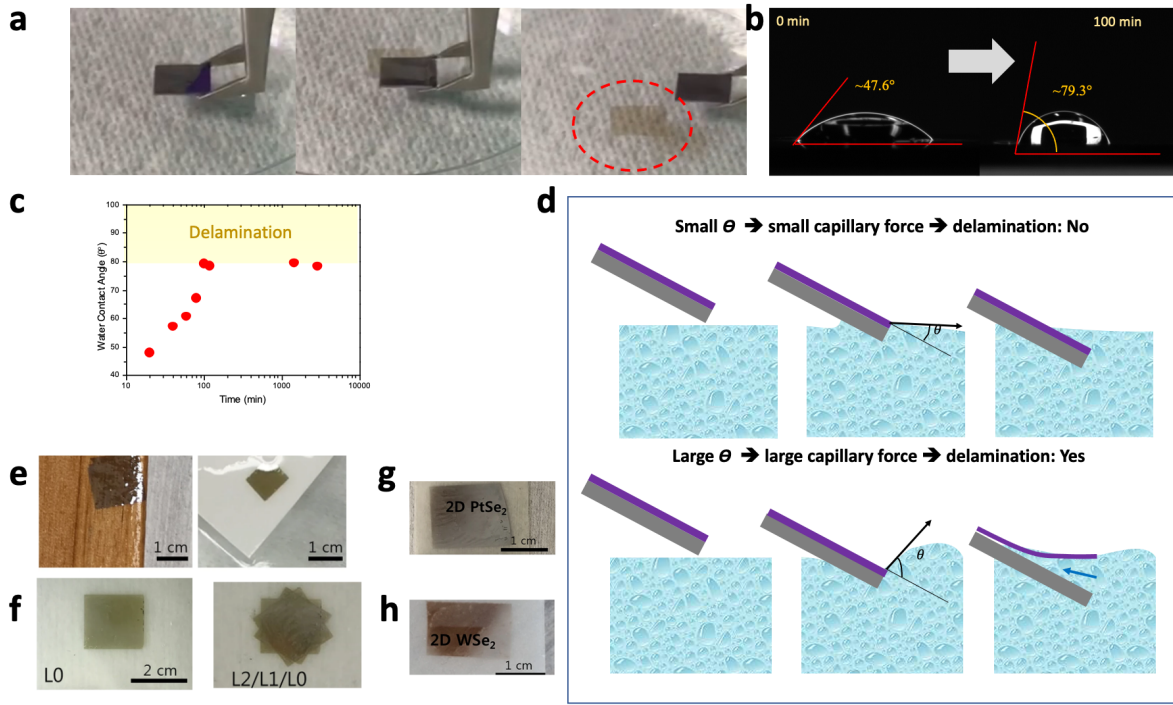


Figure 8.2: Mechanism of water-assisted transfer. Schematic illustration of the water-assisted integration of 2D PtTe<sub>2</sub> layers and 3D PtS membranes on arbitrary substrates. (a) Time-lapsed images displaying the water-assisted delamination of 3D PtS membranes. The red dotted circle denotes the delaminated membrane floating on the water surface. (b) Water droplet images and WCA measurements of a similar sample at its pristine (left) and aged (right) state. (c) Plot of time-dependent WCA values. (d) Comparison of the delamination efficacy for the samples with two distinct water wettability. (e) Representative image of 2D MoS<sub>2</sub> on an assortment of unconventional substrates, e.g. wood and paper. (f) Demonstration of the vdW assembly of multiple layers of 2D MoS<sub>2</sub> onto a PET substrate. L0, L1, L2 represent first, second and third time integration of MoS<sub>2</sub> layers. Integration of 2D WSe<sub>2</sub> layers (g) and 2D PtSe<sub>2</sub> layers (h) onto PET substrates. Adapted with permission from reference [10, 11].

When “hydrophobic” thin films grown (or, deposited) on hydrophilic substrates such as SiO<sub>2</sub>/Si wafers are exposed to water, the film/substrate interfaces experience the capillary peeling force,  $F$ , which determines the surface properties of the films. It is known that  $F = \gamma (1 - \cos \theta)$  where  $\gamma$  is the water surface tension capillary force, and  $\theta$  is the water contact angle.[178] This equation

indicates that thin films of higher hydrophobicity (thus, larger  $\theta$ ) are more prone to water-driven delamination with a larger driving force,  $F$ . To verify this idea, we identified the water wettability of PtS-grown SiO<sub>2</sub>/Si wafers by measuring their water contact angle (WCA) values (Figure 8.2 b). An as-prepared PtS thin film sample exhibited modest hydrophobicity manifested by the WCA of  $\approx 47.6^\circ$  (Figure 8.2 b, left) where it did not become delaminated in water.

Interestingly, it exhibited increasing hydrophobicity with progressive air exposure, manifested by the WCA of  $\approx 79.3^\circ$  (Figure 8.2 b, right). Once it reached a saturated WCA of  $\approx 80^\circ$ , it started to become spontaneously delaminated in water upon immersion for less than 1 min. Figure 8.2 c presents the corresponding plot of time-dependent WCA values for the sample. This observation supports that the delamination is indeed dictated by the capillary peeling force,  $F = \gamma (1 - \cos \theta)$  which should overcome a certain energy barrier for the initiation of the delamination.[178] The surface energy of the PtS film at the moment of its delamination is calculated to be  $\approx 44.37$  mN/m.[5] The air-exposure driven increase of hydrophobicity has also been observed with other vdW layered 2D TMD materials,[179, 180] while its exact origin needs to be clarified with further investigations. The illustrations in Figure 8.2 d compare the efficacy of the water-assisted delamination for the samples of low (top) versus high (bottom) hydrophobicity.

Figure 8.2 e-h shows the successful water-assisted integration of 2D TMDs onto a variety of unconventional substrates which would be difficult to achieve otherwise. Figure 8.2 e,f shows the images of centimeter-scale 2D MoS<sub>2</sub> layers integrated on a piece of (e) wood and (f) paper. The results highlight the strength and generality of our water-assisted integration approach which works for nano-membranes of layered 2D TMDs as well as non-layered PtS. Figure 8.2 f demonstrates the “layer-by-layer” integration of 2D MoS<sub>2</sub> on a piece of polyethylene terephthalate (PET) substrate achieved over an area of  $\sim 2\text{cm}^2$ . After the initial integration of original 2D MoS<sub>2</sub> layers (denoted, L0), additional layers of 2D MoS<sub>2</sub> were stacked on top of each other, denoted as (L1) and (L2) via the water-assisted layer transfer. Moreover, we demonstrate this layer transfer approach works for

materials beyond non-layered PtS and layered MoS<sub>2</sub>, including 2D tungsten (W) or platinum (P) diselenides (2D WSe<sub>2</sub> and 2D PtSe<sub>2</sub>). Figure 8.2 g, h show the images of centimeter-scale CVD-grown 2D PtSe<sub>2</sub> and 2D WSe<sub>2</sub> layers transferred and integrated on PET substrates, respectively.

### *PtTe<sub>2</sub>/PtS Hetero-Membranes for Near Infrared Photodetection*

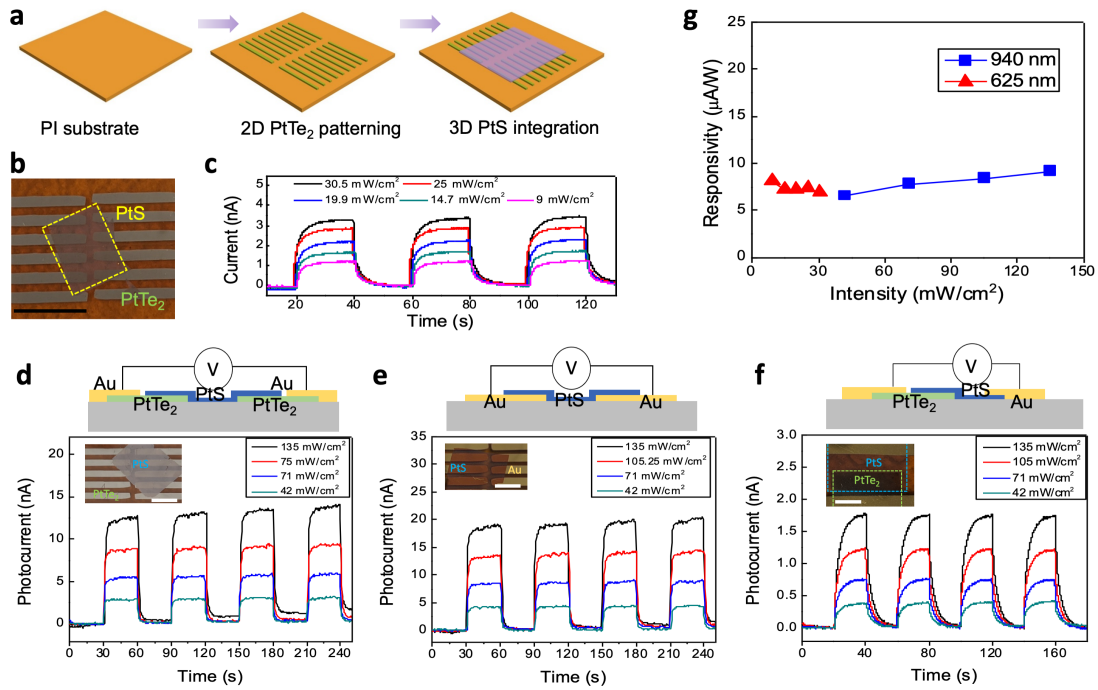


Figure 8.3: (a) Schematic illustration of combining the patterned growth of 2D PtTe<sub>2</sub> layers with the water-assisted integration of 3D PtS membranes on arbitrary substrates. (b) Camera image of a PtTe<sub>2</sub>/PtS hetero-material integrated on a PI substrate. The scale bar is 1 cm. (c) Graph of intensity-dependent temporal photo-responsiveness obtained from the sample in (b) at 625 nm wavelength at a bias of 1 V. (d–f) Graphs representing intensity-dependent temporal photo-responsiveness obtained at 940 nm wavelength from various hetero-junctions; (d) PtTe<sub>2</sub>-PtS-PtTe<sub>2</sub>, (e) Au-PtS-Au, (f) PtTe<sub>2</sub>-PtS, respectively. The scale bars in the inset images are 0.5 cm. (g) Plot of responsivity versus intensity obtained from a PtTe<sub>2</sub>/PtS/PtTe<sub>2</sub> sample. Adapted with permission from reference [11].

Figure 8.3 presents the photo-responsiveness obtained from the water-assisted vdW assembly of

large-area membrane materials, demonstrating the controllability and patternability of this integration approach. In Figure 8.3 a, an array of 2D  $\text{PtTe}_2$  layers is directly grown on a PI substrate by a patterned deposition of Pt strips followed by their CVD reaction with tellurium powder at 400 °C. Subsequently, a PtS membrane prepared by the water-assisted delamination method is then integrated onto the substrate, which yields a large-area patterned array of  $\text{PtTe}_2/\text{PtS}$  junctions. A representative image of a patterned array of  $\text{PtTe}_2/\text{PtS}$  hetero-materials integrated on a PI substrate is shown in Figure 8.3 b. The yellow square denotes the PtS integrated region whereas the grey lines are the directly grown array of  $\text{PtTe}_2$ . In this sample geometry, the semiconducting 3D PtS membrane with a bandgap of 1.24 eV is directly interfaced with metallic 2D  $\text{PtTe}_2$  layers which can function as electrodes.

Opto-electrical properties of the corresponding sample were characterized to evaluate functionalities of each constituent component. Figure 8.3 c represents plots of temporal photo-responsiveness obtained from the sample in Figure 8.3 b, with varying illumination intensity at a wavelength of 625 nm and a bias of 1 V. A significant increase of photocurrent is observed with increasing illumination intensity, indicating that the 3D PtS membrane functions as a photo-responsive active layer. We then explored a selection of vdW-assembled 2D/3D hetero-materials enabled by the intrinsic versatility of this combined approach, patterned growth and water-assisted integration. Figure 8.3 d–f present three different types of vdW hetero-materials integrated on flexible PI substrates, that is, symmetric junctions of  $\text{PtTe}_2\text{-PtS-PtTe}_2$  (Figure 8.3 d) and  $\text{Au-PtS-Au}$  (Figure 8.3 e) as well as an asymmetric junction of  $\text{PtTe}_2\text{-PtS}$  (Figure 8.3 f). The plots of photo-responsive characteristics corresponding to the images in the inset were obtained in NIR spectrum regime of 940 nm wavelength.

All samples exhibit strong intensity-dependent photocurrents, confirming that the integrated  $\text{PtTe}_2$  layers and PtS membranes well preserved their intrinsic metallic and semiconducting properties, respectively. Particularly, the comparison between  $\text{PtS/PtTe}_2$  (Figure 8.3 d) versus  $\text{PtS/Au}$  (Fig-

ure 8.3 e) shows similar photo-responsive characteristics, indicating that the vdW integrated 2D PtTe<sub>2</sub> layers well function as electrodes comparable to Au despite their much smaller thickness, that is,  $\approx 10$  nm for 2D PtTe<sub>2</sub> layers versus  $\approx 100$  nm for Au. Figure 8.3 g presents a plot of responsivity versus illumination intensity for the PtTe<sub>2</sub>-PtS-PtTe<sub>2</sub> sample obtained at wavelengths of 625 and 940 nm, respectively. The responsivity, R, is defined as  $|I_{ph}| \times P_{in}^{-1}$  where  $I_{ph}$  and  $P_{in}$  are photocurrent and incident optical power, respectively. It represents the photocurrent per unit incident optical power and functions as an important figure of merit to quantize the sensitivity of a photodetector.[7, 181] The obtained responsivity values are in the range of 6–9  $\mu\text{A/W}$  irrespective of illumination wavelength and intensity. They are comparable to those previously observed with small-sized ( $<100 \mu\text{m}^2$ ) 2D TMD flakes with two-terminal device measurement conditions,[34] while the lateral dimension ( $>\text{cm}^2$ ) of our samples is significantly larger. It is worth noting that our devices exhibit added advantages of large active area and high mechanical bendability.

### *Opto-Mechanical Performance*

It is known that vdW-interfaced contacts can efficiently accommodate an exertion of mechanical slips between active layers by releasing associated strains,[3] rendering high suitability for flexible electronic devices undergoing severe mechanical deformation.[182, 183] Having established the reliable vdW integration of PtTe<sub>2</sub>/PtS membranes on various substrates, we evaluated their feasibility for high-performance photo-detectors with mechanical flexibility and reversibility. Figure 8.4 presents the bending performance of the vdW assembled PtTe<sub>2</sub>-PtS-PtTe<sub>2</sub> sample on a PI substrate. Figure 8.4 a presents camera images of the sample undergoing a lateral bending of controlled bending radius ( $R_a$ ), that is, 11.8-6.1 mm. Figure 8.4 b–d presents plots of temporal photo-responsiveness obtained from the same sample in Figure 8.4 a under varying  $R_a$ . Intensity-dependent periodic photocurrents are observed, indicating that the sample is highly responsive to optical illumination (625 nm wavelength) even with a significant increase of lateral bending. Fig-

ure 8.4 e shows a comprehensive plot of photocurrent versus bending radius for the same sample tested in a bending radius range of 11.8–6.1 mm. The photocurrent steadily increases with increasing bending radius while its intensity dependency is well maintained even up to a small bending radius of 6.1 mm.

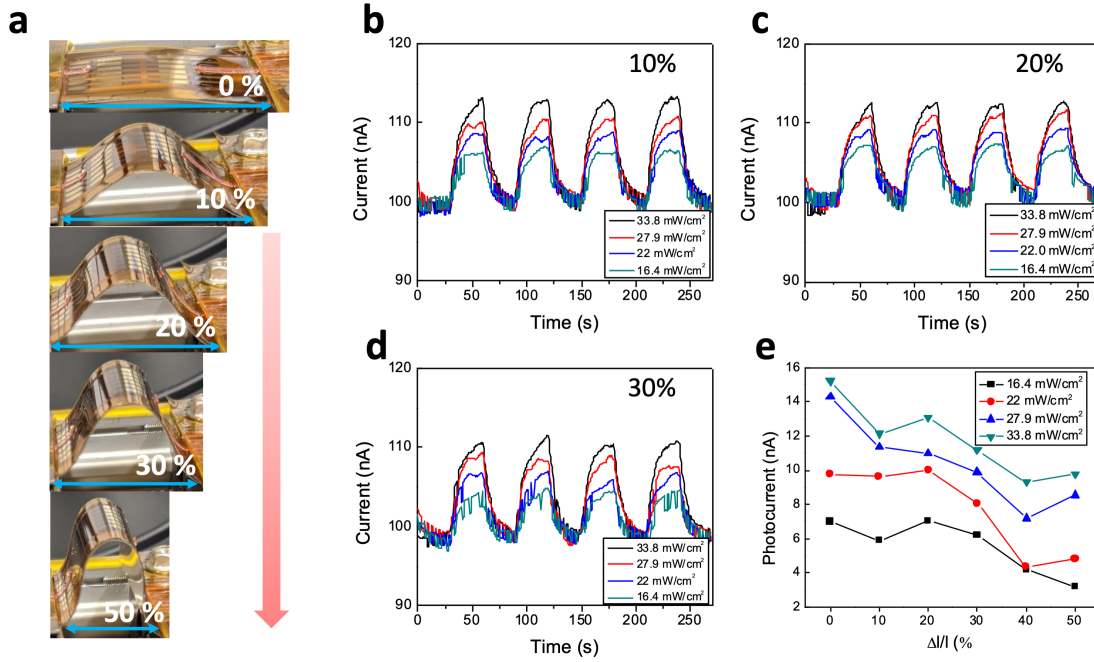


Figure 8.4: (a) Camera images of a PtTe<sub>2</sub>/PtS/PtTe<sub>2</sub> sample undergoing a string of bending degrees with varying bending radius ( $R_a$ ). (b–d) Graphs of intensity-dependent current versus time obtained from the sample in (a) at various bending radii; (b) 11.8, (c) 9.9, and (d) 8.9 mm at a bias of 1 V. (e) Plot of photocurrent versus radius of bending, with varying illumination intensity obtained at 625 nm wavelength, at a bias of 1 V. Adapted with permission from reference [11].

The mechanical endurance of the vdW-assembled photo-responsive materials was identified with another sample by repeatedly applying bending/unbending cycles, as presented in Figure 8.5. Figure 8.5 a shows plots of temporal photo-responsiveness obtained from the sample in a bending radius range of 12.0–9.0 mm, revealing well-resolved periodic photocurrents. These results combined with those in Figure 8.4 c,d confirm that PtTe<sub>2</sub>/PtS junctions of different forms enabled by the vdW assembly approach are highly attractive for mechanically flexible photo-detectors responsive

to a wide spectral range, that is, visible-to-NIR spectrum ranging from 625 to 940 nm. Last, the sample was tested under a cyclically applied deformation, that is, a reversible reduction/expansion of the original length up to a bending radius of 9.0 mm for a large number of cycles. Figure 8.5 b shows that the same sample subjected to different cycle numbers, 10, 100, and 400 present very similar photocurrents and light intensity-dependent characteristics. Figure 8.5 c compares plots of photocurrent versus light intensity for the three different cycle numbers, showing nearly identical trends.

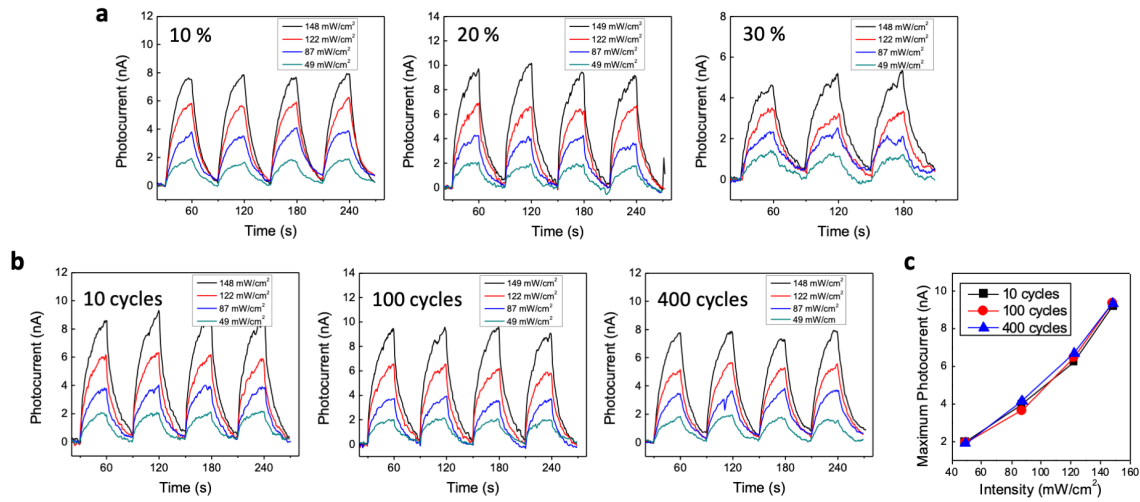


Figure 8.5: (a) Plots of intensity-dependent temporal photo-responsiveness under various bending radii at 940 nm illumination. (b) Plots of intensity-dependent temporal photo-responsiveness obtained from an identical sample subjected to reversible bending/unbending for 10, 100, and 400 cycles. (c) Comparison of maximum photocurrent versus intensity for three different bending cycles. Adapted with permission from reference [11].

## Conclusion

In summary, we developed a new vdW assembly approach to integrate near atom thickness optoelectronic materials of functionally and dimensionally distinct components on a large area. 2D

PtTe<sub>2</sub> and 3D PtS layers were deterministically integrated onto flexible substrates creating 2D/3D metallic/semiconducting junctions via a water-assisted delamination method. These hetero-materials exhibited well-preserved opto-electrical and mechanical characteristics of individual constituents. As a result, they presented highly unique mechanically resilient photodetection in a spectral range of visible-to-NIR wavelength. The vdW assembly approach unveiled in this study is believed to be extendable toward developing various unconventional devices based on near atom thickness materials in layered or non-layered structures.

## CHAPTER 9: SUMMARY AND FUTURE PERSPECTIVES

### Summary

In this dissertation, we have explored the intrinsic property advantages of Pt-based dichalcogenides for photo-sensitive applications. We made a significant contribution in developing Pt-based dichalcogenides integration with CMOS technology, owing to the low-synthesis temperature. We also made significant progress in developing novel manufacturing techniques enabling futuristic applications.

The main conclusions are presented in the following categories: 1. Pt-based dichalcogenides with exceptional material, electrical, and optical property have been developed, making them promising candidates for integration with silicon-based optoelectronics and also unconventional flexible optoelectronics. They have electronic, optical, and chemical property that make them suitable for applications where graphene or BP are unsuccessful.

2. To realize large-area devices optoelectronic devices, it is fundamental to study the integration of 2D TMDs on unconventional substrates (e.g., polymer-based) and hetero-assembly of nano-membranes of both layered 2D TMDs and non-layered materials. Large-area hetero-materials can achieve unconventional band structure without having lattice matching constraints presented by epitaxial methods. To achieve this, we used thermally assisted conversion method to obtain large-area 2D TMDs and 3D PtS and we developed a green water-assisted delamination and deterministic mechanical scooping method to create large-area hetero-materials without needing additional polymer or toxic chemicals.

3. We developed post-growth tuning method to transform specified regions in Pt-based dichalcogenides from semiconducting to metallic, promising several exciting applications in electronics.

Overall, the dissertation study suggests that Pt-based dichalcogenides are promising alternatives to graphene and BP in photo-sensitive applications. Our studies pave the way for the commercial realization of Pt-based dichalcogenides in silicon technology. Our study will also bring forth a new era in manufacturing using nano-membranes as building lego-blocks without additional lattice matching requirement.

### Future Perspectives

Despite the advantages posed by unusual electrical and optical properties of Pt-based dichalcogenides, there are still significant challenges that need to be addressed for the commercial realization of Pt-based dichalcogenides in optoelectronics. For example, synthesizing large-area Pt-based dichalcogenides with controllable structural and electrical properties remains a significant challenge. The most prominent direction with TMDs, including Pt-based dichalcogenides, is to synthesize the materials with atomic-level precision. Given that the electrical/optical properties of these materials are very strongly correlated to number of layers and defects as established in this thesis, it will be critical to control these material aspects. In addition to large-area high-quality synthesis with atomic-level precision, the ability to control the electronic property of the material post-synthesis will further extend the promise of these materials in electronic devices. The cutting edge direction with 2D TMDs is to form atomically thin circuits with the individual components all being of atomically thin dimensions. This idea can be truly realized if we can achieve controllable doping routes and precisely control the defect density. We need to find sophisticated techniques to control the material properties of these atomically thin materials.

Another distinguishable advantage of 2D TMDs is their lack of dangling bonds. Due to this property, there can be several heterostructures made from 2D TMDs. There is a vast library of 2D TMDs with various electronic properties, so many different heterostructures can be formed. For

example, metallic Pt-based dichalcogenides can be integrated with semiconducting 2D TMDs to form a Schottky junction of atomically thin form. Also, the water-assisted van der Waals assembly technique promises a novel technique for manufacturing electronic devices. Researchers need to expand the library of 2D TMDs that can currently be transferred in this method. For example, water-assisted transfer of  $\text{PtTe}_2$  is still very challenging. Various techniques to engineer the surface of the growth wafer are being studied to address this problem. Another major challenge with this van der Waals assembly technique is precisely aligning these materials. Researchers need to work on precisely transferring these materials to the location where they are desired, without having to use a polymer. Finally, there is immense potential with these Pt-based dichalcogenides for long-wavelength sensing due to the lack of need to cool these devices. The exact mechanism for sensing in very long-wavelengths with Pt-based dichalcogenides is still unknown. It will be essential to determine the exact mechanisms by which these materials respond to long wavelengths to increase their reliability in environmental applications.

## **APPENDIX : COPYRIGHT PERMISSIONS**

## The copyright permission for Figure 1.1

The chemistry of two-dimensional layered transition metal dichalcogenide nanosheets

Author: Manish Chhowalla et al  
Publication: Nature Chemistry  
Publisher: Springer Nature  
Date: Mar 20, 2013

Copyright © 2013, Nature Publishing Group, a division of Macmillan Publishers Limited. All Rights Reserved.

**Order Completed**

Thank you for your order.

This Agreement between University of Central Florida – Mashyat Sumaiya Shawkat ("You") and Springer Nature ("Springer Nature") consists of your license details and the terms and conditions provided by Springer Nature and Copyright Clearance Center.

Your confirmation email will contain your order number for future reference.

License Number 5181681075414 [Printable Details](#)

License date Nov 03, 2021

**Licensed Content**

Licensed Content Publisher Springer Nature  
Nature Chemistry  
Licensed Content Title The chemistry of two-dimensional layered transition metal dichalcogenide nanosheets  
Licensed Content Author Manish Chhowalla et al  
Licensed Content Date Mar 20, 2013

**Order Details**

Type of Use Thesis/Dissertation  
Requestor type academic/university or research institute  
Format print and electronic  
Portion figures/tables/illustrations  
Number of figures/tables/illustrations 1  
High-res required no  
Will you be translating? no  
Circulation/distribution 50000 or greater  
Author of this Springer Nature content no

**About Your Work**

Title ATOMICALLY THIN PLATINUM-BASED DICHALCOGENIDE MATERIALS FOR MULTIFUNCTIONAL PHOTO-SENSITIVE APPLICATIONS  
Institution name University of Central Florida  
Expected presentation date Jan 2022

**Requestor Location**

University of Central Florida  
4000 Central Florida Blvd

**Requestor Location**

ORLANDO, FL 32816  
United States  
Attn: University of Central Florida

**Additional Data**

Portions Figure 1

**Tax Details**


**Price**

Total 0.00 USD

Total: 0.00 USD

[CLOSE WINDOW](#) [ORDER MORE](#)

## The copyright permission for Figure 1.2

Emerging Photoluminescence in Monolayer MoS<sub>2</sub>  
Author: Andrea Splendiani, Liang Sun, Yuanbo Zhang, et al  
Publication: Nano Letters  
Publisher: American Chemical Society  
Date: Apr 1, 2010  
Copyright © 2010, American Chemical Society

**PERMISSION/LICENSE IS GRANTED FOR YOUR ORDER AT NO CHARGE**

This type of permission/license, instead of the standard Terms and Conditions, is sent to you because no fee is being charged for your order. Please note the following:

- Permission is granted for your request in both print and electronic formats, and translations.
- If figures and/or tables were requested, they may be adapted or used in part.
- Please print this page for your records and send a copy of it to your publisher/graduate school.
- Appropriate credit for the requested material should be given as follows: "Reprinted (adapted) with permission from (COMPLETE REFERENCE CITATION). Copyright (YEAR) American Chemical Society." Insert appropriate information in place of the capitalized words.
- One-time permission is granted only for the use specified in your RightsLink request. No additional uses are granted (such as derivative works or other editions). For any uses, please submit a new request.

If credit is given to another source for the material you requested from RightsLink, permission must be obtained from that source.

[BACK](#)[CLOSE WINDOW](#)

The copyright permission for Figure 1.3



## Attribution 4.0 International (CC BY 4.0)

This is a human-readable summary of (and not a substitute for) the [license](#). [Disclaimer](#).

### You are free to:

**Share** — copy and redistribute the material in any medium or format


**Adapt** — remix, transform, and build upon the material for any purpose, even commercially.

The licensor cannot revoke these freedoms as long as you follow the license terms.



---

### Under the following terms:



**Attribution** — You must give [appropriate credit](#), provide a link to the license, and [indicate if changes were made](#). You may do so in any reasonable manner, but not in any way that suggests the licensor endorses you or your use.

**No additional restrictions** — You may not apply legal terms or [technological measures](#) that legally restrict others from doing anything the license permits.

The copyright permission for Figure 1.4

CCC RightsLink<sup>®</sup>

Home

Help

Live Chat

Mashiyat Sumaiya Shawkat

Recent Progress on 2D Noble-Transition-Metal Dichalcogenides

Author: Liqing Pi, Liang Li, Kailing Liu, et al

Publisher: Advanced Functional Materials

Publisher: John Wiley and Sons

Date: Oct 3, 2019

© 2019 WILEY-VCH Verlag GmbH & Co. KGaA, Weinheim

Order Completed

Thank you for your order.

This Agreement between University of Central Florida – Mashiyat Sumaiya Shawkat ("You") and John Wiley and Sons ("John Wiley and Sons") consists of your license details and the terms and conditions provided by John Wiley and Sons and Copyright Clearance Center.

Your confirmation email will contain your order number for future reference.

License Number

5184331143685

License date

Nov 08, 2021

Order Details

Type of use

Dissertation/Thesis

Requester type

University/Academic

Format

Print and electronic

Portion

Figure/table

Number of figures/tables

1

Will you be translating?

No

Licensed Content

Licensed Content Publisher

John Wiley and Sons

Licensed Content Publication

Advanced Functional Materials

Licensed Content Title

Recent Progress on 2D Noble-Transition-Metal Dichalcogenides

Licensed Content Author

Liqing Pi, Liang Li, Kailing Liu, et al

Licensed Content Date

Oct 3, 2019

Licensed Content Volume

29

Licensed Content Issue

51

Licensed Content Pages

22

About Your Work

Title

ATOMICALLY THIN PLATINUM-BASED DICHALCOGENIDE MATERIALS FOR MULTIFUNCTIONAL PHOTO-SENSITIVE APPLICATIONS

Institution name

University of Central Florida

Expected presentation date

Jan 2022

Requester Location

University of Central Florida

4000 Central Florida Blvd

Requester Location

ORLANDO, FL 32816

United States

Attn: University of Central Florida

Additional Data

Portions

Figure 7

Tax Details

Publisher Tax ID

EUR26007151

Price

Total

0.00 USD

Would you like to purchase the full text of this article? If so, please continue on to the content ordering system located here: [Purchase PDF](#)

If you click on the buttons below or close this window, you will not be able to return to the content ordering system.


Close Window

Total: 0.00 USD

Order More

97

## The copyright permission for Figures 2.2 and 2.4

 **RightsLink®**

[Home](#) [Help](#) [Email Support](#) [Sign in](#) [Create Account](#)

**Wafer-Scale Growth of 2D PtTe<sub>2</sub> with Layer Orientation Tunable High Electrical Conductivity and Superior Hydrophobicity**

**Author:** Mengjing Wang, Tae-Jun Ko, Mashiyat Sumaiya Shawkat, et al  
**Publication:** Applied Materials  
**Publisher:** American Chemical Society  
**Date:** Mar 1, 2020

Copyright © 2020, American Chemical Society

**PERMISSION/LICENSE IS GRANTED FOR YOUR ORDER AT NO CHARGE**


This type of permission/license, instead of the standard Terms and Conditions, is sent to you because no fee is being charged for your order. Please note the following:

- Permission is granted for your request in both print and electronic formats, and translations.
- If figures and/or tables were requested, they may be adapted or used in part.
- Please print this page for your records and send a copy of it to your publisher/graduate school.
- Appropriate credit for the requested material should be given as follows: "Reprinted (adapted) with permission from (COMPLETE REFERENCE CITATION). Copyright (YEAR) American Chemical Society." Insert appropriate information in place of the capitalized words.
- One-time permission is granted only for the use specified in your RightsLink request. No additional uses are granted (such as derivative works or other editions). For any uses, please submit a new request.

If credit is given to another source for the material you requested from RightsLink, permission must be obtained from that source.

[BACK](#) [CLOSE WINDOW](#)

## The copyright permission for Figures 2.3, 3.2, and 5.1-5.3



ACS Publications  
Most Trusted. Most Cited. Most Read.

**Two-Dimensional/Three-Dimensional Schottky Junction Photovoltaic Devices Realized by the Direct CVD Growth of vdW 2D PtSe<sub>2</sub> Layers on Silicon**

**Author:** Mashiyat Sumaiya Shawkat, Hee-Suk Chung, Durjoy Dev, et al

**Publication:** Applied Materials

**Publisher:** American Chemical Society

**Date:** Jul 1, 2019

*Copyright © 2019, American Chemical Society*

**PERMISSION/LICENSE IS GRANTED FOR YOUR ORDER AT NO CHARGE**

This type of permission/license, instead of the standard Terms and Conditions, is sent to you because no fee is being charged for your order. Please note the following:

- Permission is granted for your request in both print and electronic formats, and translations.
- If figures and/or tables were requested, they may be adapted or used in part.
- Please print this page for your records and send a copy of it to your publisher/graduate school.
- Appropriate credit for the requested material should be given as follows: "Reprinted (adapted) with permission from (COMPLETE REFERENCE CITATION). Copyright (YEAR) American Chemical Society." Insert appropriate information in place of the capitalized words.
- One-time permission is granted only for the use specified in your RightsLink request. No additional uses are granted (such as derivative works or other editions). For any uses, please submit a new request.

If credit is given to another source for the material you requested from RightsLink, permission must be obtained from that source.

[BACK](#)[CLOSE WINDOW](#)

The copyright permission for Figures 3.1, 3.3, and 6.1-6.5

**Large-area 2D PtTe<sub>2</sub>/silicon vertical-junction devices with ultrafast and high-sensitivity photodetection and photovoltaic enhancement by integrating water droplets**

M. S. Shawkat, T. A. Chowdhury, H. Chung, S. Sattar, T. Ko, J. A. Larsson and Y. Jung, *Nanoscale*, 2020, **12**, 23116 DOI: 10.1039/D0NR05670G

To request permission to reproduce material from this article, please go to the [Copyright Clearance Center request page](#).

If you are **an author contributing to an RSC publication**, **you do not need to request permission** provided correct acknowledgement is given.

If you are **the author of this article**, **you do not need to request permission to reproduce figures and diagrams** provided correct acknowledgement is given. If you want to reproduce the whole article in a third-party publication (excluding your thesis/dissertation for which permission is not required) please go to the [Copyright Clearance Center request page](#).

Read more about [how to correctly acknowledge RSC content](#).

## The copyright permission for Figures 3.3 and 7.1-7.4



**ACS Publications**  
Most Trusted. Most Cited. Most Read.

**Scalable Van der Waals Two-Dimensional PtTe<sub>2</sub> Layers Integrated onto Silicon for Efficient Near-to-Mid Infrared Photodetection**

**Author:** Mashiyat Sumaiya Shawkat, Shihab Bin Hafiz, Molla Manjurul Islam, et al  
**Publication:** Applied Materials  
**Publisher:** American Chemical Society  
**Date:** Apr 1, 2021

Copyright © 2021, American Chemical Society

**PERMISSION/LICENSE IS GRANTED FOR YOUR ORDER AT NO CHARGE**


This type of permission/license, instead of the standard Terms and Conditions, is sent to you because no fee is being charged for your order. Please note the following:

- Permission is granted for your request in both print and electronic formats, and translations.
- If figures and/or tables were requested, they may be adapted or used in part.
- Please print this page for your records and send a copy of it to your publisher/graduate school.
- Appropriate credit for the requested material should be given as follows: "Reprinted (adapted) with permission from {COMPLETE REFERENCE CITATION}. Copyright {YEAR} American Chemical Society." Insert appropriate information in place of the capitalized words.
- One-time permission is granted only for the use specified in your RightsLink request. No additional uses are granted (such as derivative works or other editions). For any uses, please submit a new request.

If credit is given to another source for the material you requested from RightsLink, permission must be obtained from that source.

[BACK](#)[CLOSE WINDOW](#)

## The copyright permission for Figures 4.1-4.5



Most Trusted. Most Cited. Most Read.

**Thickness-Independent Semiconducting-to-Metallic Conversion in Wafer-Scale Two-Dimensional PtSe<sub>2</sub> Layers by Plasma-Driven Chalcogen Defect Engineering**

**Author:** Mashiyat Sumaiya Shawkat, Jaeyoung Gil, Sang Sub Han, et al

**Publication:** Applied Materials

**Publisher:** American Chemical Society

**Date:** Mar 1, 2020

*Copyright © 2020, American Chemical Society*

**PERMISSION/LICENSE IS GRANTED FOR YOUR ORDER AT NO CHARGE**


This type of permission/license, instead of the standard Terms and Conditions, is sent to you because no fee is being charged for your order. Please note the following:

- Permission is granted for your request in both print and electronic formats, and translations.
- If figures and/or tables were requested, they may be adapted or used in part.
- Please print this page for your records and send a copy of it to your publisher/graduate school.
- Appropriate credit for the requested material should be given as follows: "Reprinted (adapted) with permission from {COMPLETE REFERENCE CITATION}. Copyright {YEAR} American Chemical Society." Insert appropriate information in place of the capitalized words.
- One-time permission is granted only for the use specified in your RightsLink request. No additional uses are granted (such as derivative works or other editions). For any uses, please submit a new request.

If credit is given to another source for the material you requested from RightsLink, permission must be obtained from that source.

[BACK](#)[CLOSE WINDOW](#)

## The copyright permission for Figure 8.1



### Attribution 4.0 International (CC BY 4.0)


This is a human-readable summary of (and not a substitute for) the [license](#). [Disclaimer](#).

#### You are free to:


**Share** — copy and redistribute the material in any medium or format

**Adapt** — remix, transform, and build upon the material for any purpose, even commercially.

The licensor cannot revoke these freedoms as long as you follow the license terms.



#### Under the following terms:

 **Attribution** — You must give [appropriate credit](#), provide a link to the license, and [indicate if changes were made](#). You may do so in any reasonable manner, but not in any way that suggests the licensor endorses you or your use.


**No additional restrictions** — You may not apply legal terms or [technological measures](#) that legally restrict others from doing anything the license permits.

#### Notices:


You do not have to comply with the license for elements of the material in the public domain or where your use is permitted by an applicable [exception or limitation](#).

No warranties are given. The license may not give you all of the permissions necessary for your intended use. For example, other rights such as [publicity, privacy, or moral rights](#) may limit how you use the material.

## The copyright permissions for Figure 8.2



[Home](#)
[Help](#)
[Email Support](#)
Mashiyat Sumaiya Shawkat



**Wafer-Scale Van der Waals Assembly of Free-Standing Near Atom Thickness Hetero-Membranes for Flexible Photo-Detectors**  
 Author: Mashiyat Sumaiya Shawkat, Sang Sub Han, Hee-Suk Chung, et al  
 Publication: Advanced Electronic Materials  
 Publisher: John Wiley and Sons  
 Date: Jun 21, 2021  
 © 2021 Wiley-VCH GmbH

### Order Completed

Thank you for your order.

This Agreement between University of Central Florida -- Mashiyat Sumaiya Shawkat ("You") and John Wiley and Sons ("John Wiley and Sons") consists of your license details and the terms and conditions provided by John Wiley and Sons and Copyright Clearance Center.

Your confirmation email will contain your order number for future reference.

License Number 5172770414930 [Printable Details](#)

License date Oct 19, 2021

[Licensed Content](#)

Licensed Content Publisher	John Wiley and Sons	Type of use	Dissertation/Thesis
Licensed Content Publication	Advanced Electronic Materials	Requestor type	Author of this Wiley article
Licensed Content Title	Wafer-Scale Van der Waals Assembly of Free-Standing Near Atom Thickness Hetero-Membranes for Flexible Photo-Detectors	Format	Print and electronic
Licensed Content Author	Mashiyat Sumaiya Shawkat, Sang Sub Han, Hee-Suk Chung, et al	Portion	Full article
Licensed Content Date	Jun 21, 2021	Will you be translating?	No
Licensed Content Volume	7		
Licensed Content Issue	8		
Licensed Content Pages	8		

[Order Details](#)

[About Your Work](#)

Title	ATOMICALLY THIN PLATINUM-BASED DICHALCOGENIDE MATERIALS FOR MULTIFUNCTIONAL PHOTO-SENSITIVE APPLICATIONS
Institution name	University of Central Florida
Expected presentation date	Jan 2022

[Additional Data](#)

Order reference number	1
------------------------	---

[Requestor Location](#)

Requestor Location	University of Central Florida 4000 Central Florida Blvd  ORLANDO, FL 32816 United States Attn: University of Central Florida
--------------------	---

[Tax Details](#)

Publisher Tax ID	EU826007151
------------------	-------------

[Price](#)

Total	0.00 USD
-------	----------



## Attribution 4.0 International (CC BY 4.0)

This is a human-readable summary of (and not a substitute for) the [license](#). [Disclaimer](#).

### You are free to:

**Share** — copy and redistribute the material in any medium or format

**Adapt** — remix, transform, and build upon the material for any purpose, even commercially.

The licensor cannot revoke these freedoms as long as you follow the license terms.



### Under the following terms:



**Attribution** — You must give [appropriate credit](#), provide a link to the license, and [indicate if changes were made](#). You may do so in any reasonable manner, but not in any way that suggests the licensor endorses you or your use.

**No additional restrictions** — You may not apply legal terms or [technological measures](#) that legally restrict others from doing anything the license permits.

### Notices:

You do not have to comply with the license for elements of the material in the public domain or where your use is permitted by an applicable [exception or limitation](#).

No warranties are given. The license may not give you all of the permissions necessary for your intended use. For example, other rights such as [publicity, privacy, or moral rights](#) may limit how you use the material.

## The copyright permission for Figures 8.3- 8.5

### Order Completed

Thank you for your order.

This Agreement between University of Central Florida -- Mashiyat Sumaiya Shawkat ("You") and John Wiley and Sons ("John Wiley and Sons") consists of your license details and the terms and conditions provided by John Wiley and Sons and Copyright Clearance Center.

Your confirmation email will contain your order number for future reference.

License Number 5172770414930

[Printable Details](#)

License date Oct 19, 2021

#### Licensed Content

Licensed Content Publisher	John Wiley and Sons
Licensed Content Publication	Advanced Electronic Materials
Licensed Content Title	Wafer-Scale Van der Waals Assembly of Free-Standing Near Atom Thickness Hetero-Membranes for Flexible Photo-Detectors
Licensed Content Author	Mashiyat Sumaiya Shawkat, Sang Sub Han, Hee-Suk Chung, et al
Licensed Content Date	Jun 21, 2021
Licensed Content Volume	7
Licensed Content Issue	8
Licensed Content Pages	8

#### Order Details

Type of use	Dissertation/Thesis
Requestor type	Author of this Wiley article
Format	Print and electronic
Portion	Full article
Will you be translating?	No

## LIST OF REFERENCES

- [1] L. Pi, L. Li, K. Liu, Q. Zhang, H. Li, and T. Zhai, “Recent progress on 2d noble-transition-metal dichalcogenides,” *Advanced Functional Materials*, vol. 29, no. 51, p. 1904932, 2019.
- [2] G. R. Bhimanapati, Z. Lin, V. Meunier, Y. Jung, J. Cha, S. Das, D. Xiao, Y. Son, M. S. Strano, V. R. Cooper, L. Liang, S. G. Louie, E. Ringe, W. Zhou, S. S. Kim, R. R. Naik, B. G. Sumpter, H. Terrones, F. Xia, Y. Wang, J. Zhu, D. Akinwande, N. Alem, J. A. Schuller, R. E. Schaak, M. Terrones, and J. A. Robinson, “Recent advances in two-dimensional materials beyond graphene,” *ACS Nano*, vol. 9, no. 12, pp. 11509–11539, 2015.
- [3] M. Wang, H. Li, T.-J. Ko, M. Sumaiya Shawkat, E. Okogbue, C. Yoo, S. S. Han, M. A. Islam, K. H. Oh, Y. Jung, and et al., “Manufacturing strategies for wafer-scale two-dimensional transition metal dichalcogenide heterolayers,” *Journal of Materials Research*, vol. 35, no. 11, p. 1350–1368, 2020.
- [4] F. Bonaccorso, Z. Sun, T. Hasan, and A. Ferrari, “Graphene photonics and optoelectronics,” *Nature photonics*, vol. 4, no. 9, pp. 611–622, 2010.
- [5] M. J. Allen, V. C. Tung, and R. B. Kaner, “Honeycomb carbon: a review of graphene,” *Chemical reviews*, vol. 110, no. 1, pp. 132–145, 2010.
- [6] N. Choudhary, M. A. Islam, J. H. Kim, T.-J. Ko, A. Schropp, L. Hurtado, D. Weitzman, L. Zhai, and Y. Jung, “Two-dimensional transition metal dichalcogenide hybrid materials for energy applications,” *Nano Today*, vol. 19, pp. 16–40, 2018.
- [7] H. Li, X. Duan, X. Wu, X. Zhuang, H. Zhou, Q. Zhang, X. Zhu, W. Hu, P. Ren, P. Guo, *et al.*, “Growth of alloy  $\text{MoS}_2$  x  $\text{Se}_2$  (1-x) nanosheets with fully tunable chemical compositions and

- optical properties,” *Journal of the American Chemical Society*, vol. 136, no. 10, pp. 3756–3759, 2014.
- [8] X. Bao, Q. Ou, Z.-Q. Xu, Y. Zhang, Q. Bao, and H. Zhang, “Band structure engineering in 2d materials for optoelectronic applications,” *Advanced Materials Technologies*, vol. 3, no. 11, p. 1800072, 2018.
- [9] K. F. Mak, C. Lee, J. Hone, J. Shan, and T. F. Heinz, “Atomically thin mos2: a new direct-gap semiconductor,” *Physical review letters*, vol. 105, no. 13, p. 136805, 2010.
- [10] M. Chhowalla, H. S. Shin, G. Eda, L.-J. Li, K. P. Loh, and H. Zhang, “The chemistry of two-dimensional layered transition metal dichalcogenide nanosheets,” *Nature Chemistry*, vol. 5, no. 4, pp. 263–275, 2013.
- [11] C.-H. Lee, G.-H. Lee, A. M. van der Zande, W. Chen, Y. Li, M. Han, X. Cui, G. Arefe, C. Nuckolls, T. F. Heinz, J. Guo, J. Hone, and P. Kim, “Atomically thin p–n junctions with van der waals heterointerfaces,” *Nature Nanotechnology*, vol. 9, no. 9, pp. 676–681, 2014.
- [12] M. S. Shawkat, H.-S. Chung, D. Dev, S. Das, T. Roy, and Y. Jung, “Two-dimensional/three-dimensional schottky junction photovoltaic devices realized by the direct cvd growth of vdw 2d ptse2 layers on silicon,” *ACS Applied Materials Interfaces*, vol. 11, no. 30, pp. 27251–27258, 2019.
- [13] M. S. Shawkat, T. A. Chowdhury, H.-S. Chung, S. Sattar, T.-J. Ko, J. A. Larsson, and Y. Jung, “Large-area 2d ptte2/silicon vertical-junction devices with ultrafast and high-sensitivity photodetection and photovoltaic enhancement by integrating water droplets,” *Nanoscale*, vol. 12, no. 45, pp. 23116–23124, 2020.
- [14] A. Gupta, T. Sakthivel, and S. Seal, “Recent development in 2d materials beyond graphene,” *Progress in Materials Science*, vol. 73, pp. 44–126, 2015.

- [15] S. Manzeli, D. Ovchinnikov, D. Pasquier, O. V. Yazyev, and A. Kis, “2d transition metal dichalcogenides,” *Nature Reviews Materials*, vol. 2, no. 8, p. 17033, 2017.
- [16] K. F. Mak and J. Shan, “Photonics and optoelectronics of 2d semiconductor transition metal dichalcogenides,” *Nature Photonics*, vol. 10, no. 4, pp. 216–226, 2016.
- [17] D. Akinwande, N. Petrone, and J. Hone, “Two-dimensional flexible nanoelectronics,” *Nature Communications*, vol. 5, no. 1, p. 5678, 2014.
- [18] X. Chia, A. Y. S. Eng, A. Ambrosi, S. M. Tan, and M. Pumera, “Electrochemistry of nanostructured layered transition-metal dichalcogenides,” *Chemical Reviews*, vol. 115, no. 21, pp. 11941–11966, 2015.
- [19] D. Jariwala, V. K. Sangwan, L. J. Lauhon, T. J. Marks, and M. C. Hersam, “Emerging device applications for semiconducting two-dimensional transition metal dichalcogenides,” *ACS Nano*, vol. 8, no. 2, pp. 1102–1120, 2014.
- [20] T.-J. Ko, M. Wang, C. Yoo, E. Okogbue, M. A. Islam, H. Li, M. S. Shawkat, S. S. Han, K. H. Oh, and Y. Jung, “Large-area 2d tmd layers for mechanically reconfigurable electronic devices,” *J. Phys. D: Appl. Phys.*, vol. 53, no. 31, p. 313002, 2020.
- [21] Q. H. Wang, K. Kalantar-Zadeh, A. Kis, J. N. Coleman, and M. S. Strano, “Electronics and optoelectronics of two-dimensional transition metal dichalcogenides,” *Nature Nanotechnology*, vol. 7, no. 11, pp. 699–712, 2012.
- [22] G. Fiori, F. Bonaccorso, G. Iannaccone, T. Palacios, D. Neumaier, A. Seabaugh, S. K. Banerjee, and L. Colombo, “Electronics based on two-dimensional materials,” *Nature Nanotechnology*, vol. 9, no. 10, pp. 768–779, 2014.
- [23] H. Yu, M. Liao, W. Zhao, G. Liu, X. J. Zhou, Z. Wei, X. Xu, K. Liu, Z. Hu, K. Deng, S. Zhou, J.-A. Shi, L. Gu, C. Shen, T. Zhang, L. Du, L. Xie, J. Zhu, W. Chen, R. Yang,

- D. Shi, and G. Zhang, “Wafer-scale growth and transfer of highly-oriented monolayer mos<sub>2</sub> continuous films,” *ACS Nano*, vol. 11, no. 12, pp. 12001–12007, 2017.
- [24] K. Kang, S. Xie, L. Huang, Y. Han, P. Y. Huang, K. F. Mak, C.-J. Kim, D. Muller, and J. Park, “High-mobility three-atom-thick semiconducting films with wafer-scale homogeneity,” *Nature*, vol. 520, no. 7549, pp. 656–660, 2015.
- [25] A. Splendiani, L. Sun, Y. Zhang, T. Li, J. Kim, C.-Y. Chim, G. Galli, and F. Wang, “Emerging photoluminescence in monolayer mos<sub>2</sub>,” *Nano letters*, vol. 10, no. 4, pp. 1271–1275, 2010.
- [26] X. Ling, H. Wang, S. Huang, F. Xia, and M. S. Dresselhaus, “The renaissance of black phosphorus,” *Proceedings of the National Academy of Sciences*, vol. 112, no. 15, pp. 4523–4530, 2015.
- [27] Q. Zhou, Q. Chen, Y. Tong, and J. Wang, “Light-induced ambient degradation of few-layer black phosphorus: Mechanism and protection,” *Angewandte Chemie International Edition*, vol. 55, no. 38, pp. 11437–11441, 2016.
- [28] Y. Xu, Z. Shi, X. Shi, K. Zhang, and H. Zhang, “Recent progress in black phosphorus and black-phosphorus-analogue materials: properties, synthesis and applications,” *Nanoscale*, vol. 11, no. 31, pp. 14491–14527, 2019.
- [29] G. Y. Guo and W. Y. Liang, “The electronic structures of platinum dichalcogenides: Pts<sub>2</sub>, ptse<sub>2</sub> and ptte<sub>2</sub>,” *Journal of Physics C: Solid State Physics*, vol. 19, no. 7, pp. 995–1008, 1986.
- [30] A. Ciarrocchi, A. Avsar, D. Ovchinnikov, and A. Kis, “Thickness-modulated metal-to-semiconductor transformation in a transition metal dichalcogenide,” *Nature Communications*, vol. 9, no. 1, p. 919, 2018.

- [31] W. Yao, E. Wang, H. Huang, K. Deng, M. Yan, K. Zhang, K. Miyamoto, T. Okuda, L. Li, Y. Wang, H. Gao, C. Liu, W. Duan, and S. Zhou, “Direct observation of spin-layer locking by local rashba effect in monolayer semiconducting ptse2 film,” *Nature Communications*, vol. 8, no. 1, p. 14216, 2017.
- [32] M. Wang, T.-J. Ko, M. S. Shawkat, S. S. Han, E. Okogbue, H.-S. Chung, T.-S. Bae, S. Sattar, J. Gil, C. Noh, K. H. Oh, Y. Jung, J. A. Larsson, and Y. Jung, “Wafer-scale growth of 2d ptte2 with layer orientation tunable high electrical conductivity and superior hydrophobicity,” *ACS Applied Materials Interfaces*, vol. 12, no. 9, pp. 10839–10851, 2020.
- [33] X. Lin, J. Lu, Y. Shao, Y. Zhang, X. Wu, J. Pan, L. Gao, S. Zhu, K. Qian, Y. Zhang, *et al.*, “Intrinsically patterned two-dimensional materials for selective adsorption of molecules and nanoclusters,” *Nature materials*, vol. 16, no. 7, pp. 717–721, 2017.
- [34] P. Li, L. Li, and X. C. Zeng, “Tuning the electronic properties of monolayer and bilayer ptse 2 via strain engineering,” *Journal of Materials Chemistry C*, vol. 4, no. 15, pp. 3106–3112, 2016.
- [35] S. Lin, Y. Liu, Z. Hu, W. Lu, C. H. Mak, L. Zeng, J. Zhao, Y. Li, F. Yan, Y. H. Tsang, *et al.*, “Tunable active edge sites in ptse2 films towards hydrogen evolution reaction,” *Nano Energy*, vol. 42, pp. 26–33, 2017.
- [36] Y. Zhao, J. Qiao, Z. Yu, P. Yu, K. Xu, S. P. Lau, W. Zhou, Z. Liu, X. Wang, W. Ji, and Y. Chai, “High-electron-mobility and air-stable 2d layered ptse2 fets,” *Advanced Materials*, vol. 29, no. 5, p. 1604230, 2017.
- [37] W. Zhang, Z. Huang, W. Zhang, and Y. Li, “Two-dimensional semiconductors with possible high room temperature mobility,” *Nano Research*, vol. 7, no. 12, pp. 1731–1737, 2014.

- [38] X. Yu, P. Yu, D. Wu, B. Singh, Q. Zeng, H. Lin, W. Zhou, J. Lin, K. Suenaga, Z. Liu, and Q. J. Wang, “Atomically thin noble metal dichalcogenide: a broadband mid-infrared semiconductor,” *Nature Communications*, vol. 9, no. 1, p. 1545, 2018.
- [39] J. D. Wood, S. A. Wells, D. Jariwala, K.-S. Chen, E. Cho, V. K. Sangwan, X. Liu, L. J. Lauhon, T. J. Marks, and M. C. Hersam, “Effective passivation of exfoliated black phosphorus transistors against ambient degradation,” *Nano Letters*, vol. 14, no. 12, pp. 6964–6970, 2014.
- [40] S. S. Han, J. H. Kim, C. Noh, J. H. Kim, E. Ji, J. Kwon, S. M. Yu, T.-J. Ko, E. Okogbue, K. H. Oh, H.-S. Chung, Y. Jung, G.-H. Lee, and Y. Jung, “Horizontal-to-vertical transition of 2d layer orientation in low-temperature chemical vapor deposition-grown ptse2 and its influences on electrical properties and device applications,” *ACS Applied Materials Interfaces*, vol. 11, no. 14, pp. 13598–13607, 2019.
- [41] L. Fu, D. Hu, R. G. Mendes, M. H. Rmmeli, Q. Dai, B. Wu, L. Fu, and Y. Liu, “Highly organized epitaxy of dirac semimetallic ptte2 crystals with extrahigh conductivity and visible surface plasmons at edges,” *ACS Nano*, vol. 12, no. 9, pp. 9405–9411, 2018.
- [42] H. Ma, P. Chen, B. Li, J. Li, R. Ai, Z. Zhang, G. Sun, K. Yao, Z. Lin, B. Zhao, R. Wu, X. Tang, X. Duan, and X. Duan, “Thickness-tunable synthesis of ultrathin type-ii dirac semimetal ptte2 single crystals and their thickness-dependent electronic properties,” *Nano Letters*, vol. 18, no. 6, pp. 3523–3529, 2018.
- [43] E. Okogbue, T.-J. Ko, S. S. Han, M. S. Shawkat, M. Wang, H.-S. Chung, K. H. Oh, and Y. Jung, “Wafer-scale 2d ptte2 layers for high-efficiency mechanically flexible electro-thermal smart window applications,” *Nanoscale*, 2020.

- [44] D. Periyangounder, P. Gnanasekar, P. Varadhan, J.-H. He, and J. Kulandaivel, “High performance, self-powered photodetectors based on a graphene/silicon schottky junction diode,” *Journal of Materials Chemistry C*, vol. 6, no. 35, pp. 9545–9551, 2018.
- [45] G. Wang, Z. Wang, N. McEvoy, P. Fan, and W. J. Blau, “Layered ptse<sub>2</sub> for sensing, photonic, and (opto-) electronic applications,” *Advanced Materials*, vol. 33, no. 1, p. 2004070, 2021.
- [46] H. Xu, C. Guo, J. Zhang, W. Guo, C.-N. Kuo, C. S. Lue, W. Hu, L. Wang, G. Chen, A. Politano, *et al.*, “Ptte<sub>2</sub>-based type-ii dirac semimetal and its van der waals heterostructure for sensitive room temperature terahertz photodetection,” *Small*, vol. 15, no. 52, p. 1903362, 2019.
- [47] Y. Ma, X. Shao, J. Li, B. Dong, Z. Hu, Q. Zhou, H. Xu, X. Zhao, H. Fang, X. Li, *et al.*, “Electrochemically exfoliated platinum dichalcogenide atomic layers for high-performance air-stable infrared photodetectors,” *ACS Applied Materials & Interfaces*, vol. 13, no. 7, pp. 8518–8527, 2021.
- [48] X. Chia, A. Adriano, P. Lazar, Z. Sofer, J. Luxa, and M. Pumera, “Layered platinum dichalcogenides (pts<sub>2</sub>, ptse<sub>2</sub>, and ptte<sub>2</sub>) electrocatalysis: Monotonic dependence on the chalcogen size,” *Advanced Functional Materials*, vol. 26, no. 24, pp. 4306–4318, 2016.
- [49] S. Hao, J. Zeng, T. Xu, X. Cong, C. Wang, C. Wu, Y. Wang, X. Liu, T. Cao, G. Su, L. Jia, Z. Wu, Q. Lin, L. Zhang, S. Yan, M. Guo, Z. Wang, P. Tan, L. Sun, Z. Ni, S.-J. Liang, X. Cui, and F. Miao, “Low-temperature eutectic synthesis of ptte<sub>2</sub> with weak antilocalization and controlled layer thinning,” *Advanced Functional Materials*, vol. 28, no. 36, p. 1803746, 2018.
- [50] Y. Jung, J. Shen, Y. Liu, J. M. Woods, Y. Sun, and J. J. Cha, “Metal seed layer thickness-induced transition from vertical to horizontal growth of mos<sub>2</sub> and ws<sub>2</sub>,” *Nano Letters*, vol. 14, no. 12, pp. 6842–6849, 2014.

- [51] M. G. Stanford, P. R. Pudasaini, A. Belianinov, N. Cross, J. H. Noh, M. R. Koehler, D. G. Mandrus, G. Duscher, A. J. Rondinone, I. N. Ivanov, T. Z. Ward, and P. D. Rack, “Focused helium-ion beam irradiation effects on electrical transport properties of few-layer wse<sub>2</sub>: enabling nanoscale direct write homo-junctions,” *Scientific Reports*, vol. 6, no. 1, p. 27276, 2016.
- [52] A. Politano, G. Chiarello, B. Ghosh, K. Sadhukhan, C.-N. Kuo, C. S. Lue, V. Pellegrini, and A. Agarwal, “3d dirac plasmons in the type-ii dirac semimetal ptte<sub>2</sub>,” *Phys. Rev. Lett.*, vol. 121, p. 086804, Aug 2018.
- [53] K. Deng, M. Yan, C.-P. Yu, J. Li, X. Zhou, K. Zhang, Y. Zhao, K. Miyamoto, T. Okuda, W. Duan, Y. Wu, X. Zhong, and S. Zhou, “Crossover from 2d metal to 3d dirac semimetal in metallic ptte<sub>2</sub> films with local rashba effect,” *Science Bulletin*, vol. 64, no. 15, pp. 1044–1048, 2019. Two-Dimensional Materials: New Opportunities for Electronics, Photonics and Optoelectronics.
- [54] D. Fu, X. Bo, F. Fei, B. Wu, M. Gao, X. Wang, M. Naveed, S. A. Shah, H. Bu, B. Wang, L. Cao, W. Zou, X. Wan, and F. Song, “Quantum oscillations in type-ii dirac semimetal ptte<sub>2</sub>,” *Phys. Rev. B*, vol. 97, p. 245109, Jun 2018.
- [55] N. Choudhary, H.-S. Chung, J. H. Kim, C. Noh, M. A. Islam, K. H. Oh, K. Coffey, Y. Jung, and Y. Jung, “Strain-driven and layer-number-dependent crossover of growth mode in van der waals heterostructures: 2d/2d layer-by-layer horizontal epitaxy to 2d/3d vertical reorientation,” *Advanced Materials Interfaces*, vol. 5, no. 14, p. 1800382, 2018.
- [56] R. A. B. Villaos, C. P. Crisostomo, Z.-Q. Huang, S.-M. Huang, A. A. B. Padama, M. A. Al-bao, H. Lin, and F.-C. Chuang, “Thickness dependent electronic properties of pt dichalcogenides,” *npj 2D Materials and Applications*, vol. 3, no. 1, p. 2, 2019.

- [57] Y. Yu, S.-Y. Huang, Y. Li, S. N. Steinmann, W. Yang, and L. Cao, "Layer-dependent electrocatalysis of mos2 for hydrogen evolution," *Nano letters*, vol. 14, no. 2, pp. 553–558, 2014.
- [58] E. Cappelluti, R. Roldán, J. Silva-Guillén, P. Ordejón, and F. Guinea, "Tight-binding model and direct-gap/indirect-gap transition in single-layer and multilayer mos 2," *Physical Review B*, vol. 88, no. 7, p. 075409, 2013.
- [59] Z. Zhang, J. Niu, P. Yang, Y. Gong, Q. Ji, J. Shi, Q. Fang, S. Jiang, H. Li, X. Zhou, *et al.*, "Van der waals epitaxial growth of 2d metallic vanadium diselenide single crystals and their extra-high electrical conductivity," *Advanced Materials*, vol. 29, no. 37, p. 1702359, 2017.
- [60] M. Motoyoshi, "Through-silicon via (tsv)," *Proceedings of the IEEE*, vol. 97, no. 1, pp. 43–48, 2009.
- [61] D. Jariwala, T. J. Marks, and M. C. Hersam, "Mixed-dimensional van der waals heterostructures," *Nature Mater*, vol. 16, no. 2, pp. 170–181, 2017.
- [62] S. Das, M. J. Hossain, S.-F. Leung, A. Lenox, Y. Jung, K. Davis, J.-H. He, and T. Roy, "A leaf-inspired photon management scheme using optically tuned bilayer nanoparticles for ultra-thin and highly efficient photovoltaic devices," *Nano Energy*, vol. 58, pp. 47–56, 2019.
- [63] C. Xie, P. Lv, B. Nie, J. Jie, X. Zhang, Z. Wang, P. Jiang, Z. Hu, L. Luo, Z. Zhu, L. Wang, and C. Wu, "Monolayer graphene film/silicon nanowire array schottky junction solar cells," *Applied Physics Letters*, vol. 99, no. 13, p. 133113, 2011.
- [64] X. Liu, X. W. Zhang, Z. G. Yin, J. H. Meng, H. L. Gao, L. Q. Zhang, Y. J. Zhao, and H. L. Wang, "Enhanced efficiency of graphene-silicon schottky junction solar cells by doping with au nanoparticles," *Applied Physics Letters*, vol. 105, no. 18, p. 183901, 2014.

- [65] X. Li, H. Zhu, K. Wang, A. Cao, J. Wei, C. Li, Y. Jia, Z. Li, X. Li, and D. Wu, “Graphene-on-silicon schottky junction solar cells,” *Advanced Materials*, vol. 22, no. 25, pp. 2743–2748, 2010.
- [66] C. Yim, K. Lee, N. McEvoy, M. O’Brien, S. Riazimehr, N. C. Berner, C. P. Cullen, J. Kotakoski, J. C. Meyer, M. C. Lemme, and G. S. Duesberg, “High-performance hybrid electronic devices from layered ptse2 films grown at low temperature,” *ACS Nano*, vol. 10, no. 10, pp. 9550–9558, 2016.
- [67] M. S. Shawkat, S. B. Hafiz, M. M. Islam, S. A. Mofid, M. M. Al Mahfuz, A. Biswas, H.-S. Chung, E. Okogbue, T.-J. Ko, D. Chanda, T. Roy, D.-K. Ko, and Y. Jung, “Scalable van der waals two-dimensional ptte2 layers integrated onto silicon for efficient near-to-mid infrared photodetection,” *ACS Appl. Mater. Interfaces*, vol. 13, no. 13, pp. 15542–15550, 2021.
- [68] A. Politano, G. Chiarello, C.-N. Kuo, C. S. Lue, R. Edla, P. Torelli, V. Pellegrini, and D. W. Boukhvalov, “Tailoring the surface chemical reactivity of transition-metal dichalcogenide ptte2 crystals,” *Advanced Functional Materials*, vol. 28, no. 15, p. 1706504, 2018.
- [69] S. Yang, H. Cai, B. Chen, C. Ko, V. O. Özçelik, D. F. Ogletree, C. E. White, Y. Shen, and S. Tongay, “Environmental stability of 2d anisotropic tellurium containing nanomaterials: anisotropic to isotropic transition,” *Nanoscale*, vol. 9, no. 34, pp. 12288–12294, 2017.
- [70] T.-Y. Su, H. Medina, Y.-Z. Chen, S.-W. Wang, S.-S. Lee, Y.-C. Shih, C.-W. Chen, H.-C. Kuo, F.-C. Chuang, and Y.-L. Chueh, “Phase-engineered ptse2-layered films by a plasma-assisted selenization process toward all ptse2-based field effect transistor to highly sensitive, flexible, and wide-spectrum photoresponse photodetectors,” *Small*, vol. 14, no. 19, p. 1800032, 2018.
- [71] X. Ling, Y. Lin, Q. Ma, Z. Wang, Y. Song, L. Yu, S. Huang, W. Fang, X. Zhang, A. L. Hsu, Y. Bie, Y.-H. Lee, Y. Zhu, L. Wu, J. Li, P. Jarillo-Herrero, M. Dresselhaus, T. Palacios, and

- J. Kong, “Parallel stitching of 2d materials,” *Advanced Materials*, vol. 28, no. 12, pp. 2322–2329, 2016.
- [72] S. Cho, S. Kim, J. H. Kim, J. Zhao, J. Seok, D. H. Keum, J. Baik, D.-H. Choe, K. J. Chang, K. Suenaga, S. W. Kim, Y. H. Lee, and H. Yang, “Phase patterning for ohmic homojunction contact in mote2,” *Science*, vol. 349, no. 6248, pp. 625–628, 2015.
- [73] D. S. Fox, Y. Zhou, P. Maguire, A. O’Neill, C. Ó’Coileáin, R. Gatensby, A. M. Glushenkov, T. Tao, G. S. Duesberg, I. V. Shvets, M. Abid, M. Abid, H.-C. Wu, Y. Chen, J. N. Coleman, J. F. Donegan, and H. Zhang, “Nanopatterning and electrical tuning of mos2 layers with a subnanometer helium ion beam,” *Nano Letters*, vol. 15, no. 8, pp. 5307–5313, 2015.
- [74] H. Qiu, T. Xu, Z. Wang, W. Ren, H. Nan, Z. Ni, Q. Chen, S. Yuan, F. Miao, F. Song, G. Long, Y. Shi, L. Sun, J. Wang, and X. Wang, “Hopping transport through defect-induced localized states in molybdenum disulphide,” *Nature Communications*, vol. 4, no. 1, p. 2642, 2013.
- [75] M. G. Stanford, P. R. Pudasaini, E. T. Gallmeier, N. Cross, L. Liang, A. Oyedele, G. Duscher, M. Mahjouri-Samani, K. Wang, K. Xiao, D. B. Geohegan, A. Belianinov, B. G. Sumpter, and P. D. Rack, “High conduction hopping behavior induced in transition metal dichalcogenides by percolating defect networks: Toward atomically thin circuits,” *Advanced Functional Materials*, vol. 27, no. 36, p. 1702829, 2017.
- [76] J. H. Kim, T.-J. Ko, E. Okogbue, S. S. Han, M. S. Shawkat, M. G. Kaium, K. H. Oh, H.-S. Chung, and Y. Jung, “Centimeter-scale green integration of layer-by-layer 2d tmd vdw heterostructures on arbitrary substrates by water-assisted layer transfer,” *Scientific Reports*, vol. 9, no. 1, p. 1641, 2019.
- [77] M. S. Shawkat, J. Gil, S. S. Han, T.-J. Ko, M. Wang, D. Dev, J. Kwon, G.-H. Lee, K. H. Oh, H.-S. Chung, T. Roy, Y. Jung, and Y. Jung, “Thickness-independent semiconducting-to-

- metallic conversion in wafer-scale two-dimensional ptse2 layers by plasma-driven chalcogen defect engineering,” *ACS Applied Materials Interfaces*, vol. 12, no. 12, pp. 14341–14351, 2020.
- [78] J. Shi, Y. Huan, M. Hong, R. Xu, P. Yang, Z. Zhang, X. Zou, and Y. Zhang, “Chemical vapor deposition grown large-scale atomically thin platinum diselenide with semimetal–semiconductor transition,” *ACS Nano*, vol. 13, no. 7, pp. 8442–8451, 2019.
- [79] D. Hu, T. Zhao, X. Ping, H. Zheng, L. Xing, X. Liu, J. Zheng, L. Sun, L. Gu, C. Tao, D. Wang, and L. Jiao, “Unveiling the layer-dependent catalytic activity of ptse2 atomic crystals for the hydrogen evolution reaction,” *Angewandte Chemie International Edition*, vol. 58, no. 21, pp. 6977–6981, 2019.
- [80] C. Yim, V. Passi, M. C. Lemme, G. S. Duesberg, C. Ó Coileáin, E. Pallecchi, D. Fadil, and N. McEvoy, “Electrical devices from top-down structured platinum diselenide films,” *npj 2D Materials and Applications*, vol. 2, no. 1, p. 5, 2018.
- [81] L. Wang, S. Zhang, N. McEvoy, Y.-y. Sun, J. Huang, Y. Xie, N. Dong, X. Zhang, I. M. Kislyakov, J.-M. Nunzi, L. Zhang, and J. Wang, “Nonlinear optical signatures of the transition from semiconductor to semimetal in ptse2,” *Laser Photonics Reviews*, vol. 13, no. 8, p. 1900052, 2019.
- [82] L. Ansari, S. Monaghan, N. McEvoy, C. Coileáin, C. P. Cullen, J. Lin, R. Siris, T. Stimpel-Lindner, K. F. Burke, G. Mirabelli, R. Duffy, E. Caruso, R. E. Nagle, G. S. Duesberg, P. K. Hurley, and F. Gity, “Quantum confinement-induced semimetal-to-semiconductor evolution in large-area ultra-thin ptse2 films grown at 400°C,” *npj 2D Materials and Applications*, vol. 3, no. 1, p. 33, 2019.

- [83] C. S. Boland, C. Coileáin, S. Wagner, J. B. McManus, C. P. Cullen, M. C. Lemme, G. S. Duesberg, and N. McEvoy, "Ptse 2 grown directly on polymer foil for use as a robust piezoresistive sensor," *2D Materials*, vol. 6, no. 4, p. 045029, 2019.
- [84] B. Huang, F. Tian, Y. Shen, M. Zheng, Y. Zhao, J. Wu, Y. Liu, S. J. Pennycook, and J. T. L. Thong, "Selective engineering of chalcogen defects in mos2 by low-energy helium plasma," *ACS Applied Materials Interfaces*, vol. 11, no. 27, pp. 24404–24411, 2019.
- [85] A. P. Nayak, S. Bhattacharyya, J. Zhu, J. Liu, X. Wu, T. Pandey, C. Jin, A. K. Singh, D. Ak-inwande, and J.-F. Lin, "Pressure-induced semiconducting to metallic transition in multilayered molybdenum disulphide," *Nature Communications*, vol. 5, no. 1, p. 3731, 2014.
- [86] K. Dückers, H. P. Bonzel, and D. A. Wesner, "Surface core level shifts of pt(111) measured with y m radiation (132.3 ev)," *Surface Science*, vol. 166, no. 1, pp. 141–158, 1986.
- [87] M. Wang, J. H. Kim, S. S. Han, M. Je, J. Gil, C. Noh, T.-J. Ko, K. S. Lee, D. I. Son, T.-S. Bae, H. I. Ryu, K. H. Oh, Y. Jung, H. Choi, H.-S. Chung, and Y. Jung, "Structural evolutions of vertically aligned two-dimensional mos2 layers revealed by in situ heating transmission electron microscopy," *The Journal of Physical Chemistry C*, vol. 123, no. 45, pp. 27843–27853, 2019.
- [88] C. Kittel, *Introduction to Solid State Physics*. Hoboken, NJ: John Wiley Sons, Inc, 8th ed., 2005.
- [89] D. Sinha and J. U. Lee, "Ideal graphene/silicon schottky junction diodes," *Nano letters*, vol. 14, no. 8, pp. 4660–4664, 2014.
- [90] Z. Xiao and T. Wei, "Calculation of the intrinsic carrier concentration and the minority-carrier concentration of silicon for heavy phosphorus doping with non-parabolic energy bands at low temperature," *Solid State Electronics*, vol. 10, no. 38, pp. 1837–1838, 1995.

- [91] F. J. Morin and J. P. Maita, “Electrical properties of silicon containing arsenic and boron,” *Physical Review*, vol. 96, no. 1, pp. 28–35, 1954.
- [92] E. H. Rhoderick and R. H. Williams, *Metal-semiconductor contacts*. Clarendon Press, 1988.
- [93] S. Cheung and N. Cheung, “Extraction of schottky diode parameters from forward current-voltage characteristics,” *Applied physics letters*, vol. 49, no. 2, pp. 85–87, 1986.
- [94] C.-C. Chen, M. Aykol, C.-C. Chang, A. Levi, and S. B. Cronin, “Graphene-silicon schottky diodes,” *Nano letters*, vol. 11, no. 5, pp. 1863–1867, 2011.
- [95] L. Zeng, S. Lin, Z. Lou, H. Yuan, H. Long, Y. Li, W. Lu, S. P. Lau, D. Wu, and Y. H. Tsang, “Ultrafast and sensitive photodetector based on a ptse2/silicon nanowire array heterojunction with a multiband spectral response from 200 to 1550nm,” *NPG Asia Materials*, vol. 10, no. 4, pp. 352–362, 2018.
- [96] S. M. Sze, Y. Li, and K. K. Ng, *Physics of semiconductor devices*. John wiley sons, 2021.
- [97] K. Huang, X. Yu, J. Cong, and D. Yang, “Progress of graphene–silicon heterojunction photovoltaic devices,” *Advanced Materials Interfaces*, vol. 5, no. 24, p. 1801520, 2018.
- [98] T. Cui, R. Lv, Z.-H. Huang, S. Chen, Z. Zhang, X. Gan, Y. Jia, X. Li, K. Wang, D. Wu, *et al.*, “Enhanced efficiency of graphene/silicon heterojunction solar cells by molecular doping,” *Journal of Materials Chemistry A*, vol. 1, no. 18, pp. 5736–5740, 2013.
- [99] X. Li, D. Xie, H. Park, M. Zhu, T. H. Zeng, K. Wang, J. Wei, D. Wu, J. Kong, and H. Zhu, “Ion doping of graphene for high-efficiency heterojunction solar cells,” *Nanoscale*, vol. 5, no. 5, pp. 1945–1948, 2013.
- [100] E. Shi, H. Li, L. Yang, L. Zhang, Z. Li, P. Li, Y. Shang, S. Wu, X. Li, J. Wei, *et al.*, “Colloidal antireflection coating improves graphene–silicon solar cells,” *Nano letters*, vol. 13, no. 4, pp. 1776–1781, 2013.

- [101] Y. Song, X. Li, C. Mackin, X. Zhang, W. Fang, T. Palacios, H. Zhu, and J. Kong, “Role of interfacial oxide in high-efficiency graphene–silicon schottky barrier solar cells,” *Nano letters*, vol. 15, no. 3, pp. 2104–2110, 2015.
- [102] J. M. Kim, S. Kim, D. H. Shin, S. W. Seo, H. S. Lee, J. H. Kim, C. W. Jang, S. S. Kang, S.-H. Choi, G. Y. Kwak, *et al.*, “Si-quantum-dot heterojunction solar cells with 16.2% efficiency achieved by employing doped-graphene transparent conductive electrodes,” *Nano Energy*, vol. 43, pp. 124–129, 2018.
- [103] L. Britnell, R. M. Ribeiro, A. Eckmann, R. Jalil, B. D. Belle, A. Mishchenko, Y. J. Kim, R. V. Gorbachev, T. Georgiou, S. V. Morozov, A. N. Grigorenko, A. K. Geim, C. Casiraghi, A. H. C. Neto, and K. S. Novoselov, “Strong light-matter interactions in heterostructures of atomically thin films,” *Science*, vol. 340, no. 6138, p. 1311, 2013.
- [104] T.-J. Ko, S. S. Han, E. Okogbue, M. S. Shawkat, M. Wang, J. Ma, T.-S. Bae, S. B. Hafiz, D.-K. Ko, H.-S. Chung, K. H. Oh, and Y. Jung, “Wafer-scale 2d ptte2 layers-enabled kirigami heaters with superior mechanical stretchability and electro-thermal responsiveness,” *Applied Materials Today*, vol. 20, p. 100718, 2020.
- [105] J. Qiao, X. Kong, Z.-X. Hu, F. Yang, and W. Ji, “High-mobility transport anisotropy and linear dichroism in few-layer black phosphorus,” *Nature Communications*, vol. 5, no. 1, p. 4475, 2014.
- [106] Y. Wang, L. Li, W. Yao, S. Song, J. T. Sun, J. Pan, X. Ren, C. Li, E. Okunishi, Y.-Q. Wang, E. Wang, Y. Shao, Y. Y. Zhang, H.-t. Yang, E. F. Schwier, H. Iwasawa, K. Shimada, M. Taniguchi, Z. Cheng, S. Zhou, S. Du, S. J. Pennycook, S. T. Pantelides, and H.-J. Gao, “Monolayer ptse2, a new semiconducting transition-metal-dichalcogenide, epitaxially grown by direct selenization of pt,” *Nano Letters*, vol. 15, no. 6, pp. 4013–4018, 2015.

- [107] M. S. Bahramy, O. J. Clark, B. J. Yang, J. Feng, L. Bawden, J. M. Riley, I. Marković, F. Mazzola, V. Sunko, D. Biswas, S. P. Cooil, M. Jorge, J. W. Wells, M. Leandersson, T. Balasubramanian, J. Fujii, I. Vobornik, J. E. Rault, T. K. Kim, M. Hoesch, K. Okawa, M. Asakawa, T. Sasagawa, T. Eknapakul, W. Meevasana, and P. D. C. King, “Ubiquitous formation of bulk dirac cones and topological surface states from a single orbital manifold in transition-metal dichalcogenides,” *Nature Materials*, vol. 17, no. 1, pp. 21–28, 2018.
- [108] M. Yan, H. Huang, K. Zhang, E. Wang, W. Yao, K. Deng, G. Wan, H. Zhang, M. Arita, H. Yang, Z. Sun, H. Yao, Y. Wu, S. Fan, W. Duan, and S. Zhou, “Lorentz-violating type-ii dirac fermions in transition metal dichalcogenide ptte<sub>2</sub>,” *Nature Communications*, vol. 8, no. 1, p. 257, 2017.
- [109] L. Wang, J. Jie, Z. Shao, Q. Zhang, X. Zhang, Y. Wang, Z. Sun, and S.-T. Lee, “Mos<sub>2</sub>/si heterojunction with vertically standing layered structure for ultrafast, high-detectivity, self-driven visible–near infrared photodetectors,” *Advanced Functional Materials*, vol. 25, no. 19, pp. 2910–2919, 2015.
- [110] H. Huang, J. Wang, W. Hu, L. Liao, P. Wang, X. Wang, F. Gong, Y. Chen, G. Wu, W. Luo, *et al.*, “Highly sensitive visible to infrared mote<sub>2</sub> photodetectors enhanced by the photogating effect,” *Nanotechnology*, vol. 27, no. 44, p. 445201, 2016.
- [111] C. H. Mak, S. Lin, L. Rogée, and S. P. Lau, “Photoresponse of wafer-scale palladium diselenide films prepared by selenization method,” *Journal of Physics D: Applied Physics*, vol. 53, no. 6, p. 065102, 2019.
- [112] H. Tian, A. Hu, Q. Liu, X. He, and X. Guo, “Interface-induced high responsivity in hybrid graphene/gaas photodetector,” *Advanced Optical Materials*, vol. 8, no. 8, p. 1901741, 2020.
- [113] X. Wan, Y. Xu, H. Guo, K. Shehzad, A. Ali, Y. Liu, J. Yang, D. Dai, C.-T. Lin, L. Liu, H.-C. Cheng, F. Wang, X. Wang, H. Lu, W. Hu, X. Pi, Y. Dan, J. Luo, T. Hasan, X. Duan, X. Li,

- J. Xu, D. Yang, T. Ren, and B. Yu, “A self-powered high-performance graphene/silicon ultraviolet photodetector with ultra-shallow junction: breaking the limit of silicon?,” *npj 2D Materials and Applications*, vol. 1, no. 1, p. 4, 2017.
- [114] L.-H. Zeng, Q.-M. Chen, Z.-X. Zhang, D. Wu, H. Yuan, Y.-Y. Li, W. Qarony, S. P. Lau, L.-B. Luo, and Y. H. Tsang, “Multilayered  $\text{PdSe}_2$ /perovskite schottky junction for fast, self-powered, polarization-sensitive, broadband photodetectors, and image sensor application,” *Advanced Science*, vol. 6, no. 19, p. 1901134, 2019.
- [115] C. Xie, L. Zeng, Z. Zhang, Y.-H. Tsang, L. Luo, and J.-H. Lee, “High-performance broadband heterojunction photodetectors based on multilayered  $\text{PtSe}_2$  directly grown on a Si substrate,” *Nanoscale*, vol. 10, no. 32, pp. 15285–15293, 2018.
- [116] Z.-X. Zhang, Z. Long-Hui, X.-W. Tong, Y. Gao, C. Xie, Y. H. Tsang, L.-B. Luo, and Y.-C. Wu, “Ultrafast, self-driven, and air-stable photodetectors based on multilayer  $\text{PtSe}_2$ /perovskite heterojunctions,” *The Journal of Physical Chemistry Letters*, vol. 9, no. 6, pp. 1185–1194, 2018.
- [117] Z. Lu, Y. Xu, Y. Yu, K. Xu, J. Mao, G. Xu, Y. Ma, D. Wu, and J. Jie, “Ultrahigh speed and broadband few-layer  $\text{MoTe}_2$ /Si  $2\text{d}-3\text{d}$  heterojunction-based photodiodes fabricated by pulsed laser deposition,” *Advanced Functional Materials*, vol. 30, no. 9, p. 1907951, 2020.
- [118] L.-H. Zeng, D. Wu, S.-H. Lin, C. Xie, H.-Y. Yuan, W. Lu, S. P. Lau, Y. Chai, L.-B. Luo, Z.-J. Li, and Y. H. Tsang, “Controlled synthesis of  $2\text{d}$  palladium diselenide for sensitive photodetector applications,” *Advanced Functional Materials*, vol. 29, no. 1, p. 1806878, 2019.
- [119] J.-M. Liu, *Photonic devices*. Cambridge University Press, 2009.

- [120] L. Wang, J.-J. Li, Q. Fan, Z.-F. Huang, Y.-C. Lu, C. Xie, C.-Y. Wu, and L.-B. Luo, “A high-performance near-infrared light photovoltaic detector based on a multilayered ptse2/ge heterojunction,” *Journal of Materials Chemistry C*, vol. 7, no. 17, pp. 5019–5027, 2019.
- [121] K. Zhou, J. Shen, X. Li, X. Hong, W. Feng, X. Tang, X. Jiang, D. Wei, Y. Chen, X. Liu, Y. Xie, D. Wei, and T. Sun, “Broadband photodetector based on 2d layered ptse2 / silicon heterojunction at room-temperature,” *Physica E: Low-dimensional Systems and Nanostructures*, vol. 123, p. 114147, 2020.
- [122] C. Yim, N. McEvoy, S. Riazimehr, D. S. Schneider, F. Gity, S. Monaghan, P. K. Hurley, M. C. Lemme, and G. S. Duesberg, “Wide spectral photoresponse of layered platinum diselenide-based photodiodes,” *Nano letters*, vol. 18, no. 3, pp. 1794–1800, 2018.
- [123] D. Wu, C. Jia, F. Shi, L. Zeng, P. Lin, L. Dong, Z. Shi, Y. Tian, X. Li, and J. Jie, “Mixed-dimensional pdse 2/sinwa heterostructure based photovoltaic detectors for self-driven, broadband photodetection, infrared imaging and humidity sensing,” *Journal of Materials Chemistry A*, vol. 8, no. 7, pp. 3632–3642, 2020.
- [124] D. Wu, Y. Wang, L. Zeng, C. Jia, E. Wu, T. Xu, Z. Shi, Y. Tian, X. Li, and Y. H. Tsang, “Design of 2d layered ptse2 heterojunction for the high-performance, room-temperature, broadband, infrared photodetector,” *ACS Photonics*, vol. 5, no. 9, pp. 3820–3827, 2018.
- [125] H. Qiao, Z. Huang, X. Ren, S. Liu, Y. Zhang, X. Qi, and H. Zhang, “Self-powered photodetectors based on 2d materials,” *Advanced Optical Materials*, vol. 8, no. 1, p. 1900765, 2020.
- [126] Q. Liang, Q. Wang, Q. Zhang, J. Wei, S. X. Lim, R. Zhu, J. Hu, W. Wei, C. Lee, C. Sow, *et al.*, “High-performance, room temperature, ultra-broadband photodetectors based on air-stable pdse2,” *Advanced Materials*, vol. 31, no. 24, p. 1807609, 2019.

- [127] W. Yu, S. Li, Y. Zhang, W. Ma, T. Sun, J. Yuan, K. Fu, and Q. Bao, “Near-infrared photodetectors based on  $\text{MoS}_2$ /graphene heterostructure with high responsivity and flexibility,” *Small*, vol. 13, no. 24, p. 1700268, 2017.
- [128] R. K. Ulaganathan, Y.-Y. Lu, C.-J. Kuo, S. R. Tamalampudi, R. Sankar, K. M. Boopathi, A. Anand, K. Yadav, R. J. Mathew, C.-R. Liu, *et al.*, “High photosensitivity and broad spectral response of multi-layered germanium sulfide transistors,” *Nanoscale*, vol. 8, no. 4, pp. 2284–2292, 2016.
- [129] X. Zhou, L. Gan, W. Tian, Q. Zhang, S. Jin, H. Li, Y. Bando, D. Golberg, and T. Zhai, “Ultrathin  $\text{SnS}_2$  flakes grown by chemical vapor deposition for high-performance photodetectors,” *Advanced Materials*, vol. 27, no. 48, pp. 8035–8041, 2015.
- [130] G. W. Mudd, S. A. Svatek, L. Hague, O. Makarovskiy, Z. R. Kudrynskiy, C. J. Mellor, P. H. Beton, L. Eaves, K. S. Novoselov, Z. D. Kovalyuk, *et al.*, “High broad-band photoresponsivity of mechanically formed  $\text{InSe}$ -graphene van der Waals heterostructures,” *Advanced Materials*, vol. 27, no. 25, pp. 3760–3766, 2015.
- [131] X. Wang, P. Wang, J. Wang, W. Hu, X. Zhou, N. Guo, H. Huang, S. Sun, H. Shen, T. Lin, *et al.*, “Ultrasensitive and broadband  $\text{MoS}_2$  photodetector driven by ferroelectrics,” *Advanced materials*, vol. 27, no. 42, pp. 6575–6581, 2015.
- [132] G. Su, V. G. Hadjiev, P. E. Loya, J. Zhang, S. Lei, S. Maharjan, P. Dong, P. M. Ajayan, J. Lou, and H. Peng, “Chemical vapor deposition of thin crystals of layered semiconductor  $\text{SnS}_2$  for fast photodetection application,” *Nano letters*, vol. 15, no. 1, pp. 506–513, 2015.
- [133] J. Mao, Y. Yu, L. Wang, X. Zhang, Y. Wang, Z. Shao, and J. Jie, “Ultrafast, broadband photodetector based on  $\text{MoS}_2$ /silicon heterojunction with vertically standing layered structure using graphene as transparent electrode,” *Advanced Science*, vol. 3, no. 11, p. 1600018, 2016.

- [134] R. Zhuo, L. Zeng, H. Yuan, D. Wu, Y. Wang, Z. Shi, T. Xu, Y. Tian, X. Li, and Y. H. Tsang, “In-situ fabrication of ptse 2/gan heterojunction for self-powered deep ultraviolet photodetector with ultrahigh current on/off ratio and detectivity,” *Nano Research*, vol. 12, no. 1, pp. 183–189, 2019.
- [135] F. Wang, Z. Wang, K. Xu, F. Wang, Q. Wang, Y. Huang, L. Yin, and J. He, “Tunable gate-mos2 van der waals p–n junctions with novel optoelectronic performance,” *Nano letters*, vol. 15, no. 11, pp. 7558–7566, 2015.
- [136] S. R. Tamalampudi, Y.-Y. Lu, R. K. U, R. Sankar, C.-D. Liao, C.-H. Cheng, F. C. Chou, and Y.-T. Chen, “High performance and bendable few-layered inse photodetectors with broad spectral response,” *Nano letters*, vol. 14, no. 5, pp. 2800–2806, 2014.
- [137] A. P. S. Gaur, S. Sahoo, M. Ahmadi, S. P. Dash, M. J. F. Guinel, and R. S. Katiyar, “Surface energy engineering for tunable wettability through controlled synthesis of mos2,” *Nano Letters*, vol. 14, no. 8, pp. 4314–4321, 2014.
- [138] M. Alves, A. Pérez-Rodríguez, P. J. Dale, C. Domínguez, and S. Sadewasser, “Thin-film micro-concentrator solar cells,” *Journal of Physics: Energy*, vol. 2, no. 1, p. 012001, 2019.
- [139] X. Li, Y. Jung, K. Sakimoto, T.-H. Goh, M. A. Reed, and A. D. Taylor, “Improved efficiency of smooth and aligned single walled carbon nanotube/silicon hybrid solar cells,” *Energy Environmental Science*, vol. 6, no. 3, pp. 879–887, 2013.
- [140] Y. Fang, Y. Ge, C. Wang, and H. Zhang, “Mid-infrared photonics using 2d materials: Status and challenges,” *Laser Photonics Reviews*, vol. 14, no. 1, p. 1900098, 2020.
- [141] A. Rogalski, “Hgcdte infrared detector material: history, status and outlook,” *Reports on Progress in Physics*, vol. 68, no. 10, pp. 2267–2336, 2005.

- [142] J. Xu, J. Hu, R. Wang, Q. Li, W. Li, Y. Guo, F. Liu, Z. Ullah, L. Wen, and L. Liu, “Ultra-broadband graphene-insb heterojunction photodetector,” *Applied Physics Letters*, vol. 111, no. 5, p. 051106, 2017.
- [143] G. Sarusi, “Qwip or other alternative for third generation infrared systems,” *Infrared Physics Technology*, vol. 44, no. 5, pp. 439–444, 2003.
- [144] F. Wang, Y. Zhang, Y. Gao, P. Luo, J. Su, W. Han, K. Liu, H. Li, and T. Zhai, “2d metal chalcogenides for ir photodetection,” *Small*, vol. 15, no. 30, p. 1901347, 2019.
- [145] X. Guan, X. Yu, D. Periyangounder, M. R. Benzigar, J.-K. Huang, C.-H. Lin, J. Kim, S. Singh, L. Hu, G. Liu, D. Li, J.-H. He, F. Yan, Q. J. Wang, and T. Wu, “Recent progress in short- to long-wave infrared photodetection using 2d materials and heterostructures,” *Advanced Optical Materials*, vol. n/a, no. n/a, p. 2001708.
- [146] X. C. Yu and Q. J. Wang, “2d materials based mid-infrared and terahertz optoelectronics,” in *2019 Asia Communications and Photonics Conference (ACP)*, pp. 1–1.
- [147] Y. Zhou, M. Zhang, Z. Guo, L. Miao, S.-T. Han, Z. Wang, X. Zhang, H. Zhang, and Z. Peng, “Recent advances in black phosphorus-based photonics, electronics, sensors and energy devices,” *Materials Horizons*, vol. 4, no. 6, pp. 997–1019, 2017.
- [148] K. Kim, J.-Y. Choi, T. Kim, S.-H. Cho, and H.-J. Chung, “A role for graphene in silicon-based semiconductor devices,” *Nature*, vol. 479, no. 7373, pp. 338–344, 2011.
- [149] K. S. Novoselov, V. I. Falko, L. Colombo, P. R. Gellert, M. G. Schwab, and K. Kim, “A roadmap for graphene,” *Nature*, vol. 490, no. 7419, pp. 192–200, 2012.
- [150] F. Xia, H. Wang, D. Xiao, M. Dubey, and A. Ramasubramaniam, “Two-dimensional material nanophotonics,” *Nature Photonics*, vol. 8, no. 12, pp. 899–907, 2014.

- [151] K. Ahmed and T. Chiang, "Schottky barrier height extraction from forward current-voltage characteristics of non-ideal diodes with high series resistance," *Applied Physics Letters*, vol. 102, no. 4, p. 042110, 2013.
- [152] J. Lai, J. Ma, Y. Liu, K. Zhang, X. Zhuo, J. Chen, S. Zhou, and D. Sun, "Photocurrent response of type-ii dirac semimetal ptte2," *2D Materials*, vol. 7, no. 3, p. 034003, 2020.
- [153] J. M. Dawlaty, S. Shivaraman, J. Strait, P. George, M. Chandrashekhara, F. Rana, M. G. Spencer, D. Veksler, and Y. Chen, "Measurement of the optical absorption spectra of epitaxial graphene from terahertz to visible," *Applied Physics Letters*, vol. 93, no. 13, p. 131905, 2008.
- [154] B. Sensale-Rodriguez, R. Yan, M. Zhu, D. Jena, L. Liu, and H. G. Xing, "Efficient terahertz electro-absorption modulation employing graphene plasmonic structures," *Applied Physics Letters*, vol. 101, no. 26, p. 261115, 2012.
- [155] P. Martyniuk and A. Rogalski, "Hot infrared photodetectors," *Opto-Electronics Review*, vol. 21, no. 2, pp. 239–257, 2013.
- [156] C. Downs and T. E. Vandervelde, "Progress in infrared photodetectors since 2000," *Sensors*, vol. 13, no. 4, pp. 5054–5098, 2013.
- [157] E. Dereniak and G. Boreman, "Infrared detectors and systems wiley," *New York*, 1996.
- [158] J. Lai, X. Liu, J. Ma, Q. Wang, K. Zhang, X. Ren, Y. Liu, Q. Gu, X. Zhuo, W. Lu, Y. Wu, Y. Li, J. Feng, S. Zhou, J.-H. Chen, and D. Sun, "Anisotropic broadband photoresponse of layered type-ii weyl semimetal mote2," *Advanced Materials*, vol. 30, no. 22, p. 1707152, 2018.

- [159] X. Tang, M. M. Ackerman, M. Chen, and P. Guyot-Sionnest, “Dual-band infrared imaging using stacked colloidal quantum dot photodiodes,” *Nature Photonics*, vol. 13, no. 4, pp. 277–282, 2019.
- [160] Y. Liu, Y. Huang, and X. Duan, “Van der waals integration before and beyond two-dimensional materials,” *Nature*, vol. 567, no. 7748, pp. 323–333, 2019.
- [161] Y. Liu, P. Wang, Y. Wang, Z. Lin, H. Liu, J. Huang, Y. Huang, and X. Duan, “van der waals integrated devices based on nanomembranes of 3d materials,” *Nano Lett.*, vol. 20, no. 2, pp. 1410–1416, 2020.
- [162] Z. Lin, Y. Huang, and X. Duan, “Van der waals thin-film electronics,” *Nat. Electron.*, vol. 2, no. 9, pp. 378–388, 2019.
- [163] L. Kong, X. Zhang, Q. Tao, M. Zhang, W. Dang, Z. Li, L. Feng, L. Liao, X. Duan, and Y. Liu, “Doping-free complementary wse<sub>2</sub> circuit via van der waals metal integration,” *Nat. Commun.*, vol. 11, no. 1, p. 1866, 2020.
- [164] Q. A. Vu, Y. S. Shin, Y. R. Kim, V. L. Nguyen, W. T. Kang, H. Kim, D. H. Luong, I. M. Lee, K. Lee, D.-S. Ko, J. Heo, S. Park, Y. H. Lee, and W. J. Yu, “Two-terminal floating-gate memory with van der waals heterostructures for ultrahigh on/off ratio,” *Nat. Commun.*, vol. 7, no. 1, p. 12725, 2016.
- [165] Y. Deng, Z. Luo, N. J. Conrad, H. Liu, Y. Gong, S. Najmaei, P. M. Ajayan, J. Lou, X. Xu, and P. D. Ye, “Black phosphorus–monolayer mos<sub>2</sub> van der waals heterojunction p–n diode,” *ACS Nano*, vol. 8, no. 8, pp. 8292–8299, 2014.
- [166] Y. Choi, J. Kang, D. Jariwala, M. S. Kang, T. J. Marks, M. C. Hersam, and J. H. Cho, “Low-voltage complementary electronics from ion-gel-gated vertical van der waals heterostructures,” *Adv. Mater.*, vol. 28, no. 19, pp. 3742–3748, 2016.

- [167] W. Kim, C. Li, F. A. Chaves, D. Jiménez, R. D. Rodriguez, J. Susoma, M. A. Fenner, H. Lipsanen, and J. Riikonen, “Tunable graphene–gase dual heterojunction device,” *Adv. Mater.*, vol. 28, no. 9, pp. 1845–1852, 2016.
- [168] S. Masubuchi, M. Morimoto, S. Morikawa, M. Onodera, Y. Asakawa, K. Watanabe, T. Taniguchi, and T. Machida, “Autonomous robotic searching and assembly of two-dimensional crystals to build van der waals superlattices,” *Nat. Commun.*, vol. 9, no. 1, p. 1413, 2018.
- [169] S. G. Martanov, N. K. Zhurbina, M. V. Pugachev, A. I. Duleba, M. A. Akmaev, V. V. Belykh, and A. Y. Kuntsevich, “Making van der waals heterostructures assembly accessible to everyone,” *Nanomaterials*, vol. 10, no. 11, p. 2305, 2020.
- [170] S. S. Han, T.-J. Ko, C. Yoo, M. S. Shawkat, H. Li, B. K. Kim, W.-K. Hong, T.-S. Bae, H.-S. Chung, K. H. Oh, and Y. Jung, “Automated assembly of wafer-scale 2d tmd heterostructures of arbitrary layer orientation and stacking sequence using water dissoluble salt substrates,” *Nano Lett.*, vol. 20, no. 5, pp. 3925–3934, 2020.
- [171] W. J. Yu, Q. A. Vu, H. Oh, H. G. Nam, H. Zhou, S. Cha, J.-Y. Kim, A. Carvalho, M. Jeong, H. Choi, A. H. Castro Neto, Y. H. Lee, and X. Duan, “Unusually efficient photocurrent extraction in monolayer van der waals heterostructure by tunnelling through discretized barriers,” *Nat. Commun.*, vol. 7, no. 1, p. 13278, 2016.
- [172] Y. Chen, Y. Li, Y. Zhao, H. Zhou, and H. Zhu, “Highly efficient hot electron harvesting from graphene before electron-hole thermalization,” *Sci. Adv.*, vol. 5, no. 11, p. eaax9958, 2019.
- [173] R. Frisenda, E. Navarro-Moratalla, P. Gant, D. P. De Lara, P. Jarillo-Herrero, R. V. Gorbachev, and A. Castellanos-Gomez, “Recent progress in the assembly of nanodevices and van der waals heterostructures by deterministic placement of 2d materials,” *Chemical Society Reviews*, vol. 47, no. 1, pp. 53–68, 2018.

- [174] Y.-C. Lin, W. Zhang, J.-K. Huang, K.-K. Liu, Y.-H. Lee, C.-T. Liang, C.-W. Chu, and L.-J. Li, “Wafer-scale mos 2 thin layers prepared by moo 3 sulfurization,” *Nanoscale*, vol. 4, no. 20, pp. 6637–6641, 2012.
- [175] A. Gurarslan, Y. Yu, L. Su, Y. Yu, F. Suarez, S. Yao, Y. Zhu, M. Ozturk, Y. Zhang, and L. Cao, “Surface-energy-assisted perfect transfer of centimeter-scale monolayer and few-layer mos2 films onto arbitrary substrates,” *ACS nano*, vol. 8, no. 11, pp. 11522–11528, 2014.
- [176] K.-K. Liu, W. Zhang, Y.-H. Lee, Y.-C. Lin, M.-T. Chang, C.-Y. Su, C.-S. Chang, H. Li, Y. Shi, H. Zhang, *et al.*, “Growth of large-area and highly crystalline mos2 thin layers on insulating substrates,” *Nano letters*, vol. 12, no. 3, pp. 1538–1544, 2012.
- [177] M. S. Shawkat, S. S. Han, H.-S. Chung, S. A. Mofid, C. Yoo, and Y. Jung, “Wafer-scale van der waals assembly of free-standing near atom thickness hetero-membranes for flexible photo-detectors,” *Advanced Electronic Materials*, vol. n/a, no. n/a, p. 2100395.
- [178] S. Kang and T.-S. Kim, “Capillary-force-driven switchable delamination of nanofilms and its application to green selective transfer,” *Adv. Mater. Technol.*, vol. 6, no. 3, p. 2001082, 2021.
- [179] P. K. Chow, E. Singh, B. C. Viana, J. Gao, J. Luo, J. Li, Z. Lin, A. L. Elías, Y. Shi, Z. Wang, M. Terrones, and N. Koratkar, “Wetting of mono and few-layered ws2 and mos2 films supported on si/sio2 substrates,” *ACS Nano*, vol. 9, no. 3, pp. 3023–3031, 2015.
- [180] A. Kozbial, X. Gong, H. Liu, and L. Li, “Understanding the intrinsic water wettability of molybdenum disulfide (mos2),” *Langmuir*, vol. 31, no. 30, pp. 8429–8435, 2015.
- [181] G. Konstantatos, “Current status and technological prospect of photodetectors based on two-dimensional materials,” *Nat. Commun.*, vol. 9, no. 1, p. 5266, 2018.

- [182] S. J. Kim, K. Choi, B. Lee, Y. Kim, and B. H. Hong, “Materials for flexible, stretchable electronics: Graphene and 2d materials,” *Annu. Rev. Mater. Res.*, vol. 45, no. 1, pp. 63–84, 2015.
- [183] A. K. Geim and I. V. Grigorieva, “Van der waals heterostructures,” *Nature*, vol. 499, no. 7459, pp. 419–425, 2013.